A THz Lens Antenna fed by a Photoconductive Connected Dipole Array

Antonios Pelekanidis (4803116)

TU Delft

A THz Lens Antenna fed by a Photoconductive Connected Dipole Array

by

Antonios Pelekanidis

to obtain the degree of Master of Science
at the Delft University of Technology,
to be defended publicly on 31 August 2020 at 10.00

Student number:	4803116	
Project duration:	November 26, 2019 - August 31, 2020	
Thesis committee:	Prof. dr. A. Neto,	TU Delft, supervisor
	Prof. dr. N. Llombart,	TU Delft
	dr. M. Mastrangeli,	TU Delft
	dr. P. M. Sberna,	TU Delft

An electronic version of this thesis is available at `http://repository.tudelft.nl/`.

TU Delft

Preface

This thesis is the second part of the work on photoconductive antennas that I have conducted in the THz Sensing group. The first part has been focused on the design of a photoconductive connected array (PCCA) of dipoles, targeting at a radiation to frequencies up to 5 THz. The outcome of this first part was the determination of all geometrical parameters for the connected array, such as periodicity, width of the dipoles, tapering, as well as for a microlens array that is part of the excitation mechanism of the connected array.

In the thesis we explore some practical aspects related to the fabrication of this type of antenna. Due to the small dimensions of the structure that are required in order to have efficient radiation up to THz frequencies, and the complexity of the geometries, there are many challenges that need to be taken into consideration and are investigated in the thesis. Apart from this, the thesis includes a theoretical study regarding the radiation of the lens antenna. This study constitutes an extensive part of the thesis, because it also includes the development of a Matlab GUI tool that calculates the far field radiated by a lens antenna for any feed.

At this point I would like to thank my supervisor professor Andrea Neto for giving me the opportunity to study this fascinating topic and gain hands-on experience on the fabrication and measurement of $\mu m-$ sized structures. Also I would like to thank professor Nuria Llombart for her instructive feedback in every part of the thesis. This work could not have been completed without the assistance and support of dr. Paolo Sberna in the cleanroom and without the contribution of Daniel Fan at the 3D printing of the microlenses. Lastly, I would like to thank dr. Juan Bueno, dr. Shahab Dabironezare and Arturo Fiorellini Bernardis for their active participation and contribution on the various parts of the project.

Undoubtedly, there are also many people in the non-academic environment that supported me during this year of my thesis work. First of all, I would like to thank my parents and my girlfriend Despoina for all their support and encouragement even in tough times. Furthermore, I would like to thank my friends Manos, Pantelis, Roxani and Tworit for the beautiful and cheerful moments we shared during our stay in Delft. Finally, I would to thank Vangelis and Stefania because they gave me the opportunity to work in a totally unfamiliar field in order to financially support my studies.

Delft, August 2020

"Experience serves not only to confirm theory, but differs from it without disturbing it, it leads to new truths which theory only has not been able to reach."
(Jean le Rond d'Alembert)

Contents

List of Figures

List of Tables

1 Introduction

An electromagnetic wave is the key mechanism for the transmission of power and information from a transmitter to a receiver. The most common types of electromagnetic waves used for the transmission of information, basically for telecommunications, oscillate in frequencies that range between a few hundred kHz and a few hundred THz. Within this spectrum of the used frequencies there is a frequency region between 0.3 and 3 THz that is relatively unexplored and provides limited applications so far, as it is mainly used for space observation [1]. Exploitation of this spectrum would revolutionize some aspects of telecommunications and would enable the development of applications that are not feasible in other frequencies and wavelengths.

Two of the limitations that prevented these THz waves from flourishing have been the difficulty in their generation in transmission and in their detection in reception [2]. Over the last decades, however, there have been many attempts to overcome these limitations. A number of different THz sources are described in [3]. Among them, photoconductive antennas (PCAs) distinguish as a type of optoelectronic source that is able to generate THz broadband and narrowband waves and can be used either as a transmitter or a receiver. There has been extensive research, which aims to identify and overcome the weaknesses of PCAs. This thesis can be regarded as a part of this research, since it is dedicated in the design and experimental verification of a PCA.

1.1. Background

1.1.1. Generation and detection of THz waves with PCAs

The principle of operation of the PCA lies in the property of semiconductors to generate electron-hole pairs, when they are illuminated by a light source [4], provided that the light has an energy hf that is higher than the energy bandgap of the semiconductor. Free carriers can be developed at a semiconducting substrate, due to the fact that the electrons in the valence band move to the conduction band.This means practically that the conductivity of the semiconductor increases, and, under these conditions, an applied external electric field can move these free carriers and cause a drift current.

The semiconductor that is frequently chosen is low-temperature grown GaAs (LT-GaAs), because of its low carrier lifetime and its high dark resistivity [5]. The advantages of a low carrier lifetime and a high dark resistivity will become clear later. The required light comes from a laser source, which can emit either a short pulse or a continuous sinusoidal signal. In the first case, the photoconductor operates at a pulsed wave mode, whereas in the second case we refer to a continuous wave mode.

In the pulsed mode, the duration of the laser pulse is usually in the order of fs, if we want to radiate a THz signal. For an antenna in transmission, the semiconducting substrate is biased with a voltage that excites the aforementioned external electric field. Upon illumination, electron-hole pairs are instantly created and they start moving under the influence of the electric field leading to the excitation of a current. When the laser is off, the free carriers recombine, until none of them is left. The recombination rate is inversely proportional to the carrier lifetime, so the low carrier lifetime of LT-GaAs means that the recombination rate is high. As the number of free carriers decreases, the amplitude of the current also decreases. Finally, in the absence of free carriers, the conductivity of the material is zero and the resistivity is infinite, so the current becomes zero. In practice, however, there is still a small current running, even without the laser illumination. This current is called dark current and depends on a property of the material called dark resistivity. When the dark resistivity is high, like in LT-GaAs, the dark current is small. Obviously, the dark current is an undesired feature, because

we would like to fully control the current on the semiconductor by changing the laser pulse duration and intensity. The resulting current has, for a practically infinite dark resistivity, a duration of a few ps. Such a current can excite an antenna to radiate a broadband signal that reaches THz frequencies. The principle is similar for the photoconductor in reception, except that there is no bias voltage. Instead, the necessary electric field that initiates the drift current of the free carriers comes from the incident THz electromagnetic pulse.

In the continuous wave mode, the optical illumination intensity can be described with a sinusoidal function with angular frequency ω [3], so the conductivity and the excited current are expected to have a sinusoidal behaviour, as well. This operation mode is suitable for the radiation of narrowband waves. Our focus, however, is the pulsed laser and our goal is to transmit the generated broadband THz signal.

PCAs attracted much attention during the 1980s, when the transmitted and received fields could be experimentally verified thanks to the development of subpicosecond lasers. Indicatively, in 1984, Auston, Cheung and Smith [6] experimentally verified that the use of a photoconducting film that is illuminated by a fs-pulse laser is able to excite a current and subsequently an electric field, when the photoconductor is biased with a dc voltage. Specifically, the current they measured had duration of approximately 1 ps. Also, when used in reception, the photoconducting film illuminated by the same laser source could receive the radiated electric field. The rapid excitation of the photocurrent was attributed to the rapid excitation of free carriers in the photoconductive material by the optical pulse, whereas the fast decay of the current was attributed to the capture of the carriers at traps in the energy band due to the large number of defects.

In [7], the operation of large-aperture PCAs both as transmitters and receivers was investigated. This work contains some useful remarks that apply generally in the operation of PCAs. First of all, the conductivity of the semiconductor upon pulsed illumination depends on the transient mobility of the material and not on the steady-state mobility. The reason for that is that the carriers relax to thermal equilibrium, which is considered as the steady state, after a few picoseconds. The transient mobility is usually more than an order of magnitude lower than the value of the mobility in the steady state for a given semiconductor. Furthermore, the transient mobility of the electrons is higher than that of the holes, so the former are assumed to dominate and contribute mostly to the change in the conductivity. The authors' focus was on the saturation of the radiated field with respect to the optical intensity and fluence of the laser. They concluded, based on theoretical models and experimental results, that the near and far electric field saturates when the optical fluence increases above a certain level.

Jepsen, Jacobsen and Keiding [8] modelled and studied the whole THz generation - detection process, including the optical path of the THz signal. Specifically, they calculated the radiated electric field at the emitter, taking into account the screening effect that is caused when there is high optical fluence and consequently high carrier density. Under intense illumination, the space-charge field created by the separation of the electron-hole pairs becomes comparable to the applied external bias voltage, distorting the exponential relationship between the applied voltage and the excited current. The radiated field is modelled with a Gaussian spatial distribution and the authors study its propagation in an optical system that includes truncated, spherical lenses. For the detector, the authors make a distinction between large and small detectors, concluding that small detectors yield a signal differentiation whereas large detectors integrate the original signal. The bandwidth of the received signal is influenced by the size of the detector and the dielectric losses in the GaAs substrate; generally, the bandwidth is larger when small detectors are used.

The properties of various antennas and substrates as photoconductive emitters were investigated in [9]. The authors compared the performance of dipoles with different lengths, a bow-tie antenna and a strip line. As substrates, they used LT-GaAs and semi-insulating (SI) GaAs. They observed, among others, that longer dipoles radiate stronger signals due to their larger effective length, which is proportional to the electric field. However, the highest transmitted power was achieved with the (broadband) bow-tie antenna, since it could radiate much better at low frequencies and as efficiently as the other antennas at high frequencies. Regarding the substrates, although they observed higher transmitted powers from antennas on SI-GaAs due to the high mobility of the carriers in SI-GaAs, LT-GaAs has a better performance in terms of dark resistivity, breakdown voltage and screening. This comparison justifies the selection of LT-GaAs in the majority of the research works on PCAs.

A different study was conducted in [10], which was on continuous wave photomixers. Although this work seems to be beyond the focus of the thesis, as it studies continuous wave mode PCAs, there is much important background theoretical information and there are some considerations that are valid for the pulsed PCAs as well. Firstly, it describes the growth process of LT-GaAs, because LT-GaAs is the most preferred substrate material for photomixers as well. It is grown by molecular-beam epitaxy at approximately 200°C. The proportion

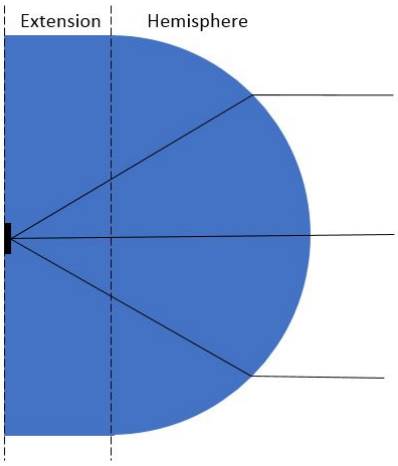

Figure 1.1: PCA in a hyperhemispherical lens and ray tracing according to [10]

of arsenic (As) in the material is 1% more than the proportion of gallium (Ga), which accounts for the short carrier lifetime. Annealing at 500°C is an important step in the process, because it creates As precipitates from the excess As atoms. The As precipitates lead to an improvement in the mobility, the resistivity and the breakdown electric field, without altering the short carrier lifetime. Secondly, the coupling of the antenna to the propagation medium, which most commonly is air, is discussed. For that, a hyperhemispherical silicon lens is proposed, which, according to [10], is a lens with a hemisperical shape and an extension made of the same material as the hemisphere. In this structure, the antenna is placed at the edge of the extension part, as is shown in Fig. 1.1. Furthermore, as fas as the measurement of the radiated power from a THz source is concerned, the author has identified bolometers as the most accurate detectors, that can detect a THz power as low as $10\,pW$. Finally, it is mentioned that the carrier lifetime is influenced by the applied bias electric field, which is a phenomenon that is not considered in most theoretical models. Specifically, at fields larger than $10^5\,V/cm$, the lifetime increases, because of ionization of traps and thus release of carriers back into the conduction or valence band. However, in our experimental setup, we will not target at such high bias electric fields, so this effect is not expected to emerge.

In [11], applications of PCAs and THz sources in general are described. The most important application, which is also mentioned by other authors as well, such as [17], is the THz time domain spectroscopy (THz-TDS). This is the characterization of the electric properties of a sample, based on its response upon an incident THz wave. Specifically, there is a delay of the signal when it propagates through the sample, compared to the reference (absence of a sample), and a change in the amplitude and phase of the received signal, due to the complex transmission coefficient T that characterizes the interface between the sample and air. A Fourier transform of the received signal gives information for the electrical properties of the sample with respect to the frequency. Fig. 1.2 presents the configuration of THz-TDS, the modules of which will be described later. Another application that is discussed in [11] is THz imaging. Experimental verification of THz-TDS and THz imaging is performed, thus proving the applicability of THz signals in these concepts.

The screening effects that occur in a PCA are studied in [13]. Previously, we mentioned briefly the screening due to the separation of electron-hole pairs which, due to the distribution of the electrons and holes in the presence of the applied external field, create an electric field that is comparable and opposite to the applied field. The authors in [13] call this type of screening space-charge field screening, and they also describe the radiation field screening, which is caused by the current that is excited in the antenna. This current creates a magnetic field, which subsequently excites a local electric field that tends to cancel out the applied external field. It is found that the radiation field screening is the main mechanism that contributes to the saturation of the generated field amplitude with respect to the intensity of the optical illumination. Moreover, the authors identify the crucial relationship between the antenna impedance and the impedance of the photoconductor. When the time-dependent photoconductor resistance becomes comparable to the antenna impedance, they observe a voltage drop across the photoconductor that deteriorates the emission efficiency. However, they fail to recognize that under matching conditions of the antenna with the photoconductor the efficiency would be maximum, and that they should try to build a model that will target at achieving this matching.

A new model for a pulsed PCA is developed in [14]. The aim of the authors is to maximize the optical-to-

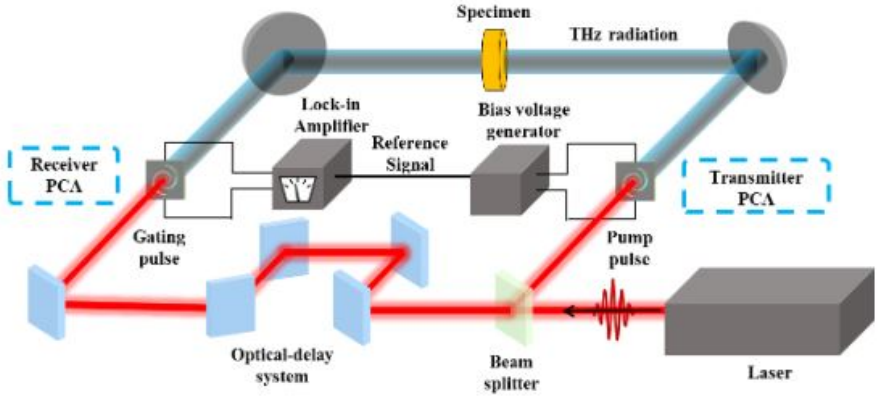

Figure 1.2: Configuration for THz time domain spectroscopy. [12, p. 3]

THz efficiency by tuning the parameters in their model. In their model, they use simple lumped components to describe the DC bias voltage, the antenna radiation impedance, the losses in the antenna and the time-dependent resistance of the semiconductor. In addition to these components, they model the separation of the electron-hole pairs and their distribution under the influence of the bias field with a time-dependent capacitance. Furthermore, they include the space-charge screening effect as a voltage-controlled voltage source that tends to counteract the applied bias voltage. Using this model, the authors demonstrate the dependence of the PCA performance on the various tunable parameters, such as the optical power, the bias voltage, the antenna impedance and the size of the excitation gap. The conclusions are that there is a positive relationship between the radiated power and the bias voltage, as well as a positive relationship between radiated power and optical power until saturation is reached. Another remarkable conclusion is that the antenna impedance does not affect the maximum achievable efficiency, but it determines the optical power that is needed in order to reach the maximum efficiency. Since the optical power is associated with the density of carriers and the semiconductor resistance, this note implies that during the design of a PCA we should choose the optical power in a way that the corresponding semiconductor resistance matches the antenna impedance, if we want to achieve maximum efficiency. Lastly, the authors recommend the use of small excitation gaps when the laser power is low, otherwise the optical-to-THz efficiency will be decreased.

A more general description of THz generation is given in [15], with an extensive description of photoconductors under pulsed illumination, though. Since many details and considerations have been already mentioned based on earlier works, we will focus on new information that will be of some use in the rest of the thesis. Firstly, low frequencies are always filtered, because practical limitations on the antenna dimensions do not allow these frequencies to be radiated as expected. Therefore, although large low-frequency components may appear in the theoretical calculations of the radiated power spectrum, in fact, there is a cut-off frequency at the detector that does not allow these components to reach the detector. Regarding material constraints, the authors distinguish them between thermal and electrical constraints. The thermal ones concern the negative effects of high-intensity laser power. Although high laser power is desirable, because it leads to high THz power, it also leads to a temperature increase that eventually causes reduction of the carrier mobility, device aging and destruction. A solution to this is the selection of materials with short lifetime, because the Joule heating is reduced. The electrical constraints are space charge screening, radiation field screening and impedance matching. The impedance matching is described as a complicated restriction, especially for high optical power levels. Under this condition the photoconductor impedance is lower than the antenna impedance directly after the pulsed illumination. Within the recombination time, the photoconductor impedance becomes approximately equal to the antenna impedance, thus achieving matching, and subsequently the former increases until it reaches the dark resistance value, which for LT-GaAs is in the order of $G\Omega$. In order to simplify the problem, the authors assume that the recombination time is much longer than the laser pulse and they compute the instantaneous conductivity of a finger structure. However, they do not provide a general methodology for any PCA structure.

In [16], the generated current in a PCA was theoretically formulated, the effects of the laser, substrate, antenna and temperature were investigated, and the theoretical results were compared with simulation results. At the analysis of the PCA, the authors refer to the screening effect and comment that for antennas with small active region the space charge screening is the dominant factor, whereas in large antennas saturation is

caused by the radiation field screening. Regarding the electrical and thermal constraints of the material, the maximum allowed values are 500 kV/cm DC bias voltage and 1 $mW/\mu m^2$ laser intensity respectively for LT-GaAs. Furthermore, the carrier lifetime should be small enough so that it leads to a high bandwidth but not too small, because that would cause a reduction in the radiated power. The authors suggest a carrier lifetime equal to 100 fs. Carrier mobility is also a feature that is associated to the peak photocurrent. As far as the mobility is concerned, it is important for the PCA designer to consider that the mobility is not constant but it increases linearly with the applied field for low bias voltages. Moreover, the authors have studied the effect of the temperature in the generated current and they have found out that including the temperature influence in the theoretical model leads to an increase of the peak value of the current as well as to longer decay time. Lastly, they observed via full-wave simulations and their theoretical model that there is a peak at the detected signal at the resonance frequency of resonant transmitter antennas.

Another approach for a theoretical model is given in [17] and [18]. A Norton equivalent circuit is developed, which basically means that the information of the photoconductor, the laser pulse and the bias voltage is expressed with a simple circuit that includes an equivalent current source and an equivalent impedance. The antenna impedance completes the equivalent Norton circuit as the load impedance. With this approach it is straightforward for the designer to maximize the efficiency of the PCA, when the antenna impedance is known, by selecting the parameters of the photoconductor and laser in such a way that the Norton impedance is matched to the antenna impedance. Three different antenna configurations are used, for which the antenna impedances are calculated as functions of frequency via simulations. Although the model does not take into consideration the screening effects and the dependence of the generated current on the temperature, the results for the detected power and the energy spectral density are verified experimentally. The authors have also tried in later works to refine the model and make it more accurate. The works in [17] and [18] will be the grounding foundation of the thesis, as this Norton equivalent circuit will be used for the design of a PCA.

Research on increasing the efficiency of PCAs has been going on also in more recent works. In [19], an enhancement in the efficiency for either polarization of the optical beam and the bias voltage as well as a reduction in screening was accomplished through the surface patterning of the semiconductor with small holes. Equivalently, Burford, Evans and El-Shenawee [20] added a thin layer of nanodisks on top of the LT-GaAs substrate in order to increase the radiated power. The enhancement in the performance of a PCA from plasmonic nanostructures at the semiconductor surface was experimentally verified in [21] as well. Specifically, an Au-grating was added to a PCA and the increase in the efficiency was observed. Lastly, in [22] the authors addressed the low dark resistivity of photoconductors able to work at 1550 nm, by creating a bias-free PCA. With their design they managed to transmit 72 μW for an optical power of approximately 350 mW. These works have identified a different approach for achieving better efficiency in a PCA, therefore the combination of implementing the proposed solutions with the Norton model of [17] could accomplish even better results. However, in this thesis, we do not take these solutions into account, because changing the configuration of the conventional PCA would lead to an amendment in the equations of the Norton model.

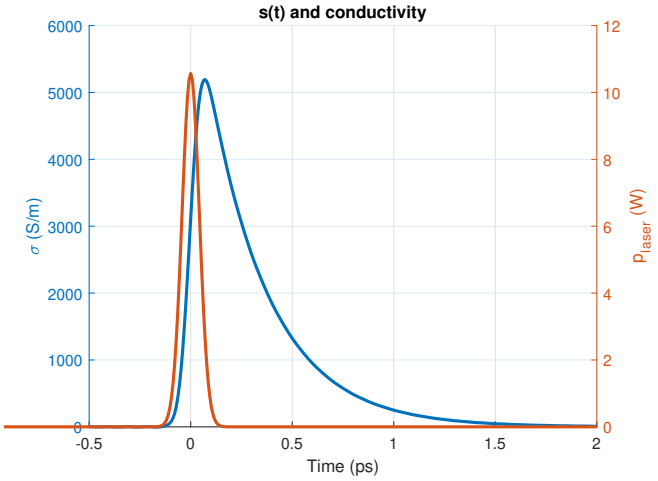

Figure 1.3: Conductivity and laser power as a function of time

Parameter name	Value
Gap size $W_x \times W_y$	$1\,\mu m \times 1\,\mu m$
Thickness of substrate W_z	$2\,\mu m$
Mobility μ	$420\,cm^2 V^{-1} s^{-1}$
Absorption coefficient α	$10^6 m^{-1}$
Laser frequency f_{laser}	385 THz[1]
Frequency associated with bandgap of semiconductor f_g	344 THz[2]
Average laser power P_{ave}	$90\,\mu W$
Laser power spatial distribution	Gaussian with -3 dB diameter $D_{laser} = 1\,\mu m$
Laser power temporal distribution	Gaussian with pulse width $\tau_p = 100\,fs$
Repetition frequency of laser f_p	80 MHz
Carrier lifetime τ	$0.3\,ps$
Relative permittivity of GaAs $\epsilon_{r,GaAs}$	13

Table 1.1: Values of the parameters for computation of the conductivity displayed in Fig. 1.3

1.1.2. Equivalent Circuit of Pulsed Wave PCAs

As mentioned before, the theoretical background in the thesis is based on [17], which proposes a Norton equivalent circuit to model the phenomena that take place at a pulsed wave PCA. In [17], the author gives analytical expressions for the conductivity $\sigma(\vec{r}, t)$ and the conductance $g(t)$ of the photoconductor, the laser power density, the Norton equivalent source current and the Norton equivalent impedance. These are mentioned and described in [23] as well, and are given in Appendix A.1 for easiness of reading.

The spatial mean conductivity $\sigma(t)$ of a LT-GaAs substrate is given in Fig. 1.3. The results are derived according to the expressions in the Appendix A.1. The values of the various parameters that contribute to the conductivity are in agreement with the values that are used in the rest of the thesis and they are given in Table 1.1. From the figure we observe the ps duration of the conductivity, and consequently of the excited current, as it has been described in the literature, which ultimately leads to a broadband THz pulse. Once the conductivity has been determined, the computation of the Norton current and Norton impedance is straightforward.

1.1.3. Photoconductive Connected Arrays

Photoconductors can be used as an excitation for a single antenna, as it has been assumed before, but the resulting PCA will probably have limited directivity which is determined by the radiation properties of the antenna. To improve the directivity we can design an array of antennas. The antenna elements can be of any type; however, resonant antennas, such as half-wave dipoles or slots are not suitable for broadband operation, because their impedance varies significantly with respect to the frequency and matching with the equivalent Norton impedance cannot be accomplished for the whole frequency band. Instead, broadband antennas have a steady impedance and are more desirable for broadband applications. The connected dipole or the connected slot antenna arrays provide such capabilities [24] and have been, thus, already used in photoconductors [25]. These structures are called photoconductive connected arrays (PCCAs).

The general structure of a PCCA, as it has been modeled in [25], is presented in Fig. 1.4. It consists of a connected array of dipoles or slots that are placed on a LT-GaAs substrate. The array is illuminated by a laser pulse. A microlens array focuses the laser on the excitation gaps of the dipoles or slots, so that all optical power is used for the change of conductivity in the area of interest. In [23], the PCCA configuration that will be the focus of this thesis is designed theoretically and optimized. The process that was followed to get the design parameters are also presented shortly in Appendix A.4.

Once we have described the photoconductive part of the antenna with the equivalent circuit mentioned in Section 1.1.2, the radiation of the PCCA can be calculated according to [26]. Specifically, the Norton circuit at each excitation gap of the array should be converted to Thevenin circuit and subsequently the expressions for active input impedance of the array, the equivalent current along the dipoles and the far field are very similar to [26]. These expressions for the far field from a PCCA are presented in Section 2, which is about the radiation of the array.

[1] This frequency corresponds to a wavelength $\lambda_{laser} = 780$ nm, which is the laser wavelength that is available from the THz spectrometer in the facilities of TU Delft.

[2] For this frequency f_g, the energy bandgap is $E_g = hf_g = 1.42\,eV$, which is the energy bandgap of GaAs. h is the Planck's constant, $h = 4.1357 \cdot 10^{-15}\,eV \cdot s$

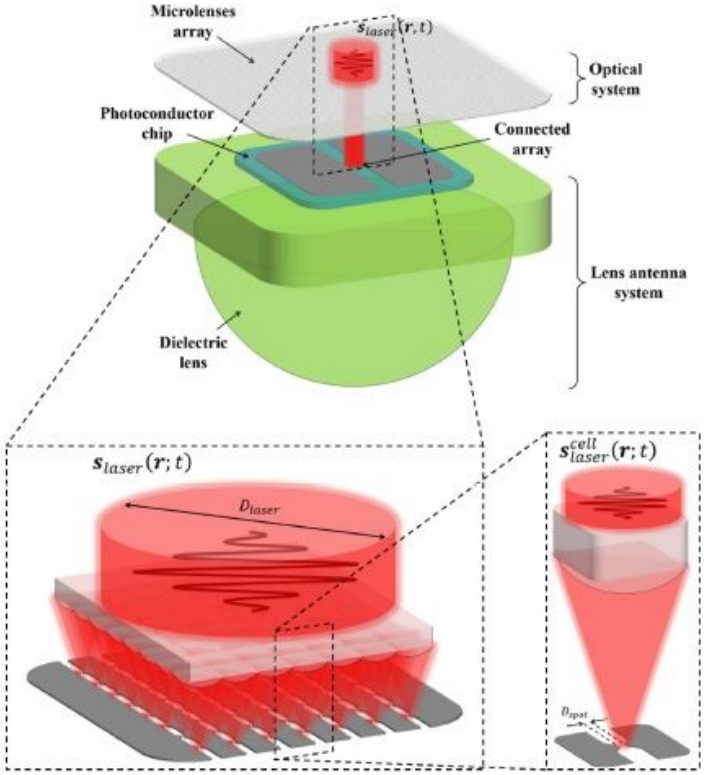

(a) Full structure of the PCCA [25, p. 222]

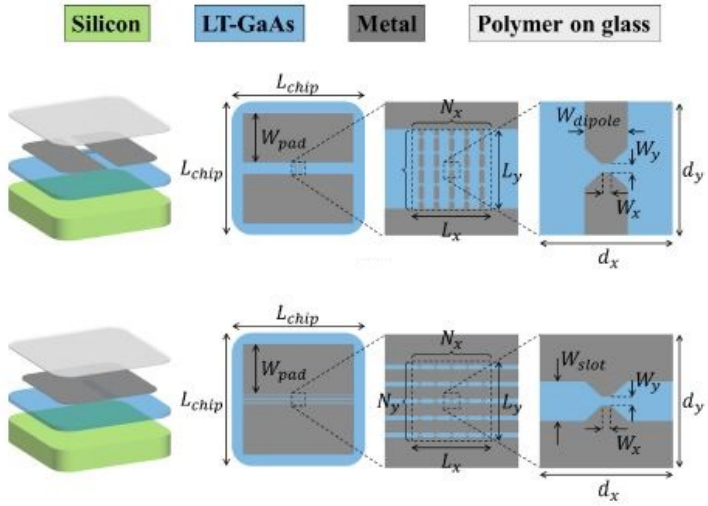

(b) Stratification and antenna elements of the PCCA [25, p. 224]

Figure 1.4: Structure of the PCCA

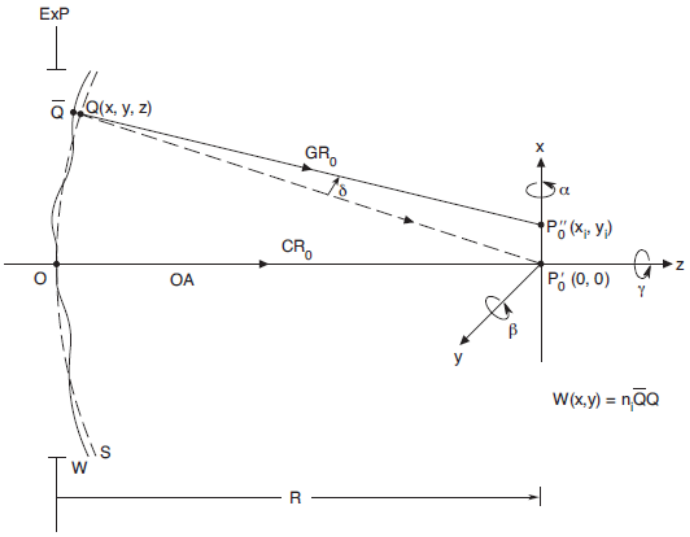

Figure 1.5: Aberrated ray focusing on a different point than the expected focal point [28, p. 144].

Part of the thesis will be dedicated to the fabrication of the PCCA, thus it is important to explore some common fabrication techniques for the different components of the PCCA. Definitely one of the most cumbersome processes is the fabrication of the microlens array, because of the high accuracy that is required for structures whose size is only a few μm. In [27] the most prevalent fabrication methods for microlenses are presented. They are categorized in direct and indirect methods. A direct method is the thermal reflow, during which cylinders of photoresist are created and heated to form a spherical structure for the microlens. Other direct methods are the microplastic embossing, during which external pressure is exerted on a polymer substrate that is located between heating plates and a silicon mold and subsequently the polymer is slowly cooled to formulate the microlens; and the microdroplet jetting method, at which droplets of UV-polymerizable liquid are UV-exposed to create the microlens. The indirect methods require a mold to shape the microlens. The mold can be fabricated with isotropic etching on wafer that creates the concave mold or with ultraprecision machining.

The fabrication of the lenses in such small dimensions with the aforementioned methods is very likely to lead to a deviation of the final result compared to our theoretical model, as the solidification process of the liquid photoresist which takes place during the formulation of the spherical (or elliptical) shape of the microlens is not totally controllable by us. Such fabrication errors can lead to aberration [28] during operation of the PCCA, which means that the laser rays will not focus at the same point (the focal point) which is supposed to be the center of the excitation gap of the dipole. This effect may degrade the performance of the PCCA, so it is important that we estimate the aberration.

The aberration can be quantitatively described with the aberration function $W(x,y)$ that expresses the difference between the wavefront of the aberrated wave and a reference sphere. In the PCCA configuration designed in [23], the microlenses have an elliptical shape and the reference sphere could be the FO sphere that corresponds to the wavefront of the incident wave after transmission through the lens surface in the absence of aberration. The schematic displaying the wavefront and the reference sphere is given in Fig. 1.5. The aberration function is defined as $W(x,y) = n_i\bar{Q}Q$, where n_i is the refractive index of the medium, $\bar{Q}$ is a point on the wavefront that is intersected by an incident ray and Q is a point on the reference sphere intersected by the same ray.

There are different types of (monochromatic) aberration that are likely to emerge due to fabrication errors. The aberration function, expressed in polar coordinates, can be expanded into a series of Zernike polynomials $W(\rho,\theta) = \sum_{n=0}^{\infty}\sum_{m=0}^{n} c_{nm}Z_n^m(\rho,\theta)$, where $Z_n^m(\rho,\theta)$ are the Zernike polynomials and c_{nm} are orthonormal coefficients that depend on $W(\rho,\theta)$. Each Zernike polynomial corresponds to a type of aberration such as piston, distortion, defocus, primary astigmatism, primary coma etc. [28]. If we know the dominant terms in the Zernike series expansion of the aberration function, we can characterize the aberration and understand the effect that the fabrication errors will cause to the incoming laser beam.

Another important component of the structure is the connected dipole array. The dipoles are fabricated on semiconductor wafers, which, according to the aforementioned literature on photoconductors, are made

of GaAs. A typical size of a GaAs wafer is 2 inches in diameter and 450 μm in thickness [29], but larger wafers are also very common nowadays. Due to the small dimensions and the sensitivity of the structure to dust and other nanoparticles, the fabrication of the connected dipole array needs to abide by a standard microelectronics fabrication procedure in a cleanroom. The first step in the fabrication of the PCCA is the low-temperature growth of GaAs via a method named epitaxy, which is in this case simply the extension of the initial substrate material by growing the same material, while preserving the original lattice (autoepitaxy). Epitaxy can be performed with various processes, such as molecular beam epitaxy, vapor-phase epitaxy or liquid-phase epitaxy [30]. While epitaxy usually occurs in high temperatures, because at high temperatures the crystal quality is better and the growth is faster [30], for our purpose the low-temperature growth has more advantages for the properties of the photoconductor. As LT-GaAs wafers are already available in the market, it is not necessary that we perform the epitaxial growth in the cleanroom.

The next step in the fabrication of the dipole is typically the printing of the antenna patterns. These are printed on the wafer via lithography. During lithography, the wafer is coated with photoresist, which is basically, according to [29], a resin with added photoactive compound (PAC) and a solvent. The PAC regulates the rate at which the photoresist dissolves, which is different when the resist is exposed to light compared to the non-exposure state. The solvent is responsible for the viscosity of the resin and preserves the liquid state of it [29]. There are two types of photoresist, namely positive and negative resist. For a positive resist, the PAC is an inhibitor before exposure and a sensitizer during exposure, whereas for a negative resist it is the opposite [29]. Lithography is based on this property of the photoresist when reacting with light. A photomask with the antenna pattern is placed between the light source and the coated wafer. For a positive photoresist, the photomask allows light to illuminate the wafer only at the points determined by the antenna pattern. For a negative photoresist, the photomask prevents light from illuminating the wafer only at the points determined by the antenna pattern. After exposure, the wafer is rinsed in a developer that dissolves the dissolvable parts of the photoresist [30]. The result is a layer of photoresist with some gaps that follow the antenna pattern.

The parts of the wafer that are no longer coated with photoresist can now be etched, so that they are later filled with metal, such as aluminum and finally form the antenna. There are two types of etching, wet and dry etching. The most prevalent type is the dry etching, because of the disadvantages of wet etching, which are the isotropical etching, lack of control of the process and particle contamination [29]. Dry etching, or plasma etching, is based on the bombardment of the wafer surface by ions [29]. Although not as selective as the chemicals at wet etching, the ions have some selectivity in terms of which material is etched faster; therefore, by selecting a proper gas to ionize, we can etch the exposed GaAs surface at the desired depth without etching completely the resist and thus not affecting the GaAs beneath the resist whatsoever. The remaining resist, which is of no use after the etching, can be removed by a wet chemical solvent or via plasma oxidation. The step of resist removal is called stripping [30].

The metal layer is deposited on the wafer through the sputtering process. The metal to be deposited is contained in the plasma chamber of the sputtering equipment above the wafer. High-energy ions are created, similarly to the etching process; however, instead of reaching the wafer, the ion flux strikes the metal [29]. Due to this bombardment by the ions, the metal target breaks into tiny pieces that are deposited uniformly on the wafer. Since we do not want to have metal everywhere on the wafer, but only on selected parts of it which correspond to the dipoles and also maybe the feeding lines, we need to remove the metal from the undesired areas of the wafer via lithography and etching. The lithography and etching procedures are similar to what was described before. When the connected dipoles are finely formed on the wafer amd there are no undesired residues, we can move on and print the microlens array on top of them through one of the procedures described above. The final result will be the integrated PCCA with the microlens array attached to the rest of our structure.

This whole process for the fabrication of the connected dipole array is presented in Fig. 1.6. This schematic is a general overview that takes into account typical steps followed during the fabrication of any integrated circuit in a cleanroom. The exact methodology for the particular PCCA investigated within this thesis may differ slightly based on the specifications and will be thoroughly described in the flowchart of the fabrication. However, the rationale and the principles are the same as the state of the art presented in the paragraphs above.

The last component of the structure is the silicon lens. In [25] the authors used a hyperhemispherical lens, which has been already described in Fig. 1.1, but with the more specific definition that sets the extension length to be equal to R/n, where R is the radius of the hemisphere and n is the refractive index of the material. The advantage of the hyperhemispherical lens compared to other shapes, such as the common elliptical shape, is the constant directivity of the radiated field outside of the lens and the high efficiency in terms

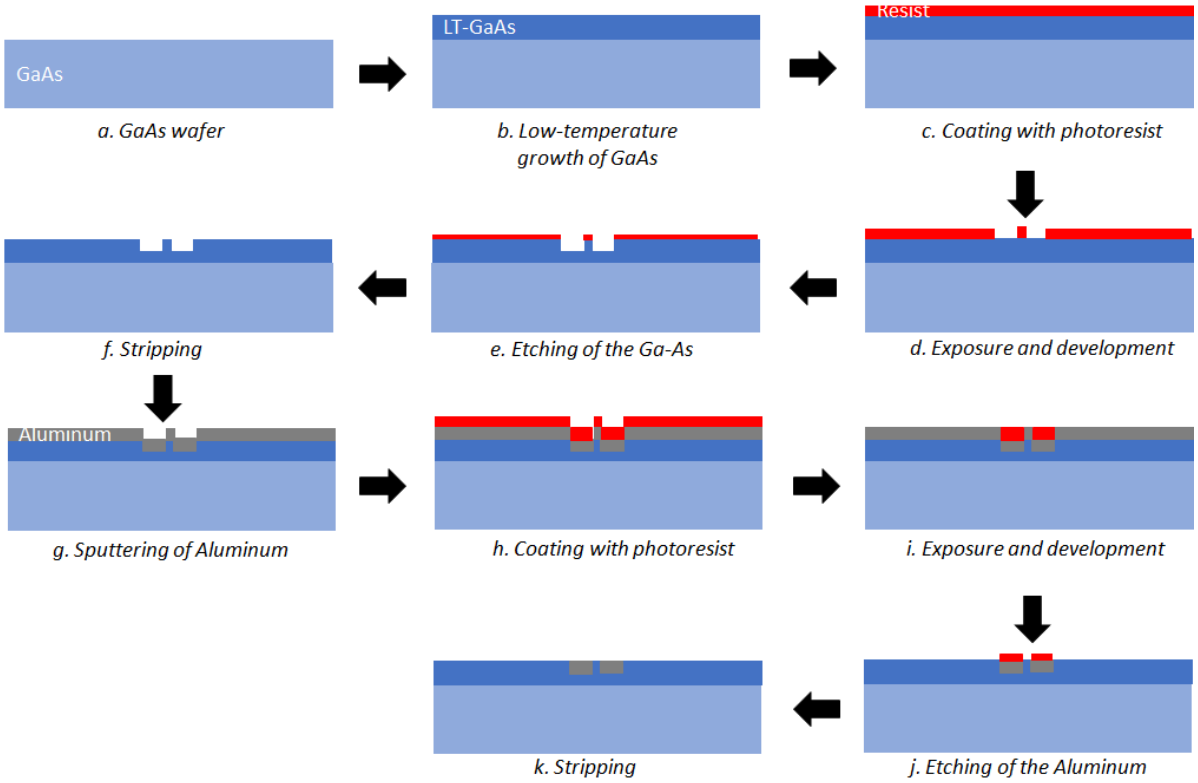

Figure 1.6: Fabrication procedure of the PCCA

of pattern coupling to the electric field of a Gaussian beam [31]. The usefulness of the silicon lens in the configuration presented in the thesis will be shown later in Chapter 2.2.

1.1.4. Transmission through the QO path

The THz signal, after its transmission through the silicon lens, travels along the quasi-optical (QO) path of the THz-TDS setup to the detector. The QO path is presented in Fig. 1.7, where we observe the transmitting antenna which consists of the laser pulse, the micro-lens array, the connected dipole array and the silicon lens; a convergent lens antenna whose role is to focus the THz signal at the detector; and the receiving antenna, which is displayed to be of the same type as the transmitting antenna, but can be any antenna, as long as it can efficiently receive the broadband THz signal. Ideally, the receiving antenna shall be such that the reaction integral of the incoming field and the current of the receiving antenna when used in transmission $-\iint_{S_{Rx}} \vec{e}_{oc} \cdot \vec{J}_0^{tx}\, dS$ is maximized for the frequencies of interest.

The focusing lens within the QO path between the transmit and receive antenna receives a spherical wave originated by the transmitter and is supposed to create another spherical wave whose rays focus on a point - the focal point - where the receive antenna will be placed. The incoming spherical wave can be approximated with a plane wave provided that the source is, theoretically, at infinite distance from the lens, or, practically, very far from the lens. The shape of the lens can be anything that corresponds to a convergent lens, which according to [32], is one of the shapes shown in Fig. 1.8.

Assuming that the surfaces of the lens are rotationally symmetrical about the same axis, as these shown in Fig. 1.8 and that the axial thickness of the lens t is not negligible, the focal distances of the source and the image can be calculated according to [32]. Specifically, the focal distances of the source f and the image f' are proven to be equal and expressed as

$$f = f' = -\frac{nr_1r_2}{\Delta}$$

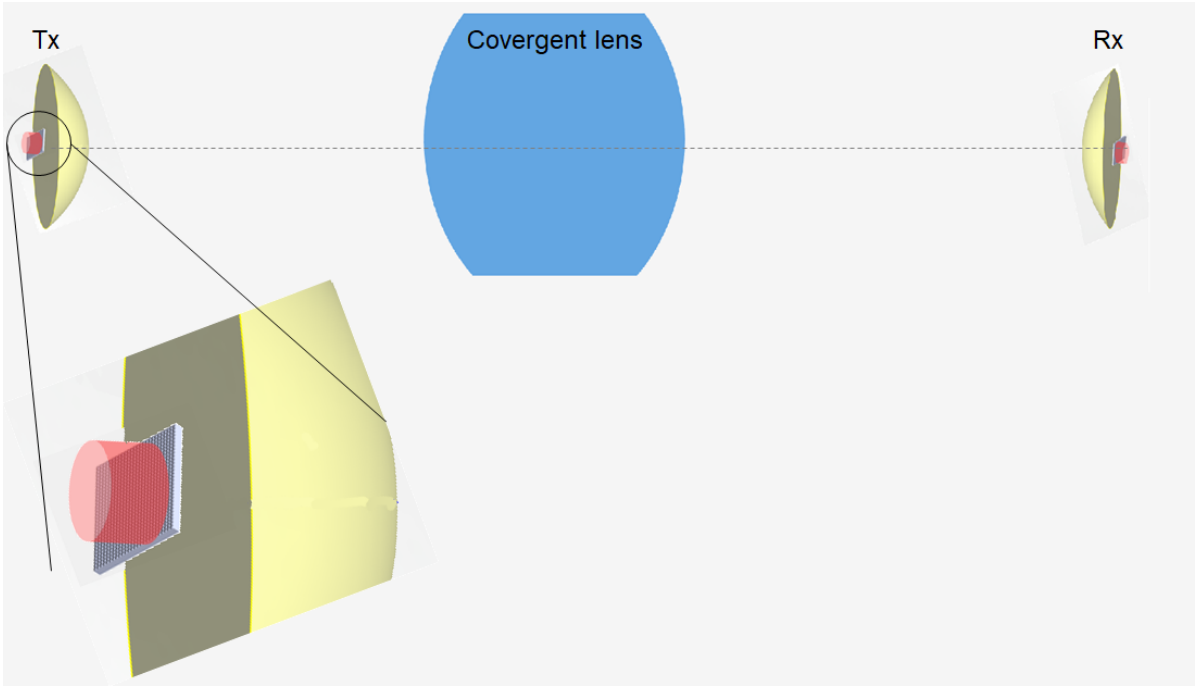

Figure 1.7: Setup for radiation of the PCCA through the QO path until the detector

Figure 1.8: Different typesof convergent lenses. Left: double convex, center: plano-convex, right: convergent meniscus

where

n is the refractive index of the lens material
r_1 is the radius of curvature of the surface towards the source
r_2 is the radius of curvature of the surface towards the image
$\Delta = (n-1)[n(r_1 - r_2) - (n-1)t]$

More detailed description of the optical parameters of the lens are given in [32].

1.2. Contribution of this thesis

The aim of this thesis is to work towards a prototype of a PCCA that can be used for the transmission and reception of broadband signals reaching frequencies up to 5 THz with a high efficiency, compared to other state-of-the-art solutions. In order to achieve it, we need to fabricate the theoretically designed PCCA of [23] and assess the feasibility of accurately fabricating this antenna. The preparation of the thesis involves familiarization with the tools that are used for the fabrication of the PCCA, such as 3D printers of nanostructures and photolithography tools, as well as compatible software therefor.

A second contribution of the thesis is the theoretical characterization of the PCCA in terms of the radiated field from the feed and from the lens antenna, assuming a THz lens similar to the one used in [25]. For the latter we developed a Matlab App that automatically calculates the secondary fields of a lens antenna if the primary field of the feed is known.

1.3. Outline of the thesis

The outline of the thesis is the following:

- Chapter 2 consists of an analysis of the primary field, which is the field radiated directly by the PCCA, as well as the secondary field of the transmitter, which is the field after transmission through the silicon lens.
- Chapter 3 describes the fabrication of the various components of the PCCA. Focus is given at the microlens array and the connected dipole array, whose fabrications are the most challenging.
- Chapter 4 presents the Matlab App that has been developed to compute the fields radiated by the lens antenna.
- Chapter 5 summarizes the work of the thesis and gives some concluding remarks and recommendations for the future.

In addition to the chapters of the main body of the thesis, the thesis includes appendices. Appendix A is based on [23] and provides all necessary background knowledge that is required for the full understanding of the thesis and the rest of the appendices complement the topics covered in the thesis.

2

Antenna Radiation

The first step in the fabrication of an antenna is definitely the theoretical analysis of its properties, such as the calculation of the radiation patterns, the efficiency and the directivity or gain. This allows us to do an optimization on the dimensions of the antenna and have expectations for the measurements that we will acquire from the fabricated prototype. Our lens antenna consists of two parts, the feed and the silicon lens, which we can study separately.

2.1. Radiation of the PCCA

In this section we will try to theoretically estimate the electromagnetic field that is radiated by the PCCA. As mentioned in the introduction, the dimensioning of the PCCA has already been done in [23]. Note that for the optimization we kept some parameters of the PCCA, which are mentioned in Table 1.1, fixed, while we tuned the periodicity of the array, the number of array elements, the width of the dipoles and the angle of tapering. The structured configuration, similar to the one presented in Fig. 1.4, is given in Fig. 2.1. In the figure, the silicon part corresponds to a mm-sized hyperhemispherical silicon lens that has the connected dipole array as feed. The tuned dimensions are given in Table 2.1.

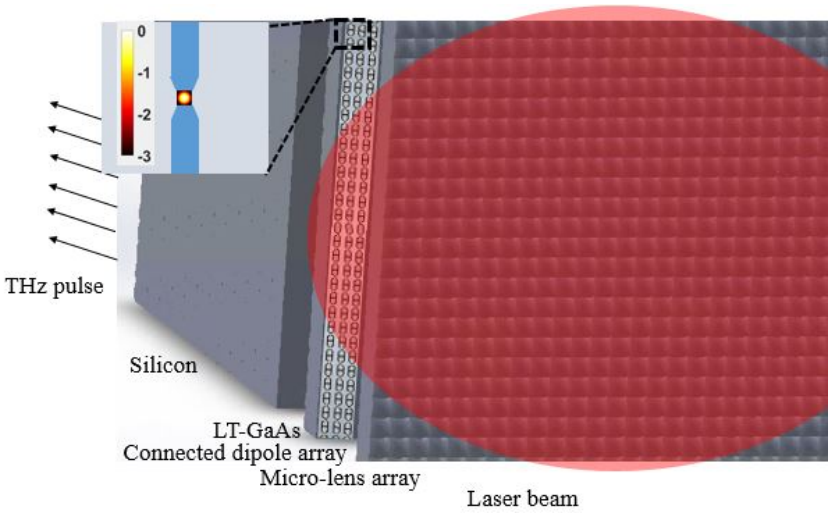

Figure 2.1: Configuration of PCCA with the integrated microlens array.

Parameter	Selected value
Number of elements N	1296 (36×36 in a 2D square array)
Periodicity d_{period}	15 μm
Dipole width W_{dipole}	8 μm
Angle of tapering α	$\approx 109°$

Table 2.1: Selected parameters for PCCA

2.1.1. Assumptions

What is of interest with respect to the electric and magnetic field radiated by the PCCA is the computation of the fields at the boundary between the silicon lens and the air. This will enable a further investigation of the secondary fields that are radiated beyond the lens, via the PO tool developed in the THz Sensing (TS) group, which is elaborated in the following section.

In order to compute the fields theoretically, we make the following approximations and assumptions, which yield the computation easier, without, however, degrading the validity of the results.

- *The boundary of the lens is in the Fraunhofer (far field) region of the PCCA.*

This is valid for low frequencies, where the distance of the PCCA from the boundary is larger than $r = \frac{2D^2}{\lambda}$, with λ the wavelength and D the maximum dimension of the antenna, which is the limit for the far field region. For example, at 200 GHz, the wavelength in silicon is $\lambda = 435\,\mu$m. For a square array, D is the diagonal and is equal to $D = \sqrt{L_x^2 + L_y^2} = L_x\sqrt{2} = 764\,\mu$m, therefore $r = 2.68$ mm. The size of the lens can be made such that up to roughly 2.5 THz its interface with the air is in the far field region. However, if we consider this condition to hold for higher frequencies as well, the distance r becomes larger and the fabrication of a lens with a size in the order of cm does not offer many benefits.

Here it is important to mention that there is a minimum frequency for which the PCCA will operate as expected, because for low frequencies the PCCA size is electrically very small and edge effects due to the finiteness of the array become dominant. Probably, as was mentioned in the literature, there will be a cut-off frequency at the receiver, so the receiver will filter the low undesirable frequencies. For the transmission, we consider that the PCCA will behave as expected when its size L_x, L_y is at least comparable to one wavelength. Therefore,

$$L_x \geq \lambda \Rightarrow \lambda_{max} = L_x \Rightarrow \frac{c_0}{f_{min}\sqrt{\epsilon_r}} = L_x \Rightarrow f_{min} = 161 \text{ GHz}$$

- *For the calculation of the far fields we consider the finiteness of the array along the x-direction and apply the windowing approximation along the y-direction.*

If we ignore for the moment the tapering of the dipoles, the electric field is equal to

$$\vec{E}(r,\theta,\phi) = jk_z\mathbf{G}^{ej}(k_x,k_y)I(k_x)J_t(k_y)\hat{x}\,AF_y\,e^{jk_z|z|}\frac{e^{-jk_d r}}{2\pi r} \tag{2.1}$$

where

$$I(k_x) = \mathscr{F}\{i(x)\} = \frac{sinc\left(\frac{k_x W_{gap}}{2}\right)}{D_l(k_x)}\Big(-\sum_{n_x=0}^{N_x-1} v_{0,n_x}e^{jk_x n_x d_x} + \sum_{n_x=0}^{N_x-1} Z_{l,n_x} i_{\delta,n_x} e^{jk_x n_x d_x}\Big) \tag{2.2}$$

$$\text{with } D_l(k_x) = \frac{1}{d_y}\sum_{m_y=-\infty}^{\infty} G_{xx}^{ej}(k_x,k_{ym})J_0\Big(\frac{k_{ym}W_{dipole}}{2}\Big)$$

$$J_t(k_y) = \mathscr{F}\left\{j_t(y)\right\} = \mathscr{F}\left\{\frac{2}{W_{dipole}\pi}\frac{1}{\sqrt{1-\left(\frac{2y}{W_{dipole}}\right)^2}}\right\} = J_0\Big(\frac{k_y W_{dipole}}{2}\Big)$$

$$AF_y = \sum_{n_y=0}^{N_y-1} e^{j(k_y-k_{y0})n_y d_y}$$

In Eq. 2.2, the terms v_{0,n_x} and Z_{l,n_x} are the Thevenin voltage and impedance in the equivalent Thevenin circuit that excites the $n_{x_{th}}$ gap of the connected dipole array. In [23] we have characterized the excitation circuit

for each gap with an equivalent Norton circuit, whose transformation to a Thevenin circuit is straightforward by defining

$$\begin{aligned} v_0 &= I_{Norton} Z_{Norton} \\ Z_l &= Z_{Norton}. \end{aligned} \tag{2.3}$$

Obviously, due to the non-uniform laser illumination of the gaps in the array, the Norton impedance, and hence the Thevenin impedance Z_{l,n_x}, is different for each of the n_y rows of the array. However, we will assume that the laser pulse uniformly illuminates the array, because for such configuration the derived theoretical results turn out to be more accurate.

After having determined the electric field, the magnetic far field is simply given by the expression

$$\vec{H}(r,\theta,\phi) = \frac{1}{\zeta_d} \hat{r} \times \vec{E}(r,\theta,\phi)$$

- *The surroundings of the antenna is a stratified medium as shown in Fig. 2.1.*

This assumption means that the spectral Green's function is computed according to Appendix B. From Eqs. 2.1, 2.2 and B.1-B.3, we observe that there may be poles due to the stratification of the antenna. From Eq. 2.2, we see that the poles occur for those spectral components k_x for which $D_l(k_x) = 0$, whereas from Eqs. B.1-B.3 we observe poles emerging when the denominator of the right hand side expression of either Eq. B.2 or B.3 is equal to 0. Due to the stratification, we expect leaky wave poles, which are complex numbers and are contained in the bottom Riemann sheet. The leaky waves do not arrive to infinity and therefore are not radiated to the far field, however, they are important because they shape the far field pattern.

The tapering of the dipoles poses an issue for the radiated electric field, because the theoretical expressions for the current of a connected dipole prerequisite a uniform width for the dipoles, while, in fact, the current along y is more accurately written as $j_t(x,y) = \frac{2}{w_d(x)\pi} \frac{1}{\sqrt{1-\left(\frac{2y}{w_d(x)}\right)^2}}$, where $w_d(x)$ is a periodic function with period d_x and its expression is

$$w_d(x) = \begin{cases} W_{gap} & ,|x| \le \frac{W_{gap}}{2} \\ 2\frac{W_{dipole}-W_{gap}}{W_{gap,untap}-W_{gap}}(x-\frac{W_{gap}}{2}) + W_{gap} & ,\frac{W_{gap}}{2} \le |x| \le \frac{W'_y}{2} \\ W_{dipole} & ,\frac{W'_y}{2} \le |x| \le d_x - \frac{W'_y}{2} \end{cases} \tag{2.4}$$

The utilization of Eq. 2.4 in the expression of the edge singular current along y has the difficulty that the current along x, $i(x)$ cannot be separated from the current along y, $j_t(x,y)$ and therefore we cannot derive an expression for the unknown current spectrum $I(k_x)$ as the one in Eq. 2.2.

As a result, we need to approximate the actual dipole structure with a simpler one, which will consist of dipoles with uniform width. In order to find the most suitable dimensions of the equivalent dipole, we did a parametric analysis, in which we compared to active input impedance of dipoles with various widths and gap sizes to the original tapered one. From the parametric analysis we derived optimal values for the equivalent dipole $W_{dipole} = 6\mu m$ and $\delta_{gap} = 3\mu m$, as shown in the inset of Fig. 2.2.

The active input impedance for this selection of dimensions is given in Fig. 2.2 in comparison with the active input impedance of the original tapered dipole dimensions. We observe that, at least for frequencies up to 3 THz, the active input impedances of the two structures are quite close. For better accuracy, the difference of the impedances can be integrated in the Thevenin circuit of each excitation gap, by adding it to the Thevenin impedance Z_l defined in Eq. 2.3. The updated Thevenin impedance is shown in Fig. 2.3.

In the rest of this section we will find the far field for this connected dipole array, according to Eq. 2.1, with the constant width given before. We will assume that the derived radiation patterns are quite close to the actual patterns. In order to validate the accuracy of the patterns, we will compare the derived theoretical results with patterns acquired via CST.

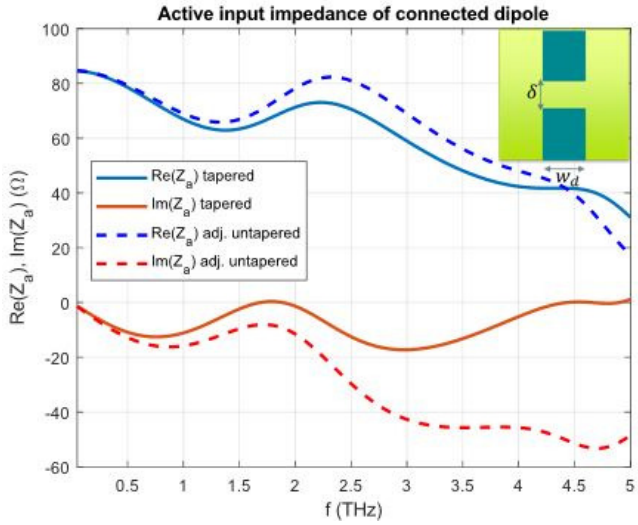

Figure 2.2: Comparison of active input impedances of a connected dipole array with uniform dipole width and a connected dipole array with the tapering close to the excitation gaps

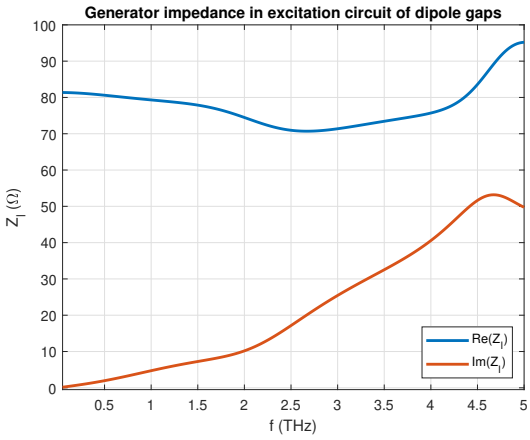

Figure 2.3: Thevenin impedance in the circuit of the excitation gaps of the connected dipole array, when the equivalent Norton impedance calculated according to Eq. A.2 is equal to 81Ω

2.1.2. Active input impedance of finite array

In order to find the far field radiated by the connected dipole antenna, we need to first calculate the average currents along the excitation gaps i_{δ,n_x}, which are necessary for the computation of the current spectrum $I(k_x)$, as it can be noticed in Eq. 2.1 and Eq. 2.2. Under the assumptions of uniform excitation of the array and uniform dipole width, these currents can be specified according to [26], as

$$\mathbf{i}_\delta = [\mathbf{I} + Z_l \mathbf{Y}]^{-1} \mathbf{Y} \mathbf{v}$$

where $\mathbf{i}_\delta$ is the vector with the excitation currents on all gaps of the array along one row, which is indicated by the red box in Fig. 2.4, $\mathbf{I}$ is the identity matrix, Z_l is the generator impedance given in Fig. 2.3, $\mathbf{Y}$ is the mutual admittance matrix and $\mathbf{v}$ is the vector with the excitation voltage in each gap along one row. The mutual admittance matrix is defined as a matrix whose element in the $\{n_x, n'_x\}$ position is

$$Y_{n_x,n'_x} = \frac{1}{2\pi} \int_{-\infty}^{\infty} \frac{-sinc\left(\frac{k_x \delta}{2}\right)}{D_l(k_x)} e^{-jk_x(n_x - n'_x)d_x} dk_x$$

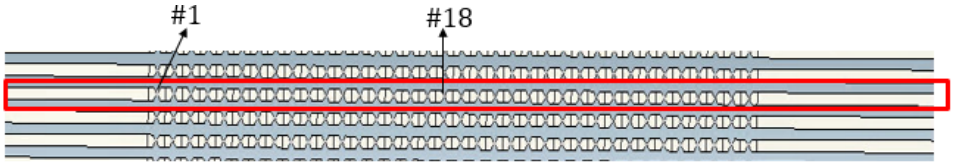

Figure 2.4: Part of the PCCA where we indicate one row and the elements #1 and #18

The calculation of the excitation currents enables us to find the active input impedance of each dipole depending on each position in the row, therefore, taking into account the finiteness of the structure. As mentioned before, each dipole in the array is considered to be the load impedance in a Thevenin circuit. For better comprehension we give the Thevenin circuit representation for a dipole in the position n_x in Fig. 2.5. The active input impedance is, according to the figure, $Z_{n_x,act} = \frac{v_{n_x}}{i_{\delta,n_x}} - Z_l$. The results of the active input impedance calculation for the dipoles in the positions 1 and 18 are shown in Fig. 2.6. We observe that the central element is characterized by an active input impedance very similar to the the active input impedance of the infinite array. On the other hand, the corner element is affected by edge effects and has an active input impedance that differs from the case of the infinite array.

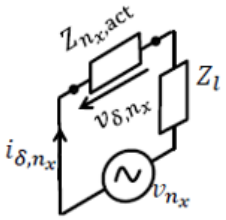

Figure 2.5: Feeding circuit of the excitation gap in the $n_x th$ position. [33]

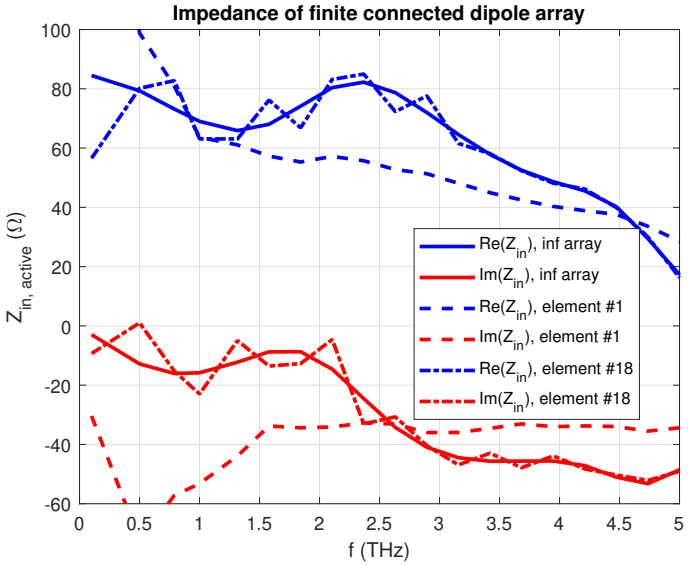

Figure 2.6: Input impedance of finite connected dipole array. The element in the corner of the array (element #1) and in the centre of the array (element #18) are compared with the active input impedance of an infinite array

2.1.3. Equivalent current along dipoles

The equivalent current along the dipoles is given, in its spectral form, in Eq. 2.2. From this expression, we can get the equivalent current in the spatial domain simply by implementing an inverse Fourier transform.

Fig. 2.7a shows some results from the investigation of the poles originating from the zeros of the denominator in the current spectrum expression at 5 THz. For completeness, we also show in Figs. 2.7b and 2.7c similar results from the TE and TM poles originating from the spectral Green's function at 5 THz. The poles are estimated by locating the local maxima, which are shown as bright points at the subfigures of Fig. 2.7. The estimated values are denoted as k_ρ^{guess}. A more accurate value of the leaky wave pole guessed in the beginning is acquired by applying the Newton-Raphson method iteratively until we have convergence of the solution. The convergence is accomplished via the following algorithm:

1. $k_\rho^{(1)} = k_\rho^{guess}$

2. $k_\rho^{(2)} = k_\rho^{(1)} - \frac{D_l(k_\rho^{(1)})}{D_l'(k_\rho^{(1)})}$

3. if $|k_\rho^{(2)} - k_\rho^{(1)}| <$ threshold
   $k_\rho = k_\rho^{(2)}$
   else
   $k_\rho^{(1)} = k_\rho^{(2)}$
   go to step 2

For lower frequencies the procedure is similar. We guess the leaky wave pole assuming a linear relationship of the leaky pole with frequency, which means that for the $i-th$ frequency, the guessed leaky pole value is $k_{\rho,i}^{guess} = k_{\rho,i+1} \cdot \frac{k_{d,i}}{k_{d,i+1}}$ and subsequently we refine the guess point via the aforementioned Newton-Raphson algorithm. In the subfigures of Fig. 2.7, we observe a number of leaky poles. In Fig. 2.8 we have selected one pole from each subfigure and show the dispersion of their real and imaginary parts over the frequency.

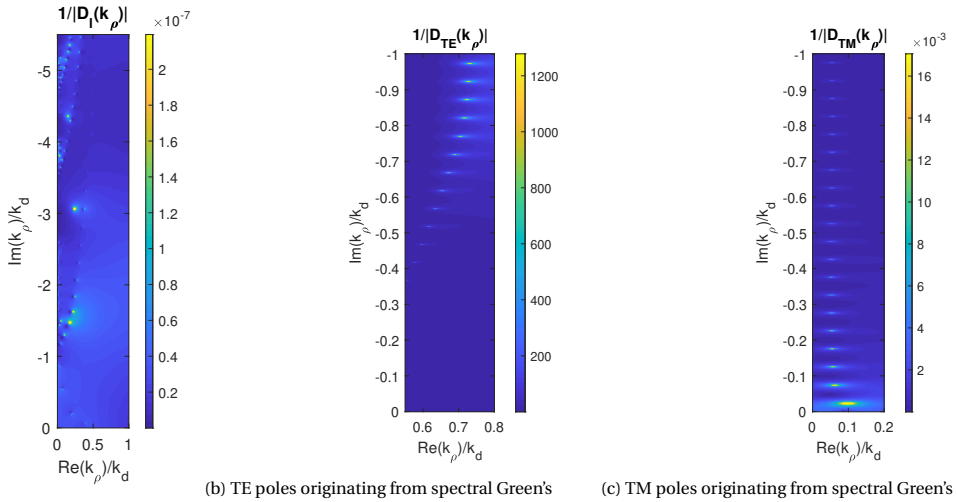

(a) Poles originating from current spectrum

(b) TE poles originating from spectral Green's function

(c) TM poles originating from spectral Green's function

Figure 2.7: Leaky poles at 5 THz

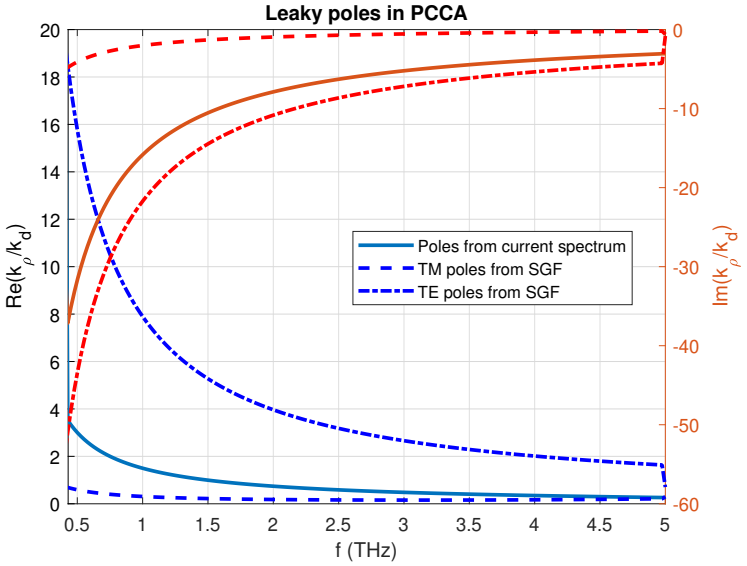

Figure 2.8: Real and imaginary part of a leaky pole as a function of frequency.

Once we have identified the leaky poles in the current spectrum, we can plot it for different frequencies and explain the results. Subsequently, as mentioned before, the current in the spatial domain is the inverse Fourier transform of the spectrum. The current spectrum and the numerically calculated inverse Fourier transform are presented for different frequencies within the frequency spectrum 0-5 THz in Fig. 2.9.

In the plots of the current spectra we can see the $sinc$ pattern that is expected from Eq. 2.2, which is denser in the interval $[-k_d, k_d]$ for larger frequencies, as k_d is proportional to the frequency. The plots are shown in this interval, because this range is of interest for the far field radiation. We remind that for the far field calculation k_x is equal to $k_d\, sin\theta\, cos\phi$, where θ and ϕ are the coordinates of the observation point, thus the $k_x \in [-k_d, k_d]$. In the plots we also observe peaks at $k_x = k_d$ at all plots, which is due to the branch cut and the radiation of the antenna. Finally, we observe the peaks at $k_x \approx 0.3k_d$ or $k_x \approx 0.4k_d$, depending on the frequency, which is due to a leaky pole, as explained before.

The plots on the right side of Fig. 2.9 show the equivalent currents in the spatial domain for the respective frequencies shown in the left side. The plots have been derived by numerically calculating the inverse Fourier transform of the current spectra, which yielded noisy results. Therefore, we have used a smoothing function during the post-processing stage, which performs a moving average filter on the data. The results are quite

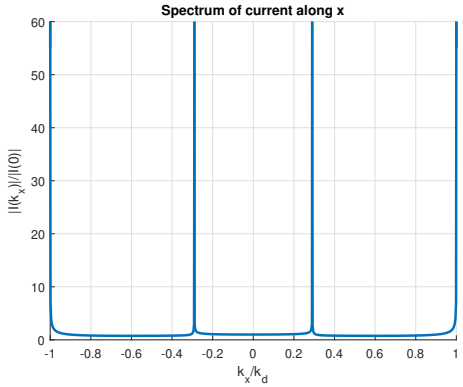

(a) 100 GHz

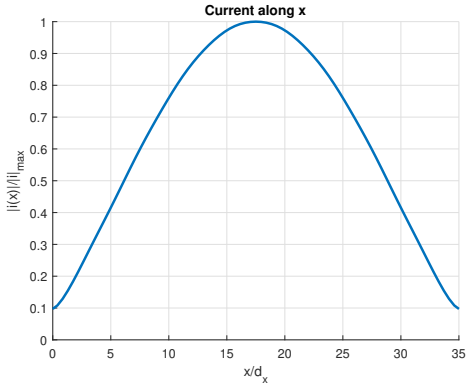

(b) 100 GHz

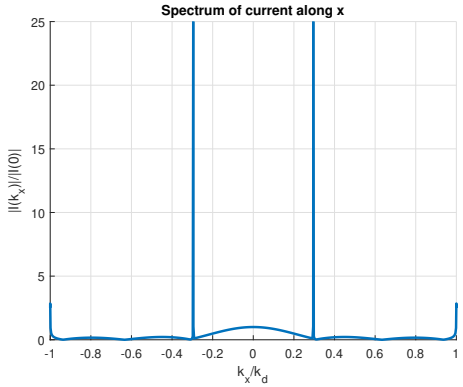

(c) 500 GHz

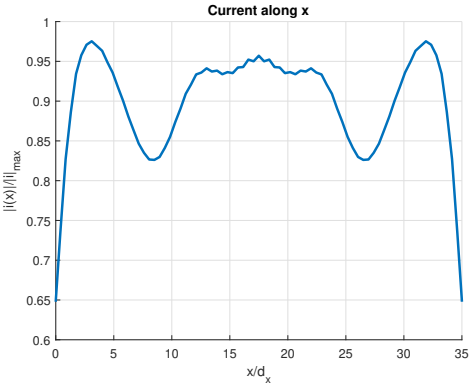

(d) 500 GHz

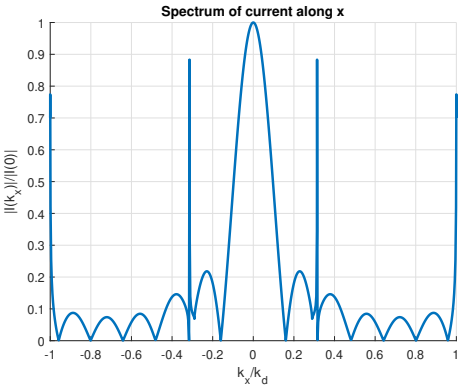

(e) 1 THz

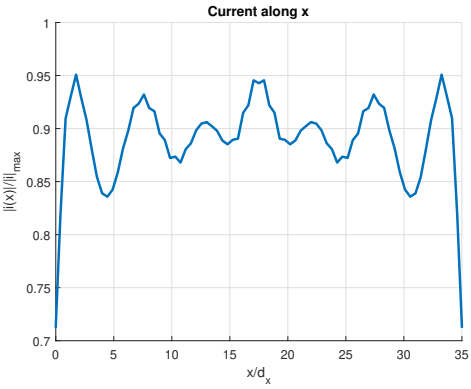

(f) 1 THz

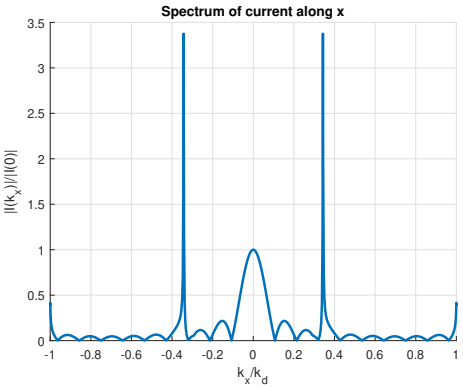

(g) 1.5 THz

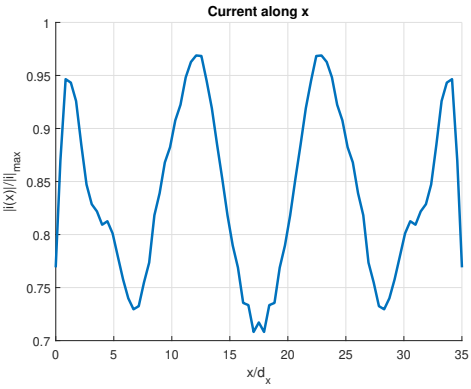

(h) 1.5 THz

Figure 2.9: Dipole current along x for various frequencies

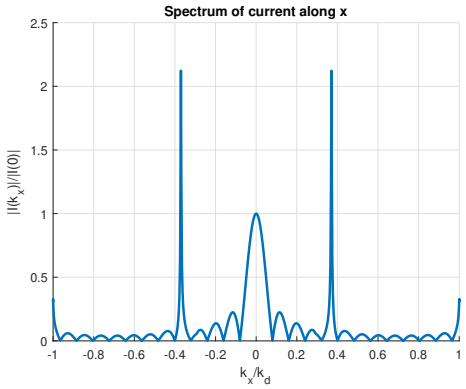

(i) 2 THz

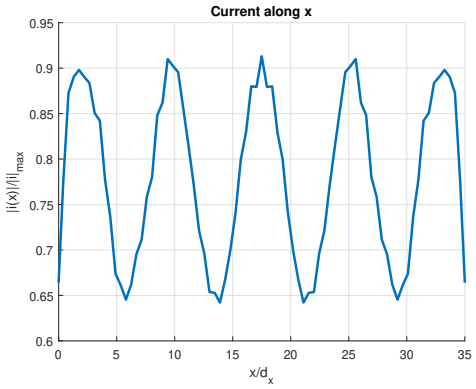

(j) 2 THz

Figure 2.9: Dipole current along x for various frequencies (cont.)

consistent with the expectations. For low frequencies (100 GHz), the electrical size of the array is small and the current has a sinusoidal form, like the current of a half-wave dipole. For higher frequencies the current shows an oscillating behaviour but does not vary significantly. This behaviour is characteristic of the broadband radiation exhibited by the connected dipole array.

2.1.4. Field patterns from PCCA

Once we have computed the current spectrum, we can use Eq. 2.1 to compute the far field radiated by the connected dipole array. The spectral Green's function that appears in the expression is calculated as shown in Appendix B. The far field patterns at the two main cuts $\phi = 0°$ (E-plane) and $\phi = 90°$ (H-plane) are given in Fig. 2.10 for various frequencies. The first subfigures that correspond to low frequencies present a the acquired results that were obtained theoretically in comparison with CST results. For higher frequencies CST results were not feasible to obtain due to memory limitations.

From the comparison between CST and Matlab we observe that in CST the leaky wave pole that is close to 20° and affects the electric field pattern is not detected, but the width and amplitude of the lobes in the pattern are in agreement with the theoretical results. Specifically, for the E-plane ($\phi = 0°$ cut) the results from Matlab and CST match almost perfectly, whereas for the H-plane ($\phi = 90°$ cut) the side lobe levels are a bit different. As the connected dipole array will be used as feed in a lens, we are mostly interested in angles that are close to broadside, because at these angles the transmission of the electromagnetic wave will be higher than at large elevation angles. Therefore, it is important for the validation of the radiated field by the connected dipole array that there is agreement between the theoretical and CST results for small angles.

It is obvious from Fig. 2.10 that as the frequency increases, the main lobe becomes narrower and the number of side lobes increases. The side lobe level is for all frequencies at least 10 dB lower than the main lobe, with the exception of the peak that arises at approximately 20° due to a leaky wave pole. For larger frequencies we expect a similar trend, which is narrower main and side lobes, as well as more lobes. The effect of narrower lobes is explained by the fact that as the frequency increases, the wavelength decreases and the electrical size of the array increases, making the radiation more directive.

The directivity D of the PCCA is given in Fig. 2.11, which has been computed, for broadside radiation, as

$$D = D(\theta = 0, \phi = 0) = 4\pi \frac{U(0,0)}{P_{rad}} = 4\pi \frac{U(0,0)}{\int_0^{2\pi} \int_0^{\pi} U(\theta,\phi) sin\theta \, d\theta \, d\phi} = 4\pi \frac{\frac{1}{2\zeta}|E(0,0)|^2}{\int_0^{2\pi} \int_0^{\pi} \frac{1}{2\zeta}|E(\theta,\phi)|^2 sin\theta \, d\theta \, d\phi}$$

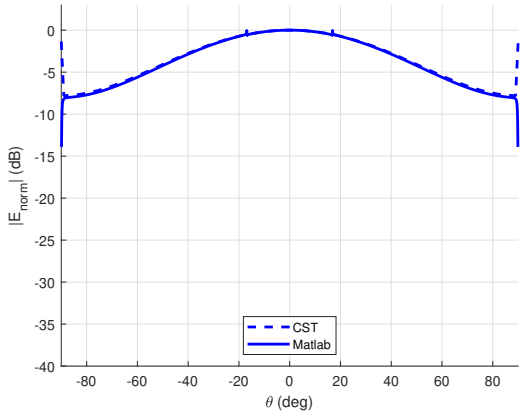

(a) f = 100 GHz, $\phi = 0°$ cut

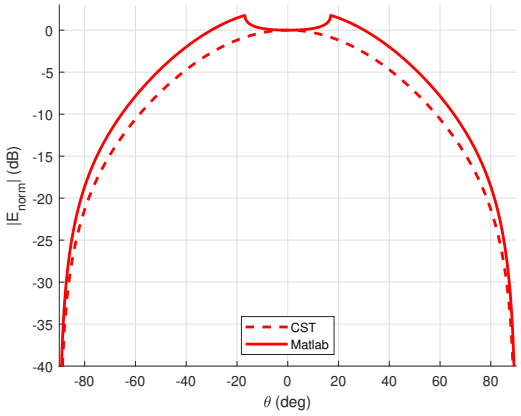

(b) f = 100 GHz, $\phi = 90°$ cut

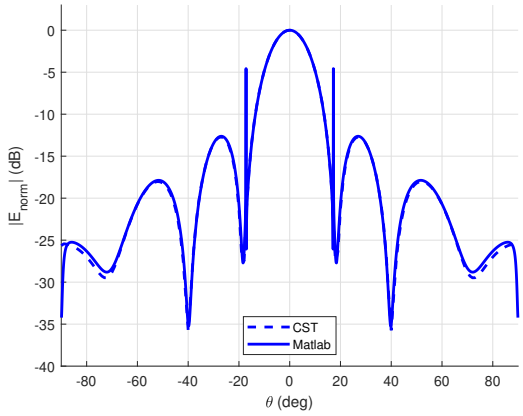

(c) f = 500 GHz, $\phi = 0°$ cut

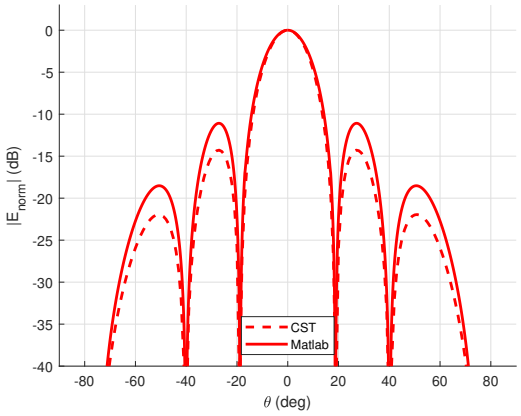

(d) f = 500 GHz, $\phi = 90°$ cut

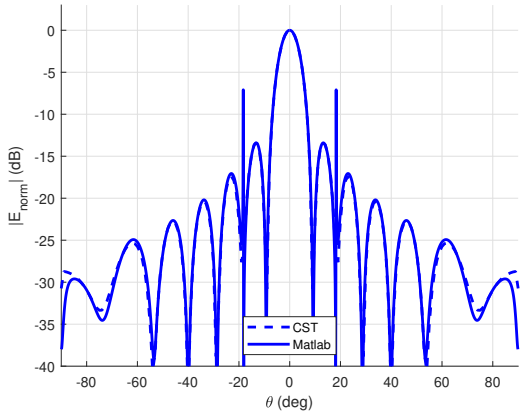

(e) f = 1000 GHz, $\phi = 0°$ cut

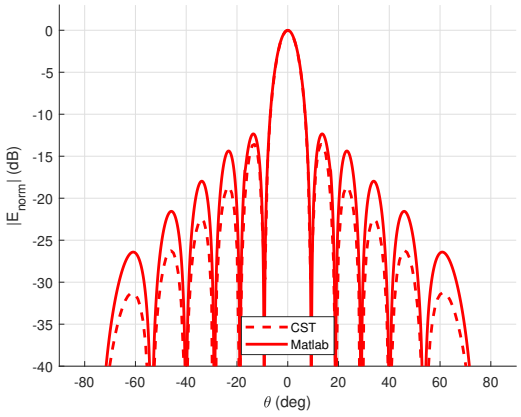

(f) f = 1000 GHz, $\phi = 90°$ cut

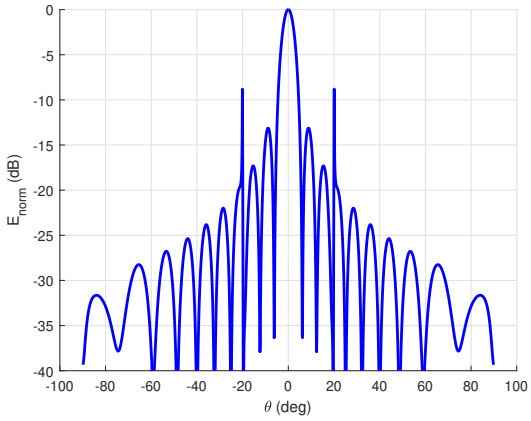

(g) f = 1500 GHz, $\phi = 0°$ cut

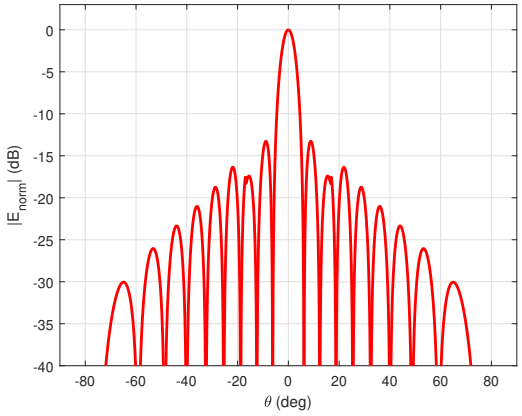

(h) f = 1500 GHz, $\phi = 90°$ cut

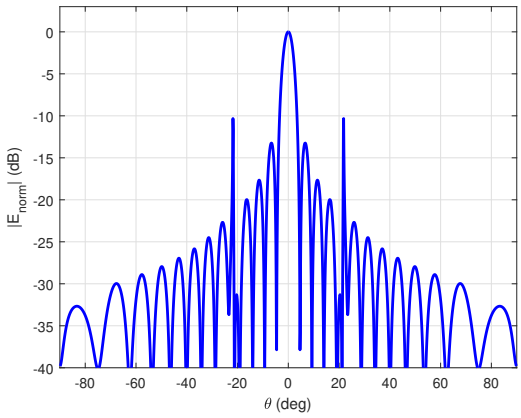

(i) f = 2000 GHz, $\phi = 0°$ cut

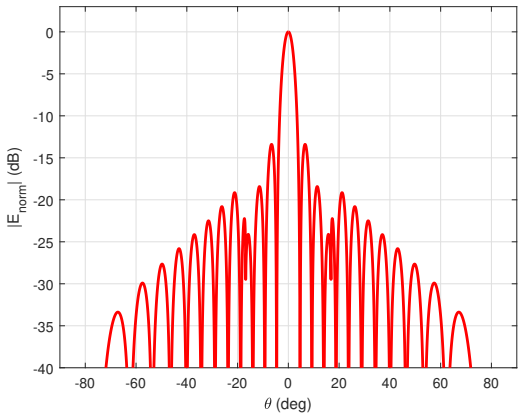

(j) f = 2000 GHz, $\phi = 90°$ cut

Figure 2.10: Plots of amplitude of electric field at the planes $\phi = 0°$ and $\phi = ang90$ at various frequencies.

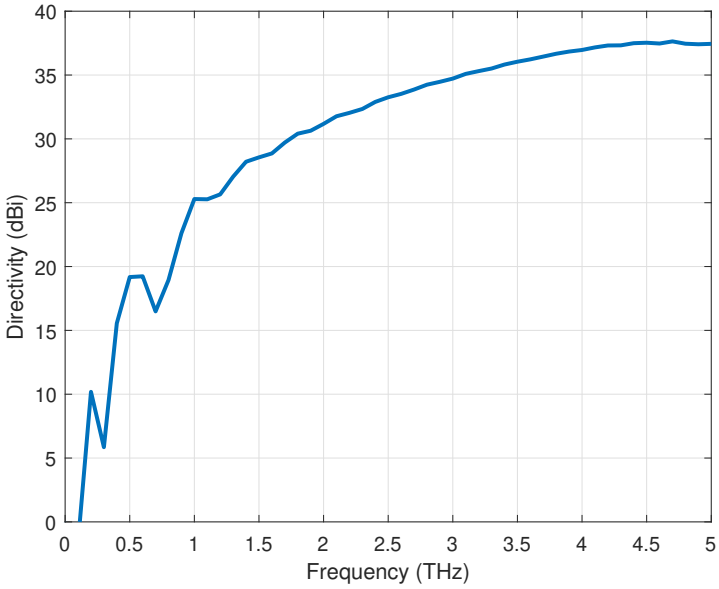

Figure 2.11: Directivity of the PCCA

2.1.5. Losses and efficiency

The lens efficiency accounts for the losses due to the backward propagation, which is power that is radiated backwards and does not reach the detector, the dielectric losses of the silicon and the reflection losses that occur in the boundary between the silicon lens and the air.

The front-to-back efficiency is the ratio between the power that is radiated forward inside the dielectric lens over the total radiated power, that includes also the power radiated backwards to the air, if we look at Fig. 1.4a.

$$\begin{aligned}
\eta_{front\,to\,back} &= \frac{P^f_{rad}}{P^{total}_{rad}} \\
&= \frac{P^f_{rad}}{P^f_{rad} + P^b_{rad}} \\
&= \frac{\int_0^{2\pi}\int_0^{\frac{\pi}{2}} U(\theta,\phi) sin\theta\, d\theta\, d\phi}{\int_0^{2\pi}\int_0^{\frac{\pi}{2}} U(\theta,\phi) sin\theta\, d\theta\, d\phi + \int_0^{2\pi}\int_{\frac{\pi}{2}}^{\pi} U(\theta,\phi) sin\theta\, d\theta\, d\phi} \\
&= \frac{\int_0^{2\pi}\int_0^{\frac{\pi}{2}} \frac{1}{2\zeta_{Si}} |E(\theta,\phi)|^2 sin\theta\, d\theta\, d\phi}{\int_0^{2\pi}\int_0^{\frac{\pi}{2}} \frac{1}{2\zeta_{Si}} |E(\theta,\phi)|^2 sin\theta\, d\theta\, d\phi + \int_0^{2\pi}\int_{\frac{\pi}{2}}^{\pi} \frac{1}{2\zeta_{air}} |E(\theta,\phi)|^2 sin\theta\, d\theta\, d\phi} \\
&= \frac{\frac{1}{2\zeta_{Si}}\int_0^{2\pi}\int_0^{\frac{\pi}{2}} |E(\theta,\phi)|^2 sin\theta\, d\theta\, d\phi}{\frac{1}{2\zeta_{Si}}\int_0^{2\pi}\int_0^{\frac{\pi}{2}} |E(\theta,\phi)|^2 sin\theta\, d\theta\, d\phi + \frac{1}{2\zeta_{air}}\int_0^{2\pi}\int_{\frac{\pi}{2}}^{\pi} |E(\theta,\phi)|^2 sin\theta\, d\theta\, d\phi} \\
&= \frac{\frac{\sqrt{\epsilon_{r,Si}}}{2\zeta_{air}}\int_0^{2\pi}\int_0^{\frac{\pi}{2}} |E(\theta,\phi)|^2 sin\theta\, d\theta\, d\phi}{\frac{\sqrt{\epsilon_{r,Si}}}{2\zeta_{air}}\int_0^{2\pi}\int_0^{\frac{\pi}{2}} |E(\theta,\phi)|^2 sin\theta\, d\theta\, d\phi + \frac{1}{2\zeta_{air}}\int_0^{2\pi}\int_{\frac{\pi}{2}}^{\pi} |E(\theta,\phi)|^2 sin\theta\, d\theta\, d\phi} \\
&= \frac{\sqrt{\epsilon_{r,Si}}\int_0^{2\pi}\int_0^{\frac{\pi}{2}} |E(\theta,\phi)|^2 sin\theta\, d\theta\, d\phi}{\sqrt{\epsilon_{r,Si}}\int_0^{2\%pi}\int_0^{\frac{\pi}{2}} |E(\theta,\phi)|^2 sin\theta\, d\theta\, d\phi + \int_0^{2\pi}\int_{\frac{\pi}{2}}^{\pi} |E(\theta,\phi)|^2 sin\theta\, d\theta\, d\phi}
\end{aligned}$$

If we assume that the integral of the square of the electric field amplitude is almost equal for transmission in silicon and in the air, the efficiency becomes approximately equal to

$$\eta_{front\,to\,back} \approx \frac{\sqrt{\epsilon_{r,Si}}}{\sqrt{\epsilon_{r,Si}}+1} = \frac{\sqrt{11.9}}{\sqrt{11.9}+1} = 0.775$$

Fig. 2.12a gives the front-to-back efficiency with respect to frequency. We observe that for a wide frequency range (2.5 THz - 4.5 THz), the efficiency is generally close to the expected value of 0.775. For low frequencies, the size of the array is probably very small compared to the wavelength and the radiation patterns cannot be predicted intuitively.

The reflection efficiency is related to the reflection of the electromagnetic wave at the boundary between the lens and the air, due to the different characteristic impedances of the media. For this reason, a matching layer will be used, as is also proposed in [25], that minimizes the reflections at a certain frequency. The most common matching layer is a quarter wavelength layer of a material with relative permittivity $\epsilon_{r,match} = \sqrt{\epsilon_{r,Si} \cdot \epsilon_{r,air}} = \sqrt{\epsilon_{r,Si}}$. The reflection losses in the specific configuration with the hyperhemispherical lens and the quarter-wavelength matching layer are taken into consideration in the PO tool developed in the TS group that calculates secondary fields, so we will not elaborate further on it.

The dielectric loss efficiency can be computed by the loss tangent $tan\delta$ over frequency, which is known for high resistivity silicon ([34]). From [35] we know that the complex permittivity of a medium is expressed as

$$\epsilon = \epsilon_0 \epsilon_r (1 - j\, tan\delta)$$

The propagation constant is then equal to

$$k = \omega\sqrt{\mu\epsilon} = \omega\sqrt{\mu_0\epsilon_0\epsilon_r}\sqrt{1 - j\, tan\delta}$$

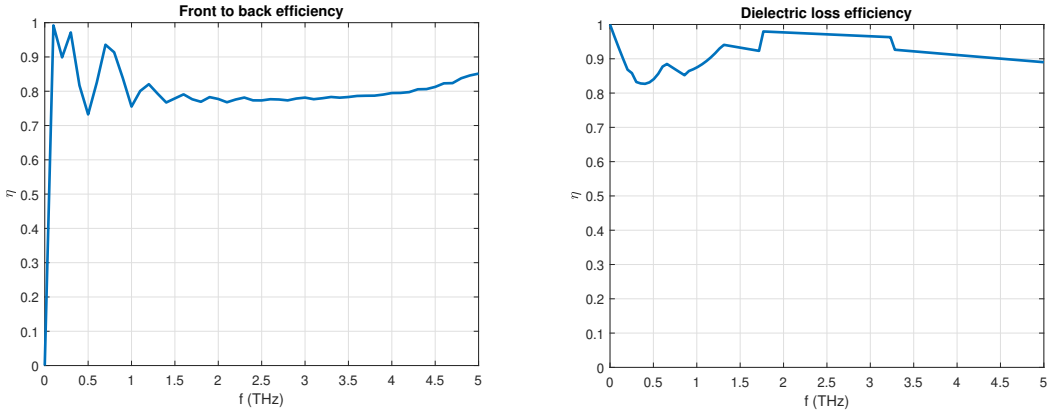

(a) $\eta_{front\,to\,back}$ (b) η_{diel}

Figure 2.12: Lens efficiency terms and total lens efficiency

In the dielectric the losses are very small, which means that $1 \gg tan\delta$, so we can write $\sqrt{1-jtan\delta} \approx 1-j\frac{tan\delta}{2}$ and $k \approx \omega\sqrt{\mu_0\epsilon_0\epsilon_r} - j\omega\sqrt{\mu_0\epsilon_0\epsilon_r}\frac{tan\delta}{2}$. The electric field of the propagating plane wave in the lens will then be equal to

$$E = E_0 e^{-jkz} = E_0 e^{-j\omega\sqrt{\mu_0\epsilon_0\epsilon_r}z} e^{-\omega\sqrt{\mu_0\epsilon_0\epsilon_r}\frac{tan\delta}{2}z}$$

and the power which is proportional to the square of the electric field will have an amplitude that decreases with a factor

$$P = P_0 e^{-\omega\sqrt{\mu_0\epsilon_0\epsilon_r}tan\delta z}$$

For a very directive beam, the wave propagates inside the hyperhemispherical lens a distance equal to $L+R$, where R is the radius of the spherical part of the lens and $L = 0.29R$ is the extension length of a hyperhemispherical silicon lens. Therefore, the dielectric loss efficiency is

$$\eta_{diel} = \frac{P}{P_0} = \frac{P_0 e^{-\omega\sqrt{\mu_0\epsilon_0\epsilon_r}tan\delta(L+R)}}{P_0} = e^{-\omega\sqrt{\mu_0\epsilon_0\epsilon_r}tan\delta(L+R)}$$

and is shown as a function of the frequency in Fig. 2.12b. The total lens efficiency is the product of the three efficiency terms

$$\eta_l = \eta_{front\,to\,back} \cdot \eta_{refl} \cdot \eta_{diel}$$

2.2. Radiation of the lens antenna

After we have computed and verified the far field patterns of the connected dipole array over the whole frequency band of interest, we can use this far field and the PO Matlab tool in order to find the field outside of the lens. This section presents the results that we have found with this tool. Details about the functionality of the tool are given in Ch. 4 and in this section we focus on the specific application of the PCCA as the lens feed.

The dimension for the lens is such that it fulfills the condition that the lens boundary is in the far field region of the feed for frequencies up to 2.21 THz, given that the lens material is silicon. The parameters related to the matching layer are similar to the ones selected in [25], so that we know that they will correspond to realistic values. Specifically, the material of the matching layer is parylene and The thickness of the matching layer has been determined in such a way that it is equal to $\lambda/4$ at the frequency of 2 THz. The type of lens has been chosen to be hyperhemispherical because of the constant directivity it exhibits over a wide frequency band. Finally, the rim angle has been set at 15°, because we expect already a very directive beam from the feed for the whole frequency band of operation, so most of the energy will be close to the broadside direction. The selected geometrical properties are summarized in Table 2.2.

Parameter	Value
Type of lens	Hyperhemispherical
Relat. permittivity ϵ_r^{lens}	11.9
Relat. permittivity of match. layer ϵ_r^{match}	2.72
Thickness of match. layer	23 μm
Lens diameter	15 mm
Lens rim angle	15°

Table 2.2: Parameters of lens antenna

The geometry of the lens is shown in Fig. 2.13. For the selected value of lens diameter and rim angle the radius of the hemisphere is, as is shown in Fig. 2.13, R_{sph} = 22.69 mm and the extensions length is L = 6.58 mm, so the total distance of the lens surface from the feed is approximately 30 mm.

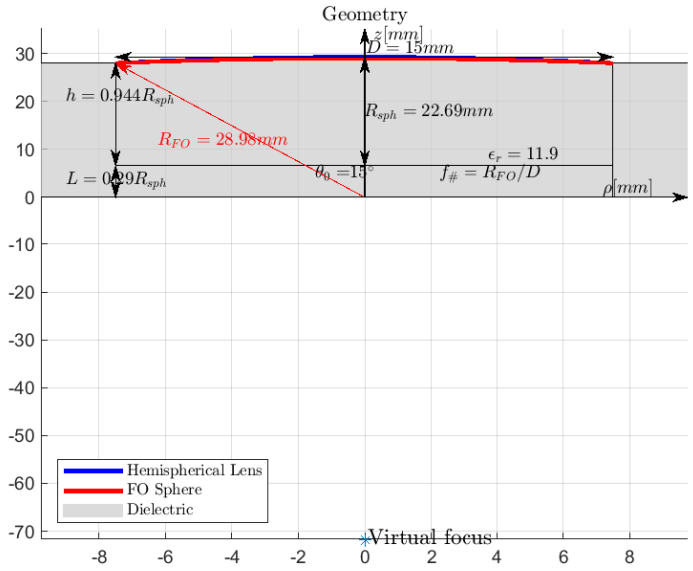

Figure 2.13: Geometry of the THz lens

2.2.1. Equivalent current on the lens boundary

Figs. 2.14 to 2.22 display the electric field pattern radiated by the feed in co-polarized and cross-polarized components, according to Ludwig's third definition [36], for various frequencies. We observe that the cross-polarized components are significantly smaller than the co-polarized for all examined frequencies. By comparing the co-polarized component of the electric field for different frequencies we also observe that the main beam becomes narrower as the frequency increases, which is in agreement with the results shown in Fig. 2.10. Moreover, due to the selection of a small rim angle for the lens, the peaks in the pattern due to the leaky pole are absent, which is positive, because it would create an undesired effect on the secondary field. The magnetic field is proportional to the electric field in the Fraunhofer region and is given by the expression $\vec{H} = \frac{1}{\zeta_d}\hat{r} \times \vec{E}$, so it has the same pattern as the electric field.

Figs. 2.14 to 2.22 also show the amplitude and phase of the equivalent electric currents computed on the lens surface, which radiate to the free space and create the secondary field. With respect to the amplitude, we observe that the equivalent current has the same pattern as the co-polarized component of the field radiated by the feed, which makes perfect sense, considering Eqs. 4.1 and 4.2, which derive the equivalent electric and magnetic current directly from the far field of the feed, after transmission through the lens surface. Regarding the phase, we can notice that the phase is relatively constant close to the broadside direction and there are equiphase (almost) concentric circles on the lens surface. The variation of the phase depends on the frequency with higher frequencies yielding a larger variation of the phase.

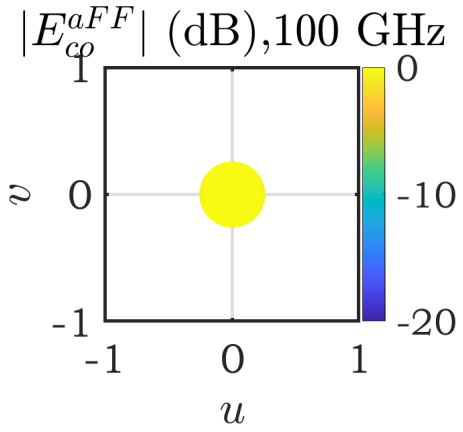

(a) Co-polarized component of electric field radiated by the feed

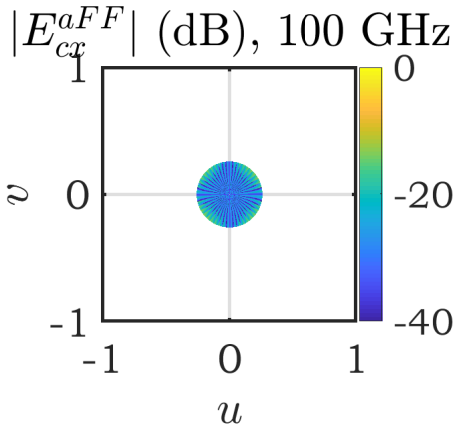

(b) Cross-polarized component of electric field radiated by the feed

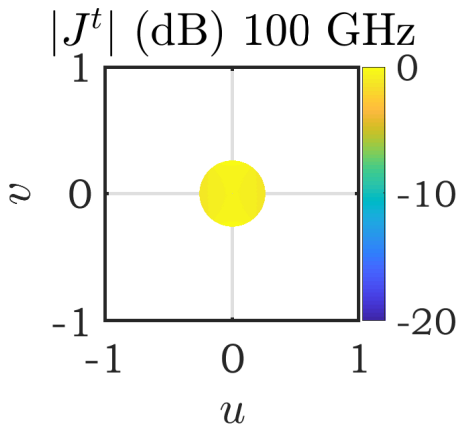

(c) Amplitude of equivalent current on lens surface

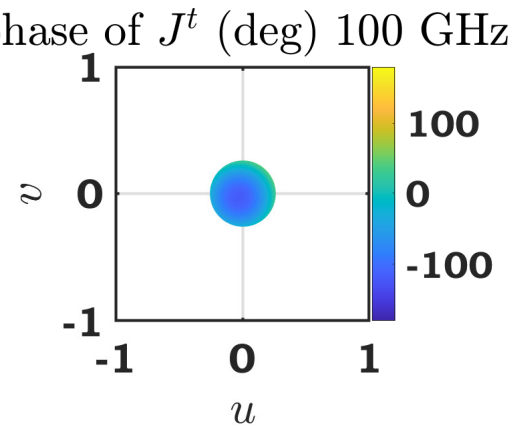

(d) Phase of equivalent current on lens surface

Figure 2.14: 100 GHz

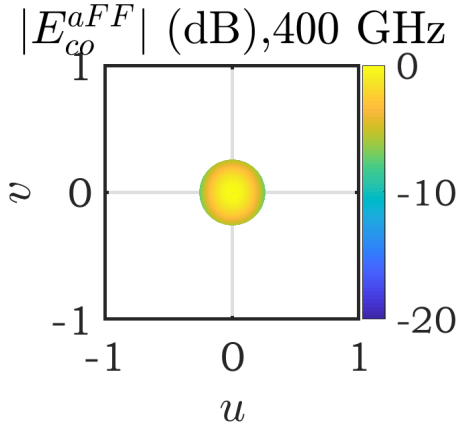

(a) Co-polarized component of electric field radiated by the feed

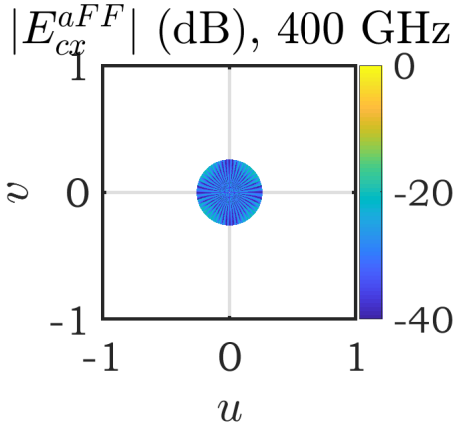

(b) Cross-polarized component of electric field radiated by the feed

Figure 2.15: 400 GHz

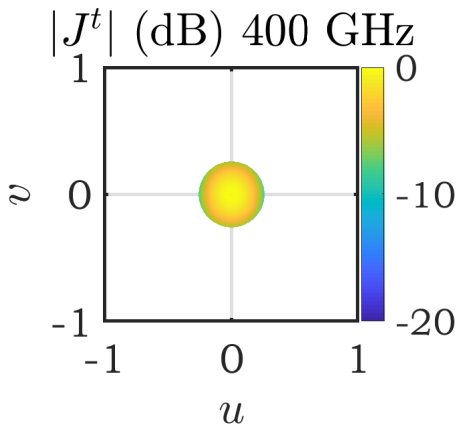

(c) Amplitude of equivalent current on lens surface

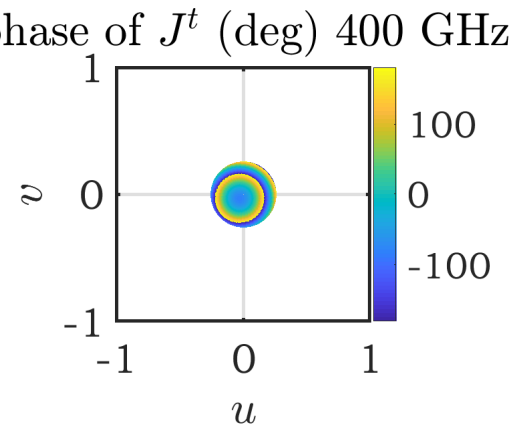

(d) Phase of equivalent current on lens surface

Figure 2.15: 400 GHz

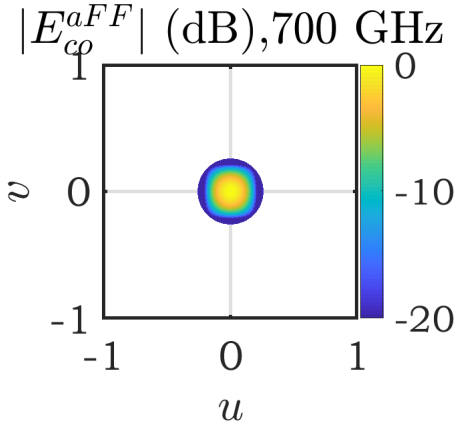

(a) Co-polarized component of electric field radiated by the feed

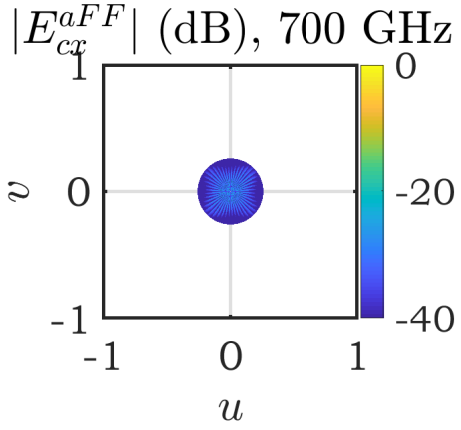

(b) Cross-polarized component of electric field radiated by the feed

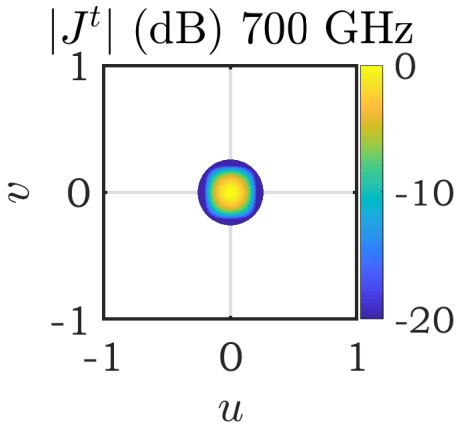

(c) Amplitude of equivalent current on lens surface

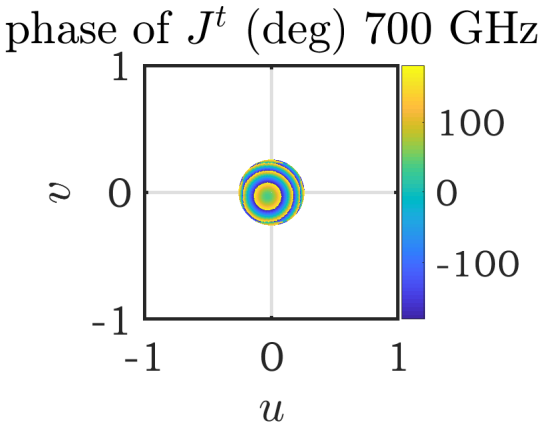

(d) Phase of equivalent current on lens surface

Figure 2.16: 700 GHz

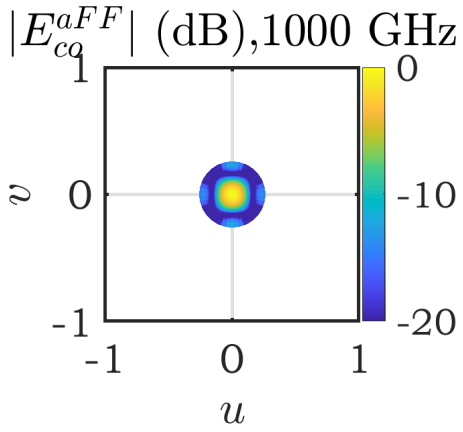

(a) Co-polarized component of electric field radiated by the feed

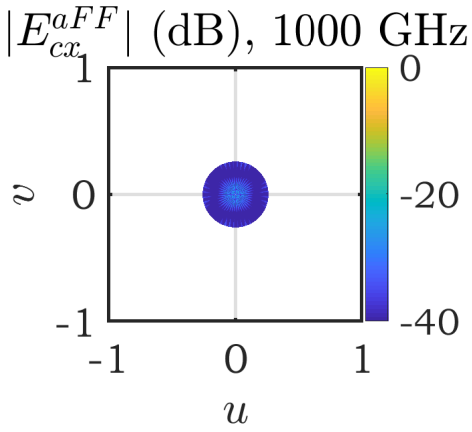

(b) Cross-polarized component of electric field radiated by the feed

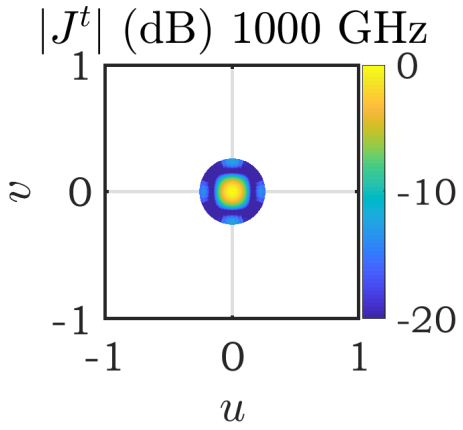

(c) Amplitude of equivalent current on lens surface

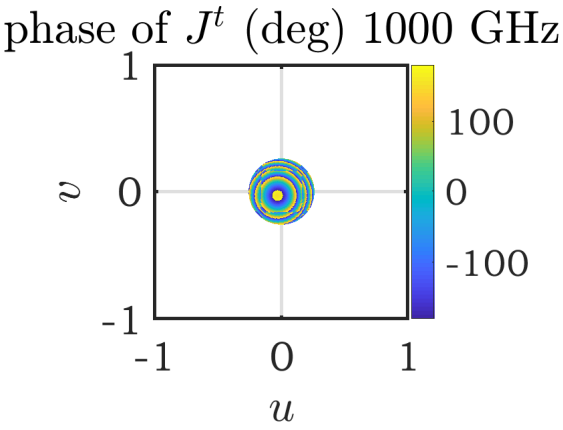

(d) Phase of equivalent current on lens surface

Figure 2.17: 1 THz

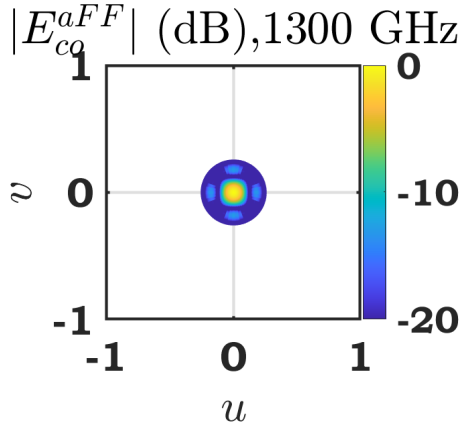

(a) Co-polarized component of electric field radiated by the feed

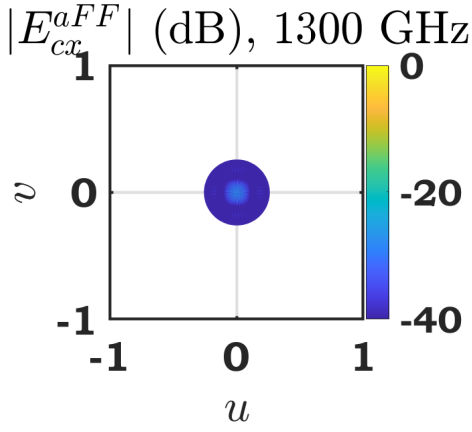

(b) Cross-polarized component of electric field radiated by the feed

Figure 2.18: 1.3 THz

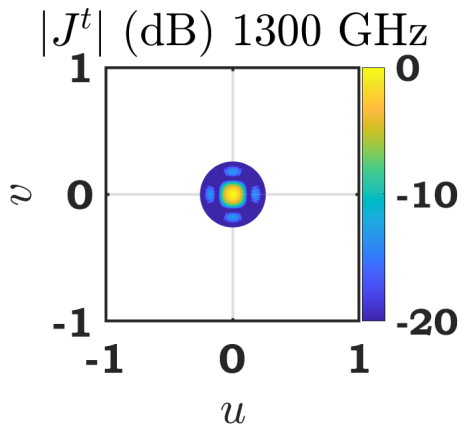

(c) Amplitude of equivalent current on lens surface

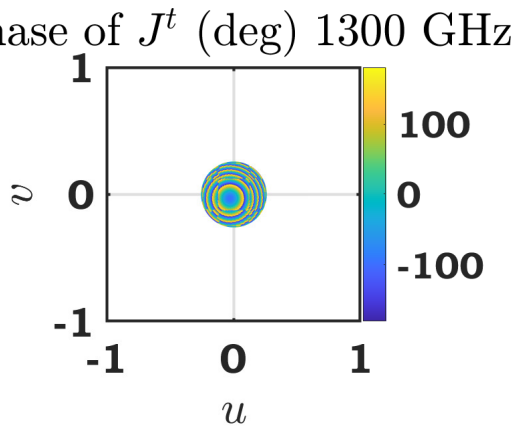

(d) Phase of equivalent current on lens surface

Figure 2.18: 1.3 THz

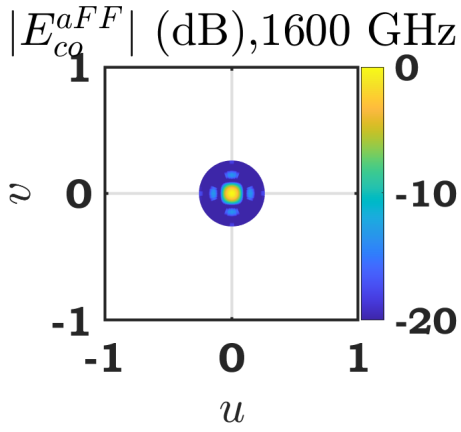

(a) Co-polarized component of electric field radiated by the feed

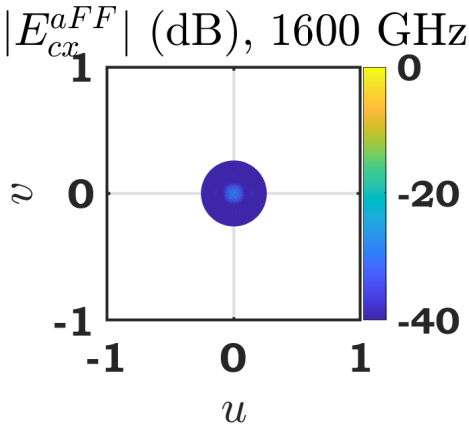

(b) Cross-polarized component of electric field radiated by the feed

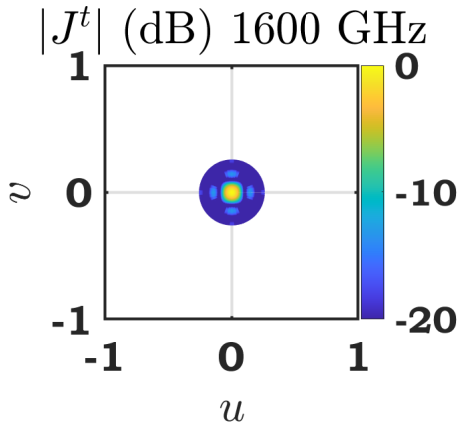

(c) Amplitude of equivalent current on lens surface

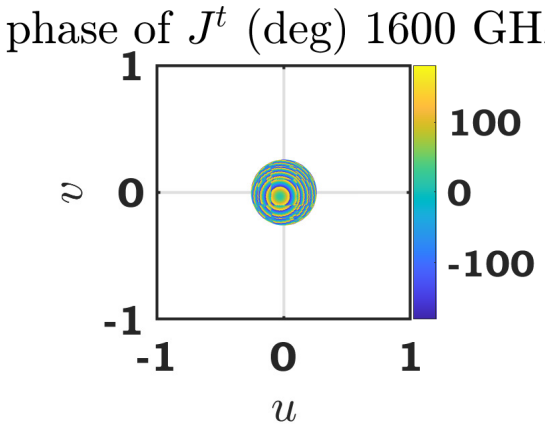

(d) Phase of equivalent current on lens surface

Figure 2.19: 1.6 THz

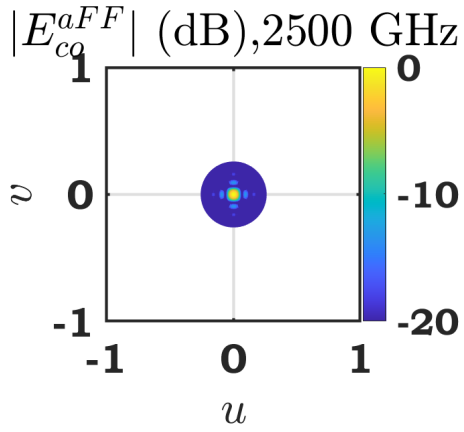

(a) Co-polarized component of electric field radiated by the feed

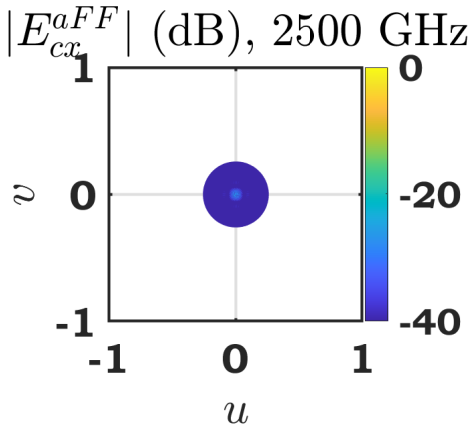

(b) Cross-polarized component of electric field radiated by the feed

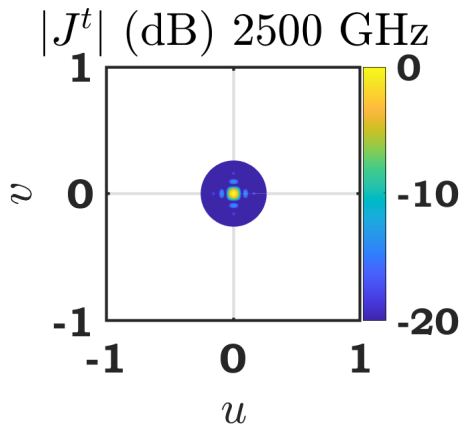

(c) Amplitude of equivalent current on lens surface

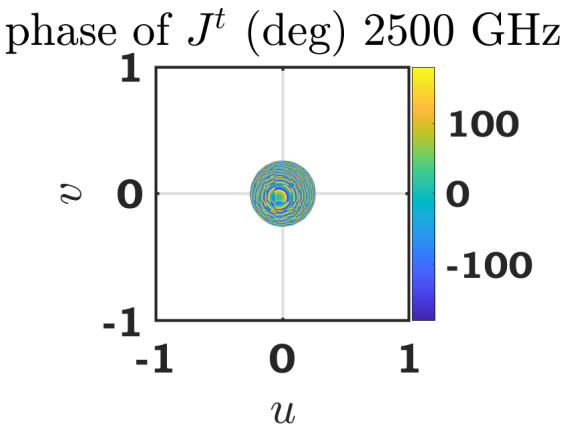

(d) Phase of equivalent current on lens surface

Figure 2.20: 2.5 THz

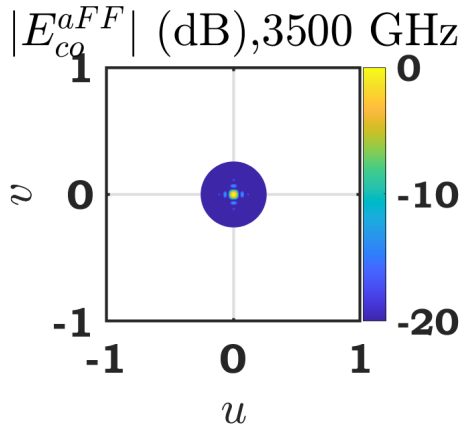

(a) Co-polarized component of electric field radiated by the feed

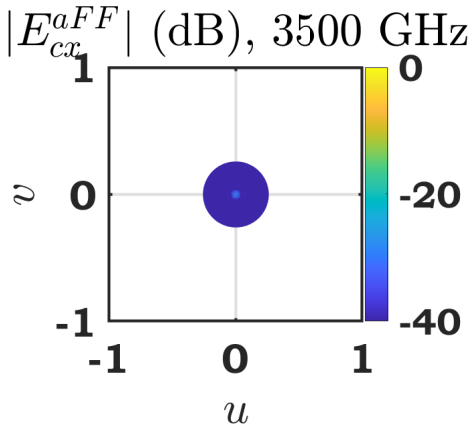

(b) Cross-polarized component of electric field radiated by the feed

Figure 2.21: 3.5 THz

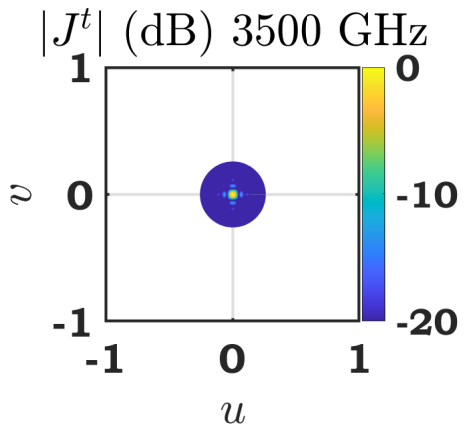

(c) Amplitude of equivalent current on lens surface

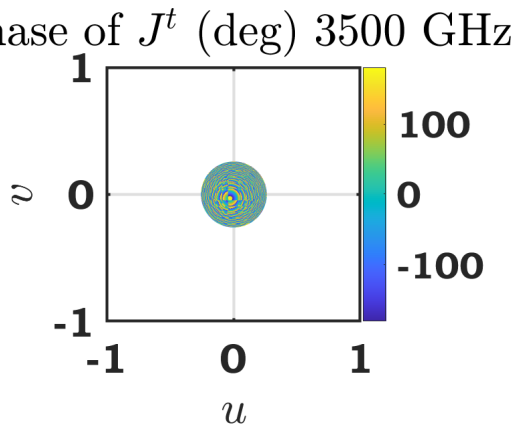

(d) Phase of equivalent current on lens surface

Figure 2.21: 3.5 THz

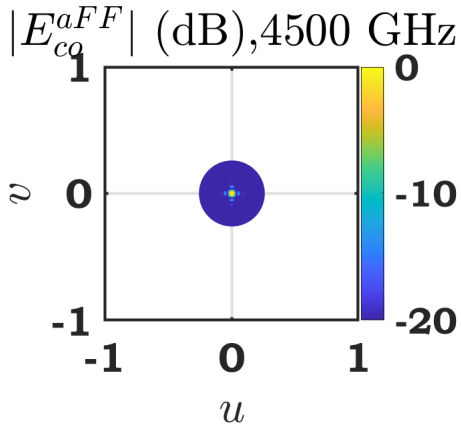

(a) Co-polarized component of electric field radiated by the feed

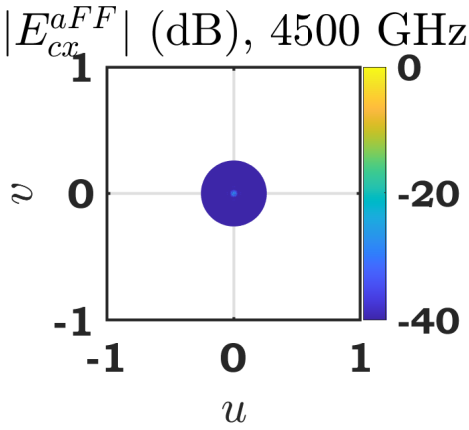

(b) Cross-polarized component of electric field radiated by the feed

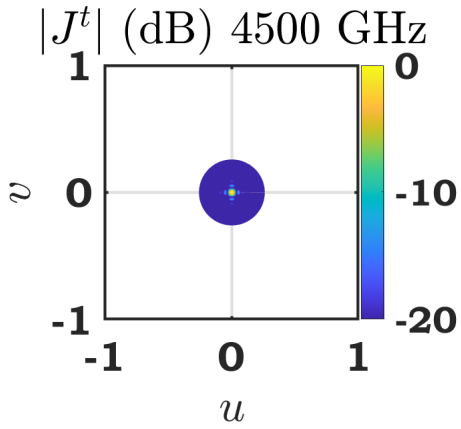

(c) Amplitude of equivalent current on lens surface

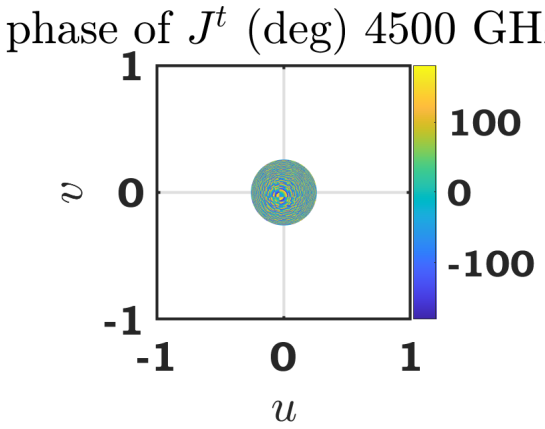

(d) Phase of equivalent current on lens surface

Figure 2.22: 4.5 THz

2.2.2. Field patterns from hyperhemispherical lens

The equivalent currents presented in the previous sections radiate in the free space beyond the lens and give the secondary fields. The total signal radiated by the lens antenna will be broadband with spectral components ranging theoretically up to 5 THz. A convergent lens within the QO path should capture this signal and redirect it to the detector. Thus, the secondary fields should have a relatively narrow main beam for all their spectral components, so that most of the energy per frequency can be captured by the lens.

Fig. 2.23 depicts the far field amplitude in the two main planes $\phi = 0°$ (E-plane) and $\phi = 90°$ (H-plane), as well as 2D sketches for elevation angles up to 35°, for various frequencies. We observe that the main beam of radiation becomes narrower as the frequency increases. Even for the lowest examined frequency of 100 GHz (Fig. 2.23a and 2.23b) the -10 dB beamwidth is 8.5°. This implies that indeed a convergent lens of reasonable dimensions can be used to capture most of the signal and send it to the detector. Furthermore, the phase of the electric fields for the different frequencies is smooth close to broadside, so we can approximate the outgoing waves with spherical waves.

Note that in Fig. 2.23 we display the far fields for frequencies up to 1.6 THz, because for higher frequencies the beam is very directive and the Matlab tool cannot give accurate results for the far field; nevertheless, we expect an even narrower beam for higher frequencies.

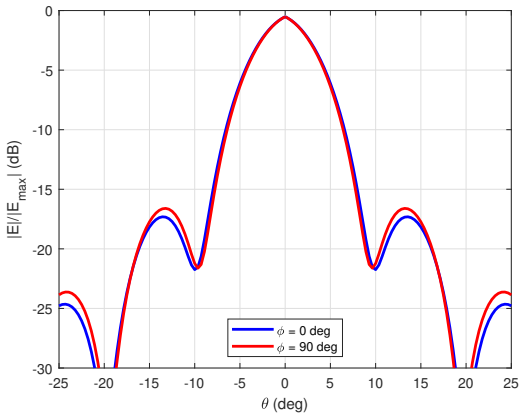

(a) 100 GHz, main plane cuts

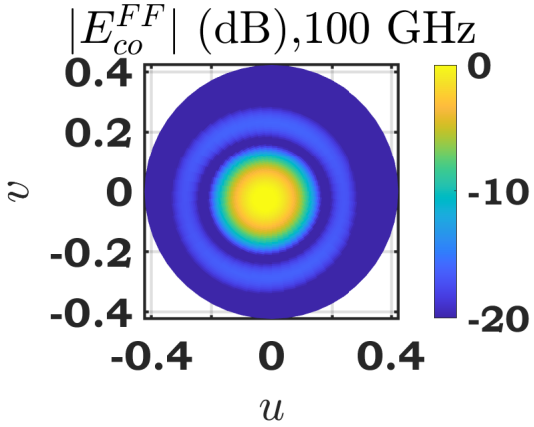

(b) 100 GHz, 2D representation

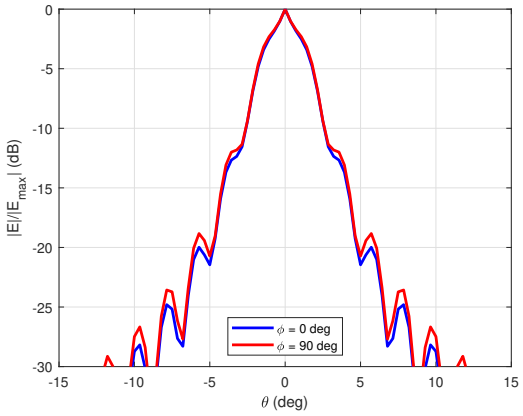

(c) 400 GHz, main plane cuts

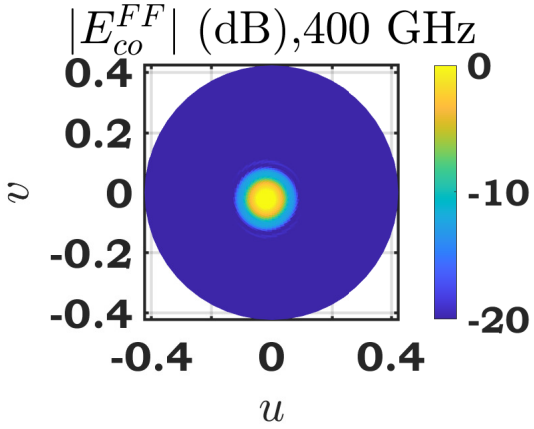

(d) 400 GHz, 2D representation

Figure 2.23: Radiation of the different spectral components from the lens antenna

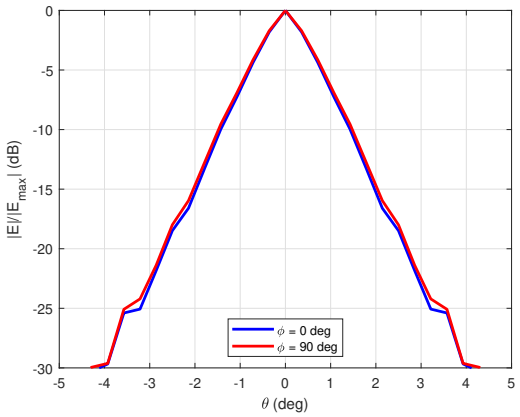

(e) 700 GHz, main plane cuts

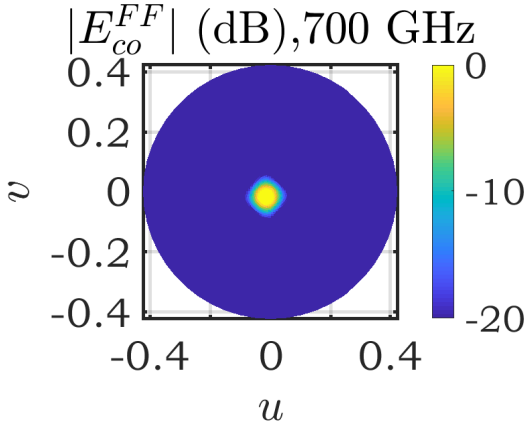

(f) 700 GHz, 2D representation

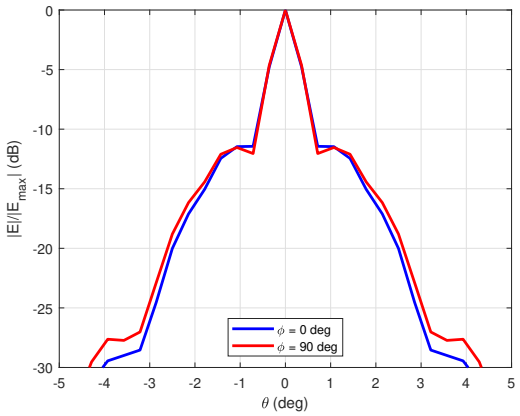

(g) 1 THz, main plane cuts

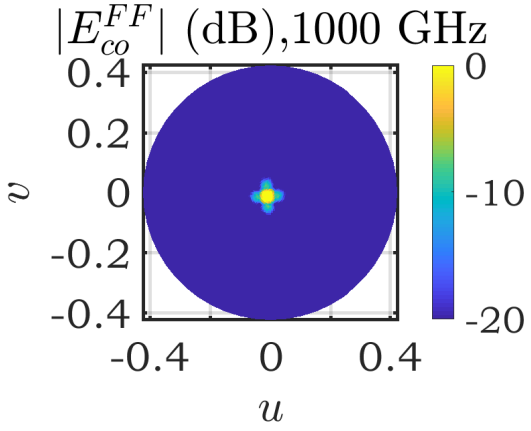

(h) 1 THz, 2D representation

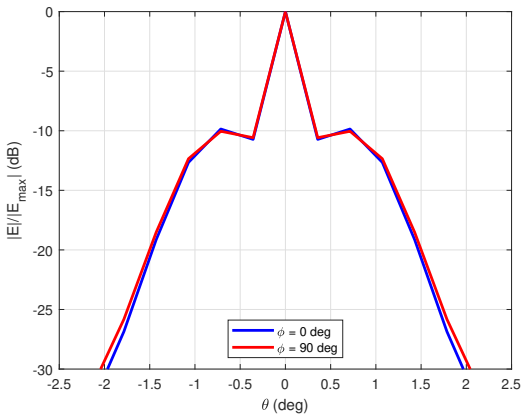

(i) 1.3 THz, main plane cuts

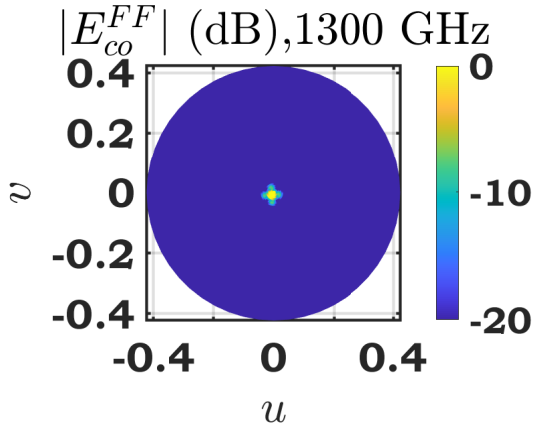

(j) 1.3 THz, 2D representation

Figure 2.23: Radiation of the different spectral components from the lens antenna

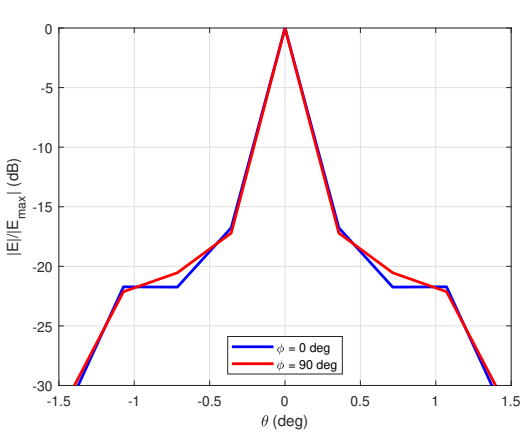

(k) 1.6 THz, main plane cuts

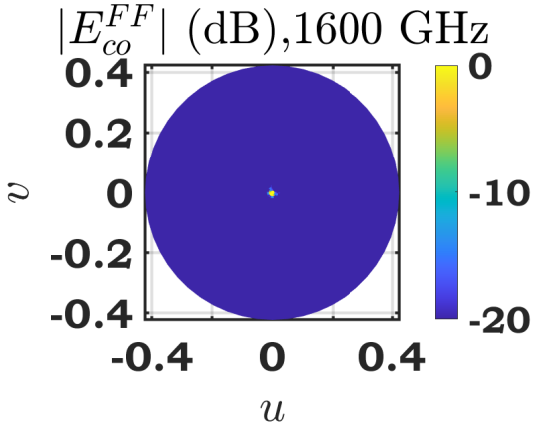

(l) 1.6 THz, 2D representation

Figure 2.23: Radiation of the different spectral components from the lens antenna

2.2.3. Efficiency and gain

Fig. 2.24 shows the radiation efficiency as a function of the frequency, which is defined in Eq. 4.3.We observe that close to 2 THz, which is the frequency for which the matching layer is equal to $\lambda/4$, the radiation efficiency reaches the maximum value, as less power is reflected at the lens-air boundary and thus more power is transmitted.

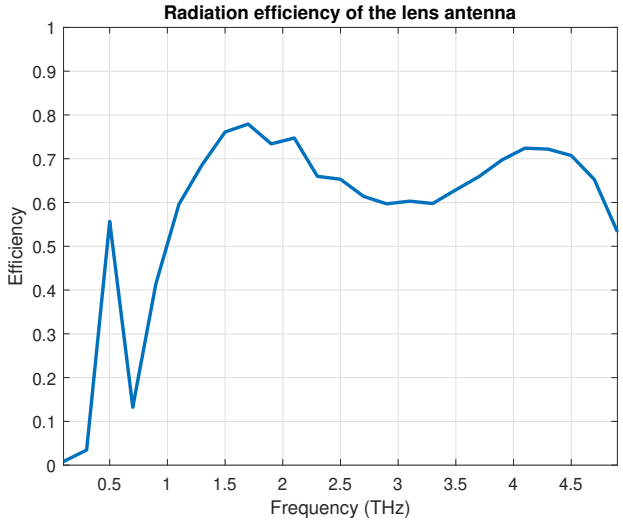

Figure 2.24: Radiation efficiency of the lens antenna

The gain of the lens antenna in the different frequencies is also computed by the GUI and is given in Fig. 2.25.

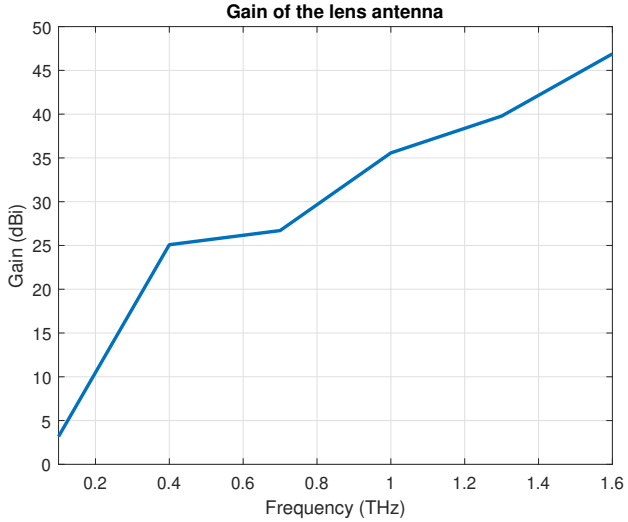

Figure 2.25: Gain of the hyperhemispherical lens antenna

3

Fabrication Process

For the fabrication of the PCCA, we need to first fabricate its individual components and then assemble them into an integrated structure. The prototype will be measured at the THz-TDS setup of the TS group which is equipped with the Tera K15 THz spectrometer of Menlo Systems [37].

3.1. Microlens array

The microlens array will be fabricated with the Nanoscribe 3D printer [38] that is located in the facilities of TU Delft [39]. Nanoscribe uses Two Photon Polymerization (2PP) to build its structures and therefore the materials that are available for use are optimized for 2PP [38]. 2PP is a procedure during which molecules in a material absorb two or more photons, when they are illuminated by a laser pulse of high intensity. The photoexcitation leads to the activation of various chemical reactions, one of which is the polymerization. An important feature of two-photon absorption is that even photons with half of the energy that is normally required for the material to be excited can create excited states [40]. Also the cross section of the two-photon absorption is very small, which is usually a negative aspect of 2PP, but in the case of nanofabrication it can create a fine resolution of the printed structures [40], [41], [42].

For the purposes of 3D printing with Nanoscribe, the microlens array was designed in SolidWorks [43], which is a CAD software that enables users to accurately design structures of any size and complexity. The design of the microlens array in SolidWorks is given in Fig. 3.1. The figure depicts the whole structure of the microlens array, which consists of 36×36 cells, each of which focuses the laser power on the excitation gap of a dipole in the connected dipole array.

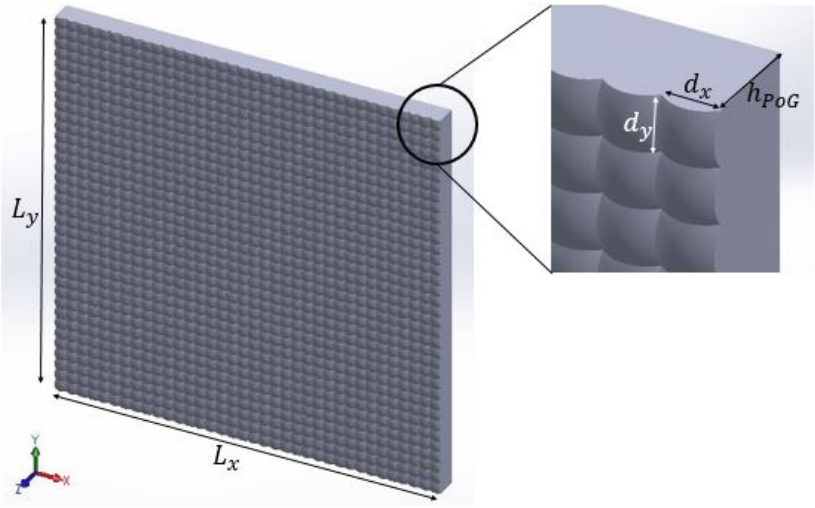

Figure 3.1: The microlens array designed in SolidWorks

3.1.1. Maximum allowed laser power

As mentioned before, the 2PP method implemented in Nanoscribe requires a laser source whose photons are absorbed by the molecules of a resin, resulting in their polymerization. The laser frequency of the source is set at 385 THz (780 nm wavelength), which is the same frequency as the one used for the excitation and operation of the PCCA. This fact creates a concern of whether the laser source during the operation of the PCCA causes any chemical reactions and deformation of the resin. This means, basically, that we need to set a threshold of the maximum allowable peak power level of the laser, above which the resin will burn or undergo a deformation.

A solution that could prevent the resin from being exposed at high power levels in any case, is the growth of an oxide at the metal/semiconductor-resin interface, as shown in Fig. 3.2. The role of the oxide is twofold. Firstly, it prevents reflection of the laser at the metal, which would cause an increase of the laser power at the resin from the superposition of the incident and the reflected field. Secondly, a substantial thickness of oxide layer underneath the resin comparable to the focal depth ensures that the maximum electric field on the resin is at least 3 dB lower than the electric field at the focal plane, thus the power that will be absorbed by the resin will be considerably low even for high electric field at the focal plane.

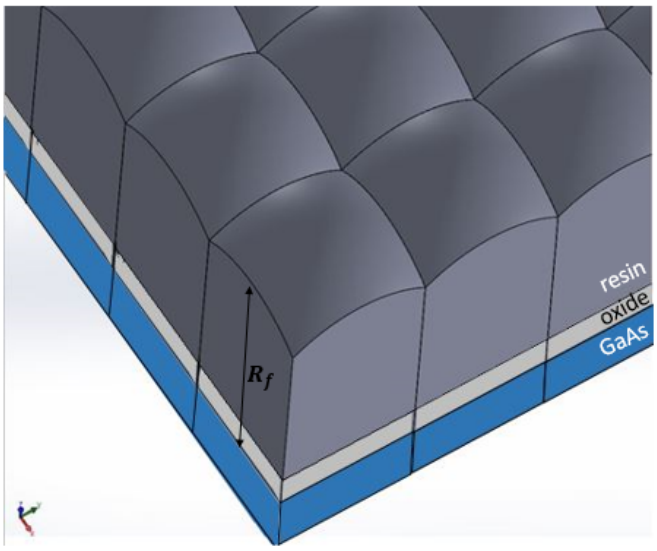

Figure 3.2: Oxide layer between resin and GaAs

In order to calculate the desired thickness of the oxide layer, we need to estimate the focal depth of the microlenses. According to [44], the intensity of the field is given by the expression

$$I(P) = I_0\big(1 - \frac{u_N}{2\pi N}\big)^2\big(\frac{sin(u_N/4)}{u_N/4}\big)^2$$

where

$$u_N = 2\pi N \frac{z}{R_f + z}$$

In the above expressions, N is the Fresnel number and is equal to $N = \frac{D^2}{4\lambda R_f}$ with D the diameter of the lens, λ the wavelength in the lens medium and R_f the focal distance; P is a point on the major axis of the ellipse, which is shifted by z from the focus of the lens.

Since the lens diameter is not constant in the square geometry that has been selected for the microlenses, we examine two extreme cases and calculate the focal depth for these two; one for the minimum lens diameter $D_{min} = 15\mu$m and one for the maximum lens diameter $D_{max} = 15\sqrt{2} = 21.21\mu$m. The selection of these lens diameters is explained in the inset of Fig. 3.3. Fig. 3.3 presents the normalized vertical pattern of the intensity (or equivalently, the electric field) in dB, with respect to the field at the focal plane. From the plot, we can conclude that the resin layer is outside of the focal depth region of the lens, if the oxide thickness is between 4.92 and 9.4 μm. Such oxide thickness cannot be deposited with common procedures on a wafer, so

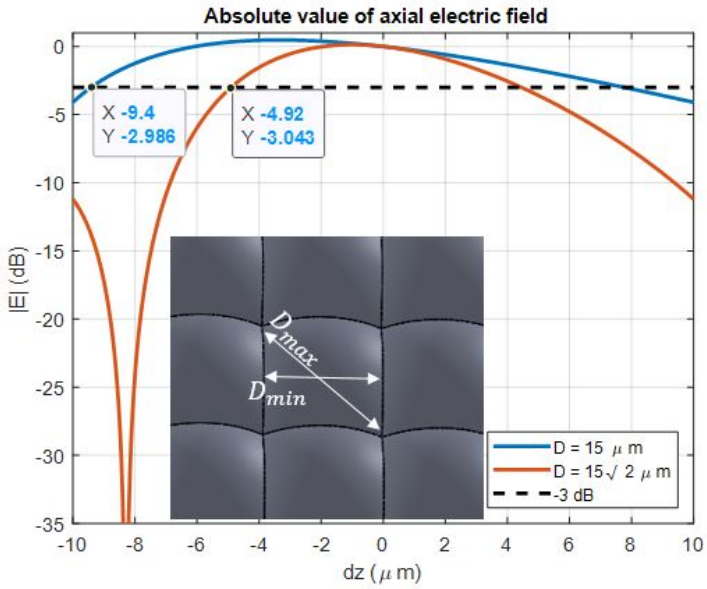

Figure 3.3: Normalized intensity of laser inside the microlens

it seems that we cannot prevent exposing the resin at approximately the same power level as that at the focal plane.

Therefore, we need to experimentally test if the estimated and planned laser power is safe for the resin, or if it causes damage to it. In the latter case, we need to determine a threshold and adjust our theoretical work based on the practical restrictions. For this test we printed a relatively big slab of IP-Dip on a chip. Our goal was to illuminate the slab with increasing laser power and observe at which power level the laser damages the resin. Of course this laser power needs to be expressed in power density, as in the final structure the laser power per unit cell will be low, but, due to the concentration of the laser around the focal point, the power density is the metrics that matter. From our experiment we did not observe any blatant damage to the resin; however, further tests need to be made, because the spin-coating of our chip did not yield a smooth surface and there were already some imperfections on the slab before the experiment, so there could have been damages that coincide with the imperfections and were not visible.

For the nominal value of the laser power that has been considered in the theoretical design $P_{laser,ave}$ = 250 mW with a 3dB diameter equal to 540 μm and the geometry of the microlens array defined in [23], the maximum power density at the focal plane is $S_{max} = 141.9\,\mu W/\mu m^2$.

3.1.2. Test of alignment and accuracy capabilities of Nanoscribe

Practical difficulties and challenges of 3D-printing of microlens arrays whose dimensions are in the order of μm are described in [42]. One of the main problems of the author with respect to the fabrication of microlens arrays is the required slicing and hatching during printing, because the 3D printer can only print a certain area at a time and subsequently it stitches the separately printed areas. Due to this limitation, he had to make sure that the stitching lines would be located at the intersections between microlenses and not on a microlens. Another problem was the discretization of the microlens array, which had to be as accurate as possible, so that the elliptical shape could be formulated. Finally, there were consistent errors in the printed geometry, which had to be compensated via tuning of the design parameters in the model.

Since similar constraints and issues would emerge in our configuration as well, we had to investigate the accuracy of the printed microlenses for our specific design. Given that the dimensions of the unit cell are only a few μm and the gap size at the dipoles is 1 μm, a horizontal misalignment of even a few hundred nm would destroy the almost uniform illumination of the gap and reduce the laser power that reaches the gap. Consequently there would be strong mismatch between the expected results and the measurements. Furthermore, the vertical accuracy is also crucial. The height of the microlenses determines whether the dipole gaps will be at the focal plane of the lenses, while the accurate shape of the ellipsoidal part ensures that all laser rays will actually focus at the focal point. An error in either of the two will result in unpredictable

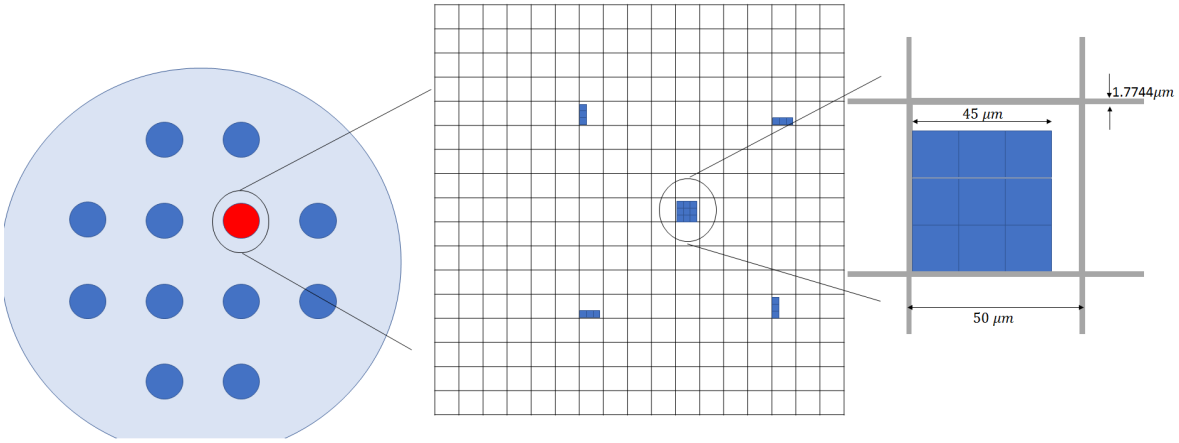

Figure 3.4: Test microlens array on wafer. Each circle on the wafer consists of a square lattice, a part of which is displayed in the middle subfigure.

laser power on the gaps that will not be in accordance with the theoretical results.

For the above reasons, Nanoscribe needs to be tested before printing the final prototype. The testing has been with a simpler structure that consists of fewer number of elements, so that at this stage the printing is not much time consuming. In fact, Nanoscribe needs approximately 5 minutes in order to print one unit cell, so the 1296 elements are printed in 108 hours. Therefore, we resorted to a test solution that includes 21 elements arranged as in Fig. 3.4, which could be printed in less than 2 hours.

We fabricated the test structure twice, once on a silicon wafer coated with silicon oxide and once on silicon only. The test wafers were patterned with 12 identical aliminum grids, shown on the left figure of Fig. 3.4 and we randomly printed the structure on one of the grids that helped us check the alignment capabilities of Nanoscribe. In the centre of the test structure we printed a 3×3 array, while at the corners we printed 1×3 and 3×1 arrays at distances 283 μm (200 μm vertically and 200 μm horizontally) from the centre. Fig. 3.4 shows the wafer with the coated oxide. The wafer without the oxide was used in a later stage and at that stage we had a photomask with slightly different periodicity available to create the grid; however, the principle remained the same.

The alignment of Nanoscribe was tested via comparison of the position of the different components of the structure with respect to the square grid. For this purpose, we observed the test structure with 3 microscopes that are located in the facilities of Else Kooi Lab in TU Delft.

- The Axiotron microscope, which is simple and easy to use
- A scanning electron microscope (SEM), that is capable of observing very small structures in the order of nm thanks to the use of beams of electrons
- The Keyence microscope that is a powerful tool offering many post-processing capabilities.

Fig. 3.5 shows the test structure on the wafer covered with the oxide layer, as it has been captured by the Axiotron microscope. The microlenses per se are not clearly depicted, because the focus of the microscope has been on the level of the grid, so the details of the elliptical parts of the lenses are more than 30 μm out of focus and are not visible. Regarding the alignment, we observe that the components of the structure are at the expected positions with respect to the grid. We remind that the expected positions are the ones shown in the second schematic of Fig. 3.4. However, the limited capabilities of this microscope does not allow us to draw more accurate conclusions on the alignment.

Fig. 3.6 depicts the structure on the wafer that is not covered with oxide, as it appears in the SEM. This wafer is more suitable than the wafer with the oxide, as at the latter the electrons are absorbed by the oxide and lead to a less clear image. From the pictures in Fig. 3.6(c), (d) and (e) we observe that the alignment achieved by Nanoscribe is satisfactory, as all sub-arrays of the test structure touch the metal grid on the one side (x-axis) and have a consistent distance of approximately 1 μm from the grid on the other side (y-axis). Fig. 3.6(a) and (b) are not particularly useful for checking the alignment of the structure, but they are shown, so that we can observe the elliptical parts of the lenses and how detailed they are displayed in the SEM.

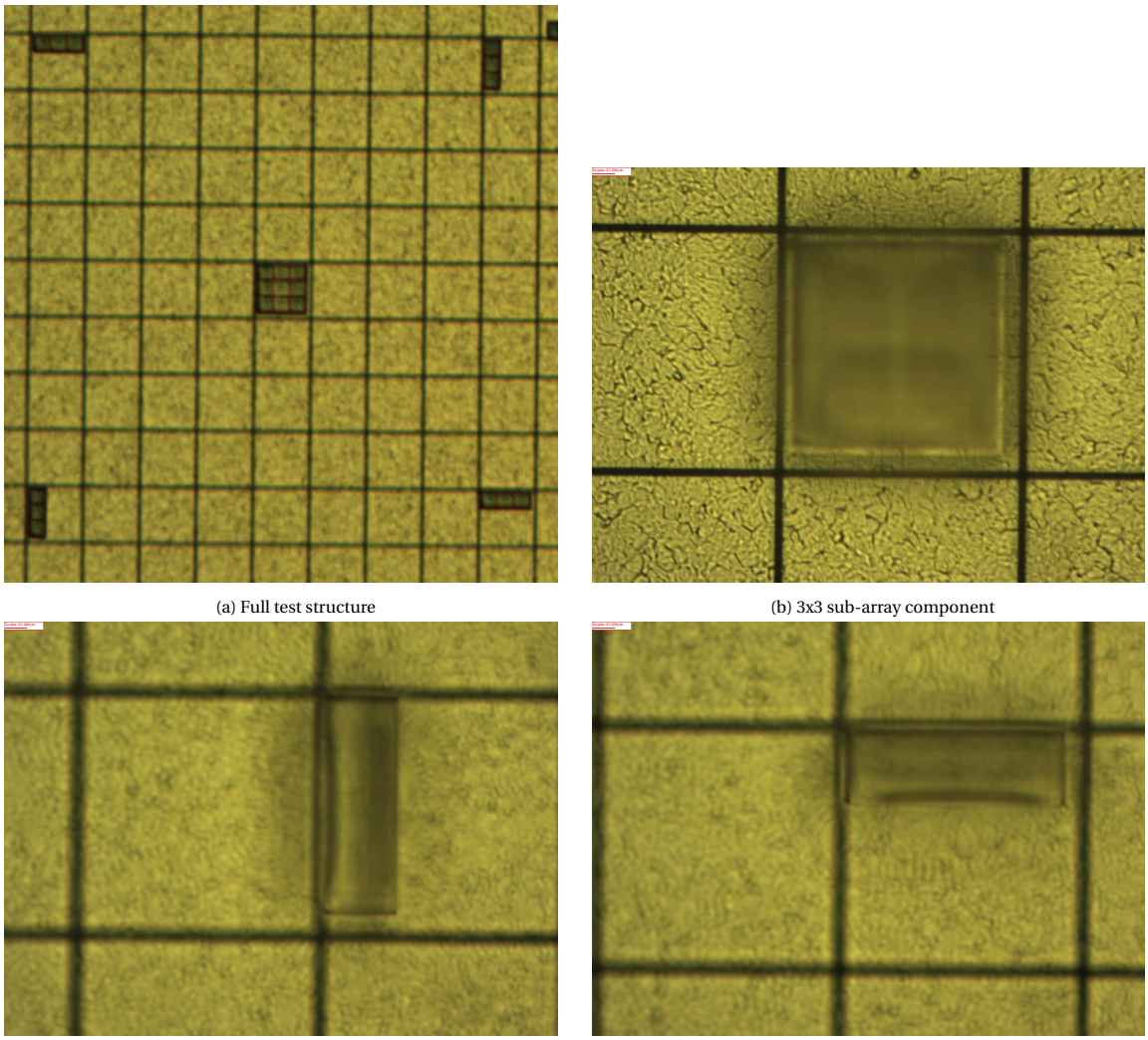

(a) Full test structure

(b) 3x3 sub-array component

(c) 3x1 sub-array component

(d) 1x3 sub-array component

Figure 3.5: The test structure (a) and location of the different components of the test structure with respect to the reference grid (b)-(d), captured by the Axiotron microscope.

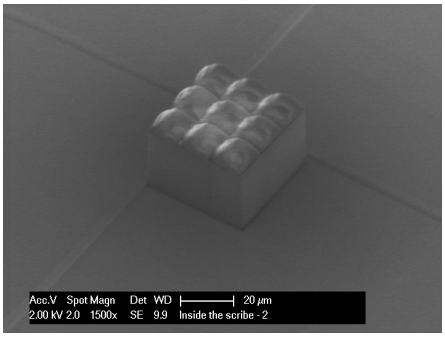

(a) 3x3 sub-array

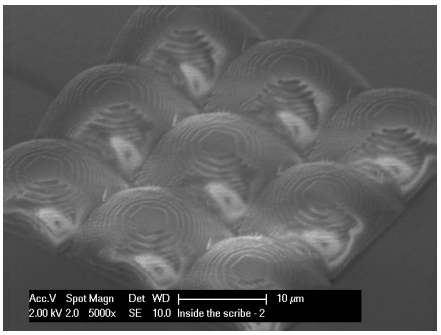

(b) Elliptical part of 3x3 sub-array

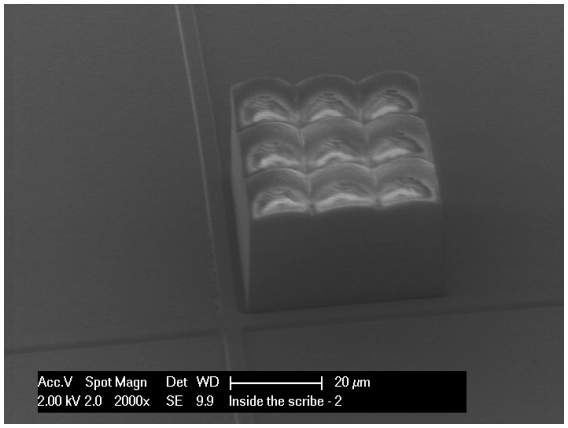

(c) 3x3 sub-array with respect to the grid

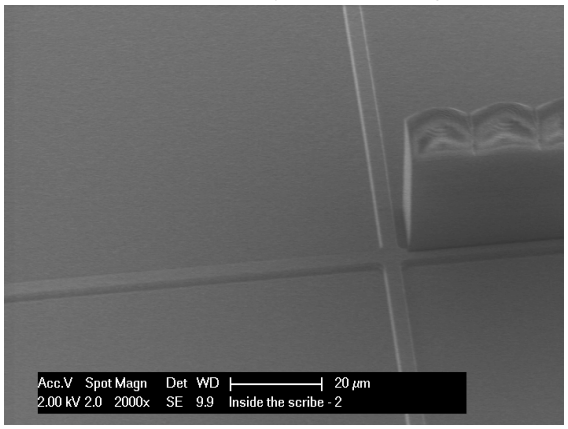

(d) 1x3 sub-array with respect to the grid

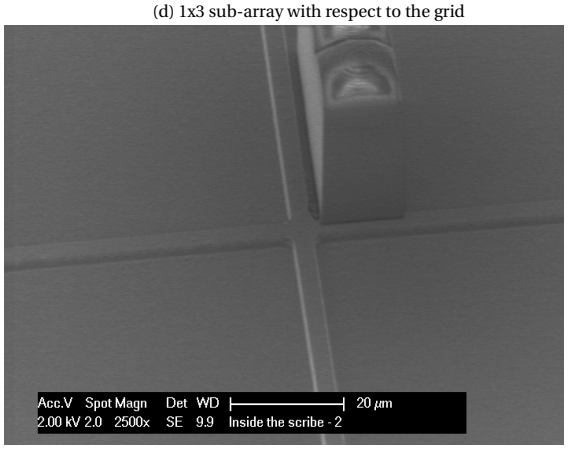

(e) 3x1 sub-array with respect to the grid

Figure 3.6: Images from the SEM.

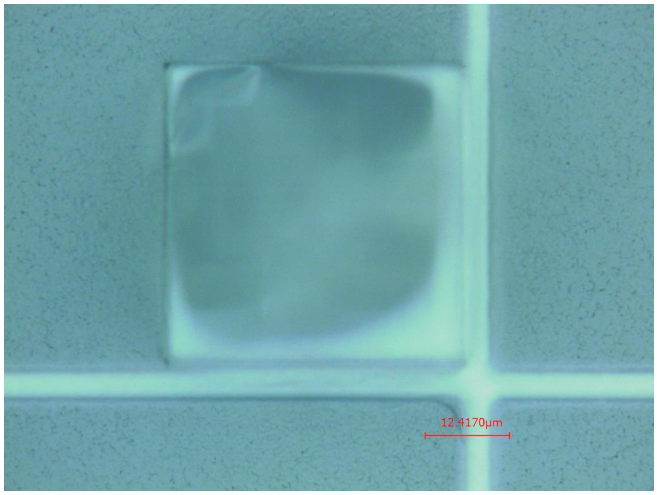

(a) 3x3 sub-array with respect to the grid

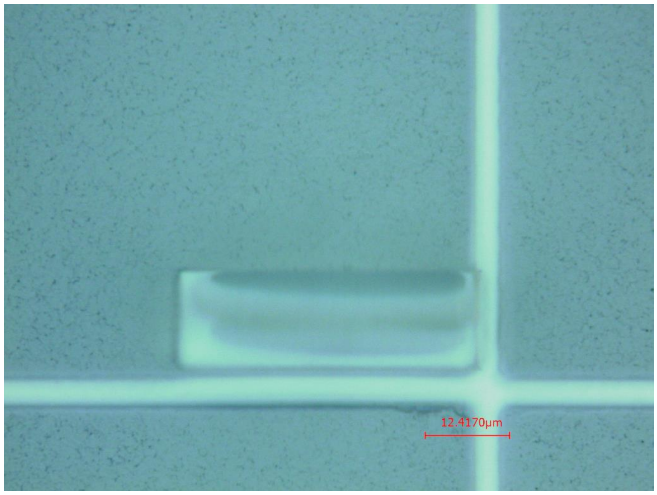

(b) 1x3 sub-array with respect to the grid

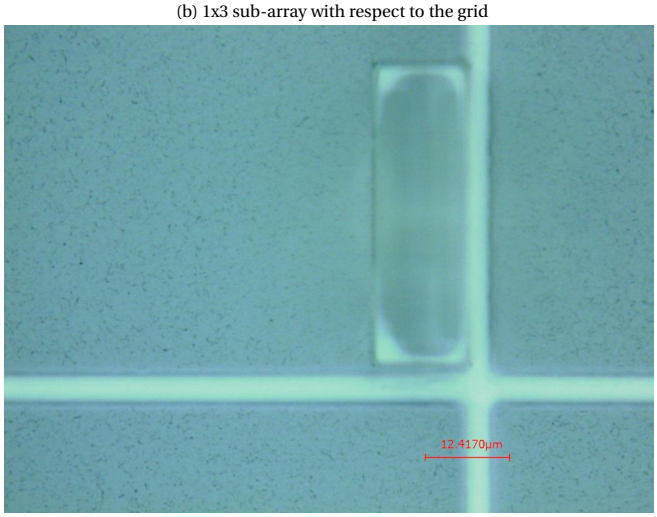

(c) 3x1 sub-array with respect to the grid

Figure 3.7: Images from Keyence indicating the alignment of the structure.

Fig. 3.7 shows similar pictures as before, taken with the Keyence microscope. The wafer that has been used is the one without the oxide layer. The details of the microlenses are not visible due to the focusing of the microscope at the level of the grid, as was the case with the Axiotron microscope. Regarding the alignment, we verify again that it is satisfactory, as the positioning of all components of the test stucture with respect to the reference grid is consistent.

Keyence microscope offers the possibility to reconstruct a 3D representation of the structure of interest, which has been done and depicted in Fig. 3.8. The subfigures on the left side of Fig. 3.8 are from the wafer without the oxide, whereas on the right side we see the microlenses on the wafer with the coated oxide. We observe that the microscope can identify many details of the stucture, such as the thickness of the reference grid and the exact geometry of the microlenses, namely the slab on the bottom part of the microlenses and the elliptical upper part.

From the scale shown in the top left corner of the subfigures, we observe that the maximum height of the structure on the wafer without the oxide is 34.5 μm, whereas the structure on the wafer with the oxide has a maximum height of 31.8 μm. This difference is probably due to a measurement error for the case of the wafer with the oxide. The Solidworks file that was given as input to Nanoscribe defines a height according to the theoretical calculations (Appendix A.4) $f \approx 34.4$. We assume that this difference for the test structure on the wafer with the oxide layer occurred due to the presence of the transparent oxide, whose reference height could not be accurately detected by the microscope. In any case, the error in the height is consistent for all unit cells of the structure, so, we can still make comparisons and draw conclusions for the accurate and consistent printing of the structure.

Figure 3.9 shows the profiles of the elliptical parts of the microlenses, as they were measured with the Keyence microscope. Various elements of the test structure from all of its components were measured and compared with each other, as well as with the anticipated theoretical ellipse. For the microlenses on the wafer with the oxide layer, the theoretical profile has been adjusted to fit the error by assuming a shorter height by 3 μm of the microlenses over their entire area. In the subfigures, when ennumerating the elements in the sub-arrays, we have started counting from left to right and from top to bottom. Furthermore, the diagonal 1 is the diagonal in a unit cell or in the square 3x3 sub-array starting from the top left corner and ending to the bottom right corner and diagonal 2 is vice versa. When we omit the description, diagonal 1 is implied.

The purpose of displaying the profiles of the microlenses is twofold. Firstly, we aim to compare the different microlenses with one another and observe the consistency of Nanoscribe and secondly, we want to compare the printed microlenses with the theoretical curves and check the accuracy of Nanoscribe; if there is a systematic error across all elements, we will need to make small refinements in the model, so that the outcome is closer to the ideal elliptical profile.

We observe that for almost all measurements the microlenses are shorter at the edges than what is expected from the theoretical values. Moreover, there are some irregular dips in the profile. It is important to mention that the majority of the dips occur at the boundary between adjacent elements, which can be either due to a weakness of Nanoscribe to accurately print the transition from one element to another or can be artifacts from the measurements with Keyence. In any case, we expect that sufficient accuracy in the centre of the lens is more important than accuracy close to the rim angle, because close to the centre of the lens the transmission of the laser power is higher. Furthermore, of most significance is the accuracy of the geometries of elements that are in the middle of the structure, since in the actual configuration, the number of non-edge elements will be insurmountably larger than the number of edge elements. Considering this fact and observing the Figs. 3.9a to 3.9d, we can deduce that indeed the middle elements show better accuracy than the edge elements, therefore the test structure is a successful first step for the construction of the entire microlens array.

One last aspect that we could measure with Keyence is the consistency of Nanoscribe to print identical copies of the unit cell of the microlens array in terms of the maximum height of each lens. This can be easily understood from Fig. 3.10, where we see a 2D representation of the 3x3 sub-array with equi-height contours and where we have marked surfaces at the highest part of each lens to compare with the reference level (large rectangular areas surrounding the sub-array). This process has been done for 3 of the 5 components of the structure, the 3x3, a 1x3 and a 3x1 sub-array, for both wafers. The average heights of the selected surfaces of the microlens array are shown in Fig. 3.11. There is a difference of up to a few hundred nm in the maximum heights that is measured for different elements in the structure, that was not expected, as all elements are supposed to be identical. The effect of these differences will be further studied later in this section.

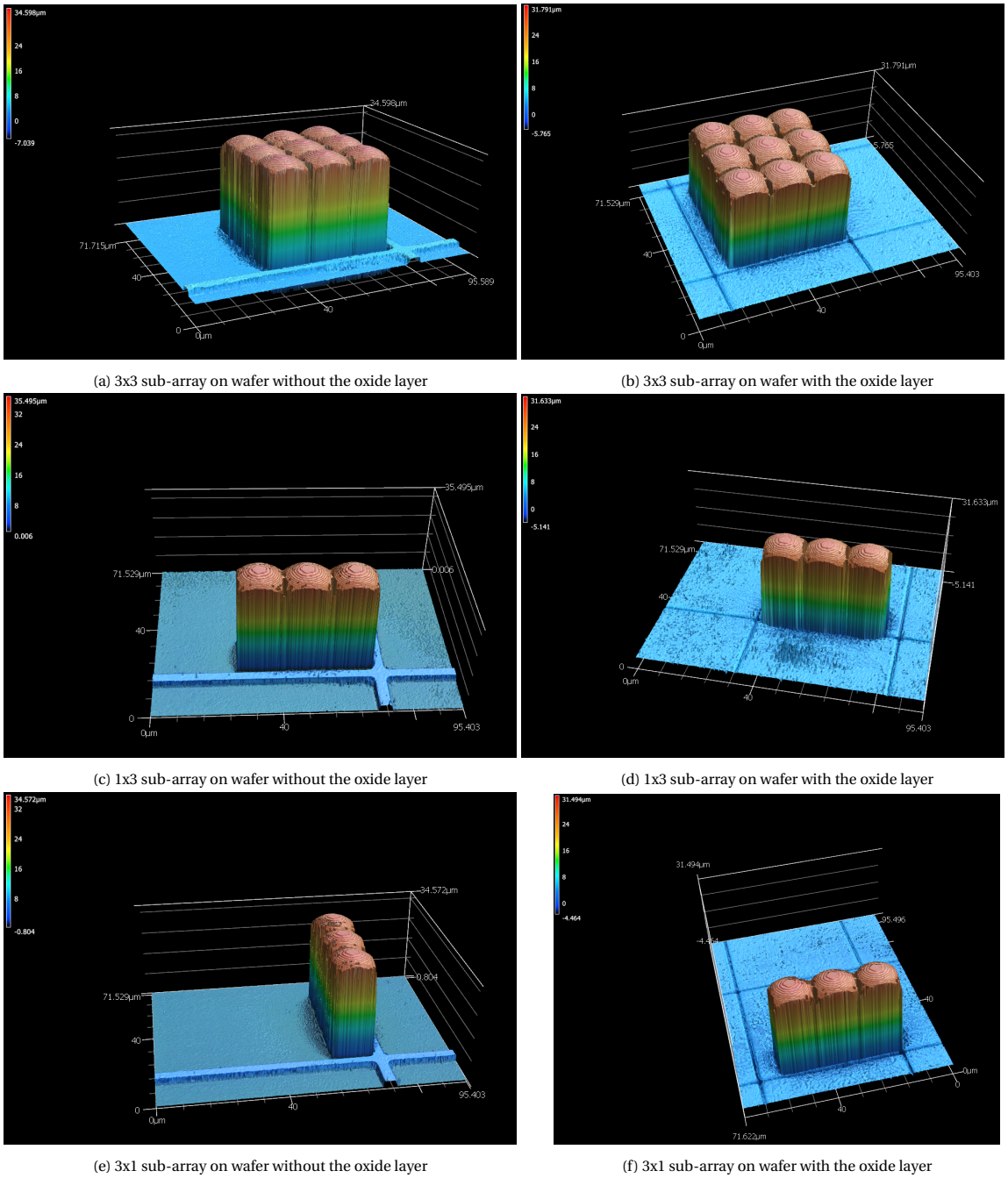

(a) 3x3 sub-array on wafer without the oxide layer

(b) 3x3 sub-array on wafer with the oxide layer

(c) 1x3 sub-array on wafer without the oxide layer

(d) 1x3 sub-array on wafer with the oxide layer

(e) 3x1 sub-array on wafer without the oxide layer

(f) 3x1 sub-array on wafer with the oxide layer

Figure 3.8: 3D representation of the microlenses as derived by Keyence measurements.

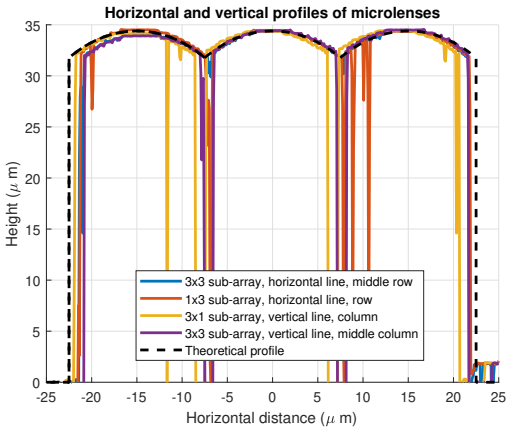

(a) Profile of 3 adjacent microlenses on wafer without the oxide

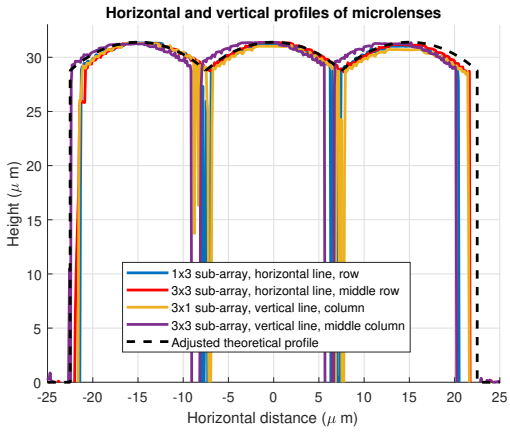

(b) Profile of 3 adjacent microlenses on wafer with the oxide

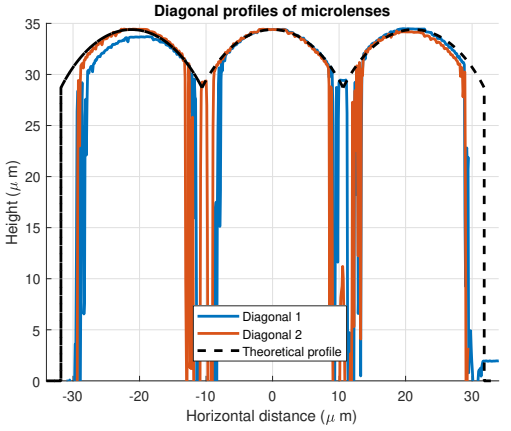

(c) Profile of 3 diagonal microlenses on wafer without the oxide

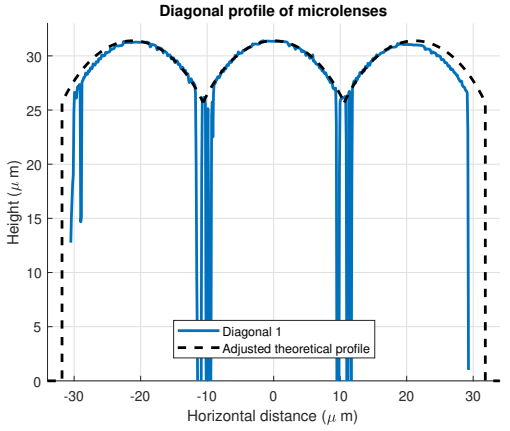

(d) Profile of 3 diagonal microlenses on wafer with the oxide

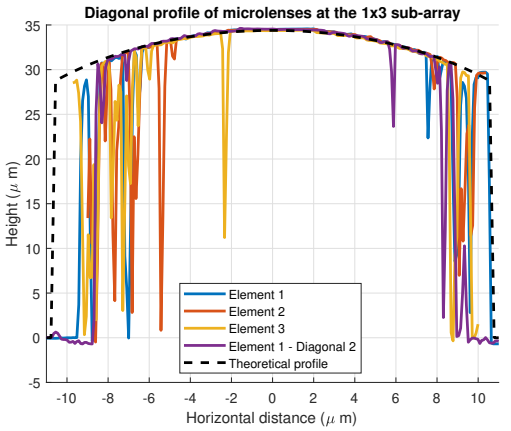

(e) Diagonal profile of individual microlenses of the 1x3 sub-array on wafer without the oxide

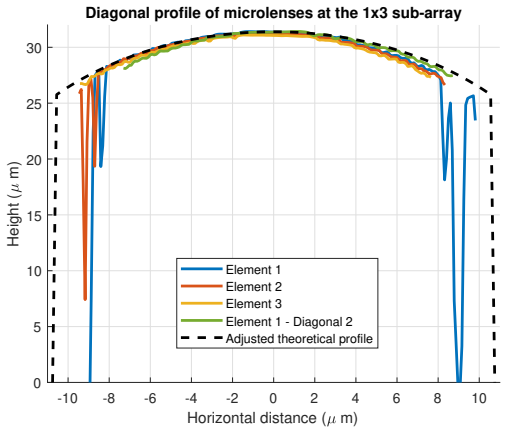

(f) Diagonal profile of individual microlenses of the 1x3 sub-array on wafer with the oxide

Figure 3.9: Profile of elliptical part of the microlenses

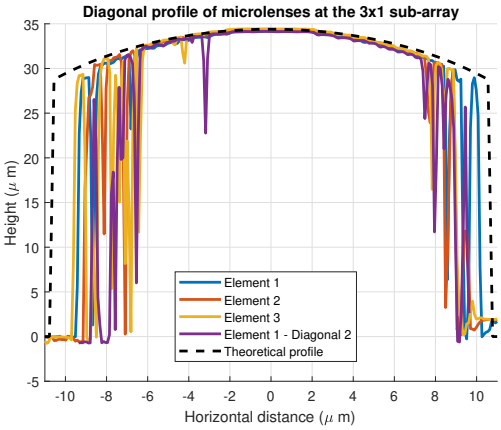

(g) Diagonal profile of individual microlenses of the 3x1 sub-array on wafer without the oxide

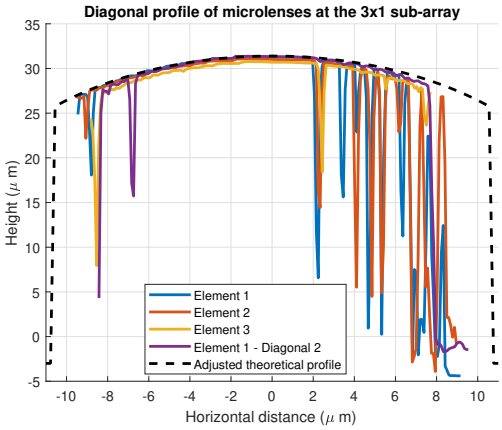

(h) Diagonal profile of individual microlenses of the 3x1 sub-array on wafer with the oxide

Figure 3.9: Profile of elliptical part of the microlenses (cont.)

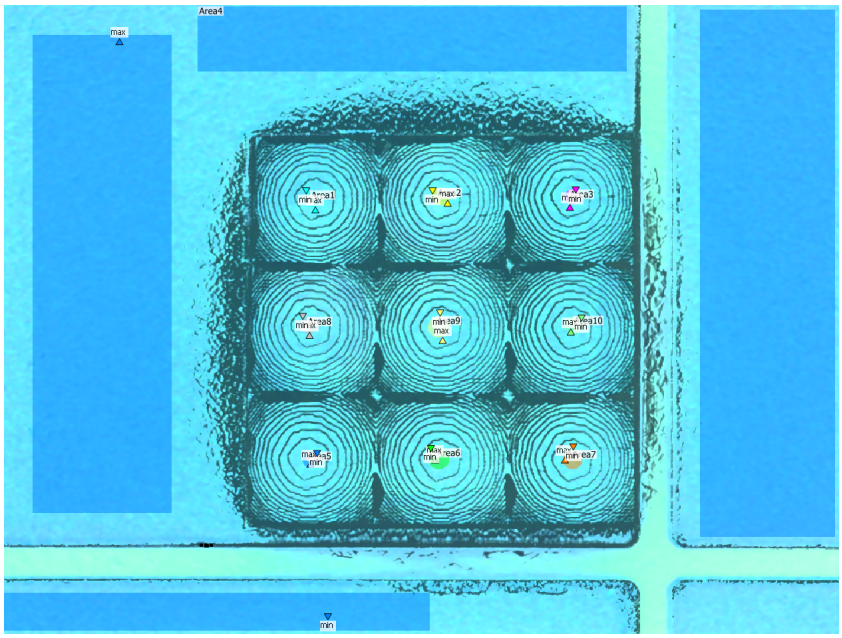

Figure 3.10: Image for comparing maximum heights of the microlenses

(a) Structure on the wafer without the oxide layer

(b) Structure on the wafer with the oxide layer

Figure 3.11: Average heights (in μm) of the surfaces corresponding to the highest part of each microlens.

3.1.3. Aberration due to errors in microlenses fabrication

As already mentioned in the previous section, the middle element of the test structure has a better accuracy in the elliptical shape than the elements located at the edges. From this observation we can conclude that the edge elements are generally more prone to fabrication errors. In the final configuration, this limitation can be overcome by printing dummy elements at the edges. We can, therefore, focus on the middle element and check whether the (minor) fabrication errors will cause aberrations to the incoming laser light.

Unfortunately, in our test structure there is only one element in the microlens array that is completely surrounded by other elements and can be considered a non-edge element. Certainly an analysis of the aberration that can lead to safe results for the whole final 36×36 array needs to be based on more samples. For this reason, we fabricated another test structure, presented in Fig. 3.12, which consists of a 6×6 array, so that, if we consider the elements at the edges as dummy, we can still have 16 elements (in a 4×4 arrangement) that we can analyze.

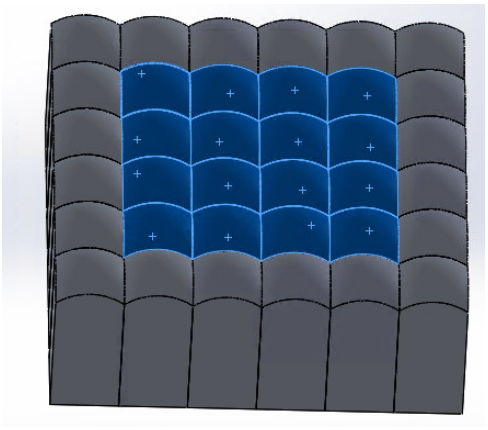

(a) Model in SolidWorks indicating the 16 non-edge elements that will be used in the analysis of the aberration.

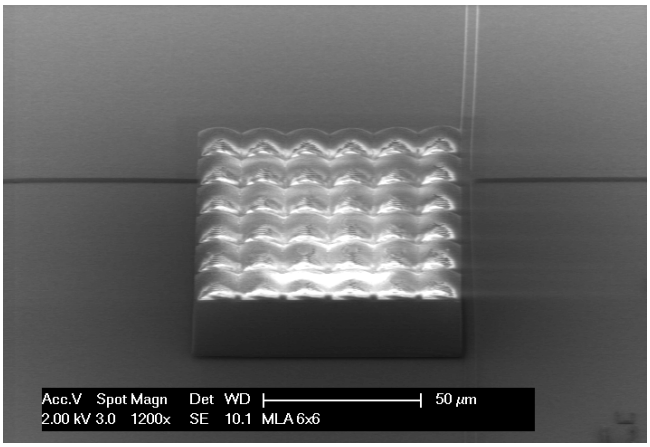

(b) Image of the structure from SEM.

(c) 3D representation of the elliptical parts measured by Keyence.

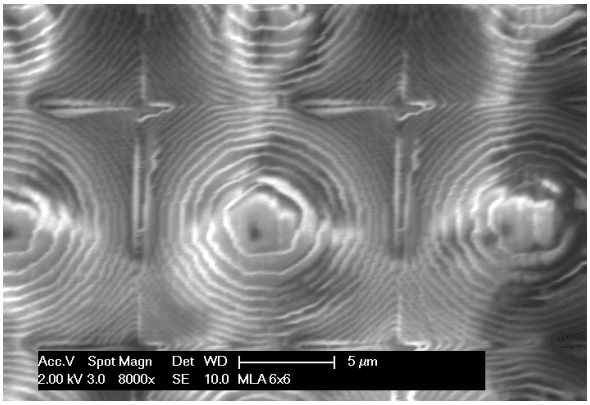

(d) 3D representation of the elliptical parts measured by SEM.

Figure 3.12: The 6×6 test structure

This new test structure was also observed with Keyence, so that we can get useful measurements for the exact profile of the fabricated microlenses. We followed the same procedure as in Section 3.1.2 that resulted in the plots shown in Fig. 3.9, by measuring the profile along vertical, horizontal and diagonal lines of the elements. Specifically, we measured the horizontal and vertical profiles of all 16 elements and the diagonal profiles along the two main diagonals of the 4×4 structure. The initial goal is to fit an axially displaced ellipse to the measured curve of each microlens and calculate the remaining error. In other words, we will try to use a first order approximation to the aberration function $W(x, y)$ = Defocusing + Error. If the error is small compared to the wavelength, aberration effects of higher order should be minor and thus negligible. The fitting of an ellipse with a displacement δz with respect to the designed origin has been via minimizing the mean square error $e^2 = \frac{\sum_{n=1}^{N} \left(measured\_height(n) - displaced\_ellipse(n) \right)^2}{N}$, where N is the number of the discrete points of each microlens measured with Keyence.

# Element	$\delta z\,(nm)$	$\bar{e}\,(nm)$ Diag.	$\bar{e}\,(nm)$ Horiz.	$\bar{e}\,(nm)$ Vert.	$s_e\,(nm)$ Diag.	$s_e\,(nm)$ Horiz.	$s_e\,(nm)$ Vert.	η/η_0
1	-247.6	2.7	-83.2	40.7	143.66	189.56	181.24	0.999
2	-385.2		-12.1	32.3		183.91	162.73	0.997
3	-522.8		-12.7	29.2		170.83	154.06	0.995
4	-687.9	-17.1	-22.5	34.7	373.7	158.54	229.58	0.992
5	-220.1		-30.6	31.3		219.51	167.34	0.999
6	-357.7	6.57	-7.9	14.3	162.34	179.05	165.34	0.998
7	-522.8	-16.4	17.4	49.5	330.16	117.3	161.49	0.995
8	-660.3		-46.9	20.9		114.25	187.49	0.992
9	-220.1		-30.6	28.9		175.23	182.24	0.999
10	-357.7	-50.6	-5.77	46.3	168.8	154.35	90.27	0.998
11	-385.2	-65.8	21.7	73.8	200.72	154.35	90.27	0.997
12	-687.9		-16.5	34.1		116.11	101.73	0.992
13	-247.6	34.7	-8.22	32.9	156.72	112.74	374.53	0.999
14	-385.2		-40.9	30.3		255.14	322.38	0.997
15	-550.3		-43.2	36		202.68	303.3	0.995
16	-715.4	22.2	-44.8	40.9	217.2	306.12	297.18	0.991

Table 3.1: Position of displaced ellipse to fit the fabricated microlenses, mean value of the remaining error, standard deviation of the error after the fitting and decrease in the power efficiency due to the aberration

The displacements δz of the ellipses for each element are given in Table 3.1. The numbering of the elements is according to Fig. C.1. Table 3.1 also includes the mean error and the standard deviation of the error of the profile of the fabricated microlenses with respect to the displaced ellipses. The mean values and standard deviations are displayed for all available data per element, which can be the measurements along a horizontal line, a vertical line and a diagonal line. The measured profiles of the microlenses are given, in comparison with the original and the refined ideal elliptical shape, in Appendix C.

The wavelength of the laser in the resin is $\lambda_d = \frac{c_0}{f \cdot n} \approx 520nm$ for $n \approx 1.5$. The mean error and standard deviation of the error are quite smaller than the wavelength, which implies that higher-order aberrations will not have a strong effect and can be neglected. Therefore, the defocusing term describes satisfactorily the aberration that occurs due to imperfections of the fabrication.

Due to the defocusing, the excitation gaps of the connected dipoles are no longer located at the focal plane of the microlenses, but they are out of focus on the axial direction. Therefore, the electric field at the excitation gaps, which will eventually cause the increase in the conductivity of the LT-GaAs, will be different compared to the electric field calculated in [23] for the ideal case. We expect that the total power at the excitation gaps will be lower than the total power at the absence of aberration, so the generator impedance in the equivalent Norton circuit of the PCA will be a bit larger and the matching condition with the active input impedance of the connected dipole array will not be fulfilled.

We can quantitatively estimate the aberrated electric field at the excitation gaps as

$$\vec{e}(\vec{r}) = \int_S [\overline{\overline{g}}^{em} \vec{m}(\vec{r}') + \overline{\overline{g}}^{ej} \vec{j}(\vec{r}')]\, d\vec{r}'$$

where $\overline{\overline{g}}$ is the Green's function, $\vec{m}(\vec{r}')$ denotes the equivalent magnetic current sources and $\vec{j}(\vec{r}')$ denotes the equivalent electric current sources located at the FO sphere S. The configuration is shown in Fig. 3.13. We can apply certain approximations to the expression above, according to [46], and result in the expression for the electric field at an observation point $\vec{r}$ at the connected dipoles' plane with coordinates $\vec{r} = x\,\hat{x} + y\,\hat{y} + \delta z\,\hat{z}$

$$\vec{e}(\vec{r}) = \frac{jRe^{-jk\frac{r^2}{2R}}}{2\pi} \int_{-ksin\theta_0}^{ksin\theta_0} \int_{-ksin\theta_0}^{ksin\theta_0} \vec{e}_{GO}(k_x, k_y) e^{j(k_x x + k_y y + k_z \delta z)} \frac{1}{k_z} dk_x\, dk_y$$

where

$$
\begin{aligned}
&R \text{ is the radius of the FO sphere}\\
k &= \frac{2\pi\sqrt{\epsilon_r^{resin}}}{\lambda_0}\\
\theta_0 &= sin^{-1}\left(\frac{\frac{D}{2}}{R}\right)\\
\vec{e}_{GO} &= S_{spread}[\tau^{||}(\hat{p}_i\cdot\hat{\rho})\hat{\theta}+\tau^{\perp}(\hat{p}_i\cdot\hat{\phi})\hat{\phi}]E_0\\
S_{spread} &= \frac{a(1-e^2)}{R(1-ecos\theta)}\\
&\hat{p}_i = \hat{x} \text{ is the polarization of the incident wave}\\
k_z &= \sqrt{k^2-k_x^2-k_y^2}
\end{aligned}
$$

The electric field at the plane of the dipoles will have all 3 components x, y, z; however, given a polarization of the incident laser wave along $\hat{x}$, the dominant component of the electric field at the plane of the dipoles will also be along x. The x-component is

$$
e_x(\vec{r}) = \frac{jRe^{-jk\frac{r^2}{2R}}}{2\pi}\int_{-ksin\theta_0}^{ksin\theta_0}\int_{-ksin\theta_0}^{ksin\theta_0} e_{GO}^{x}(k_x,k_y)e^{j(k_x x+k_y y+k_z\delta z)}\frac{1}{k_z}dk_x\,dk_y \tag{3.1}
$$

where

$$
e_{GO}^{x} = e_{GO}^{\theta}\,cos\theta\,cos\phi + e_{GO}^{\phi}\,sin\phi
$$

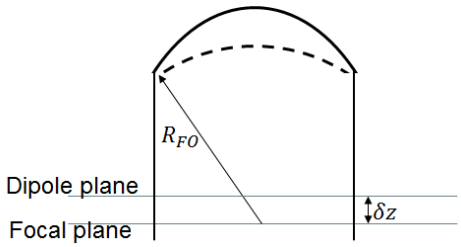

Figure 3.13: Model of the displaced elliptical microlens (solid line) and the FO sphere (dotted line). The displaced focal plane and the plane where the connected dipoles are located is also shown

The integral can be computed numerically. The plots of the electric field for each of the fabricated elements are given in Appendix C and they clearly show how a large displacement of the focal plane affects the electric field at the excitation gaps of the dipole. The defocusing indeed causes a decrease in the average power at the gaps. In the last column of Table 3.1 we give the decrease of the efficiency

$$
\eta = \frac{\frac{1}{2\zeta_d}\int_{-w_{gap}/2}^{w_{gap}/2}\int_{-w_{gap}/2}^{w_{gap}/2}|E(x,y)|^2\,dx\,dy}{P_{laser}^{unit\ cell}}
$$

in the presence of the the aberration compared to the efficiency η_0 in the ideal case with zero aberration. In [23], the efficiency η_0 has been calculated to be equal to approximately 0.556, which is, however, an optimistic efficiency because there are some approximations in the expression that gives this value. The relative efficiency has not decreased more than 99% in any of the fabricated microlenses, so we expect that the impact on the equivalent Norton circuit will not be significant.

3.1.4. Microlens material options

One of the most common materials for Nanoscribe is IP-Dip, which is suitable for printing submicron features. The refractive index of IP-Dip at 780 nm is $n_{IP-Dip} = 1.54$ [42]. Another candidate material is IP-S,

with refractive index at 780 nm $n_{IP-S} = 1.5$, according to [42]. IP-S has also been selected in [42], because of the faster printing time compared to IP-Dip, which is, however, at the expense of resolution. Considering the smaller dimensions of the microlenses in this project with respect to [42], we have preferred the IP-Dip over IP-S at our test structures.

The drawback of IP-Dip is the printing time, which for this size of the microlens array is almost prohibitive. An alternative solution to reduce the printing time is the use of SU8 photoresist whose refractive index at 780 nm is $n_{SU-8} = 1.58$. The advantage of SU8 is its availability in the cleanroom, where we can deposit a big orthogonal slab on the wafer in a short time. Thus, we can separate the printing work in two stages, which are presented in Fig. 3.14. The first stage is the deposition of the bottom part of the microlens array in the cleanroom with SU8 and the second stage is the printing of the ellipsoidal upper part of the microlens array with Nanoscribe. The material used in Nanoscribe can be either IP-Dip or SU8.

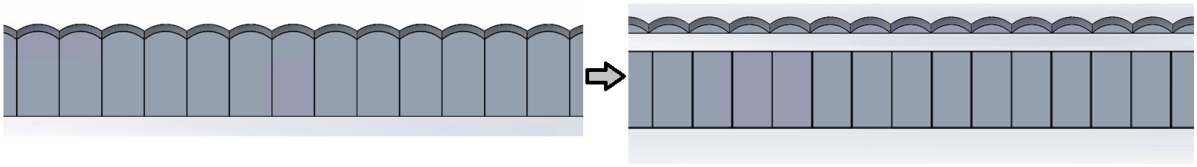

Figure 3.14: Splitting of the microlens array in 2 parts to accelerate the printing

In any case, the focal distance of the microlens array needs to be adjusted, because in [23] we have considered a refractive index of the material equal to 1.5, which will not be exactly the refractive index of the utilized material. In case IP-Dip is used for the whole microlens array, the focal distance will be 35.1 μm (less than 1 μm longer), whereas if SU8 is used, the focal distance will have to be 35.82 μm.

3.2. Antennas

The microlens array in this project is supposed to be integrated in the whole PCCA structure, which means that it must be printed on top of the wafer on which we will have already prepared the rest of the components. The preparation of the wafer will be done according to the state of the art procedure that is described in Section 1.

As mentioned in Section 1, the antenna pattern is specified by the photomask during the photolithography stage. For this project and for the prototype fabrication we have designed the mask with the L-Edit software [45]. The mask corresponds to a standard 3-inch GaAs wafer on top of which we will print the antenna. As the dimension of the designed connected dipole array including the bias metal pad is equal to 5 mm, it did not make sense to use the 3-inch wafer only for this single realization. Instead, we have splitted the wafer into several dice and in each we intend to implement a different antenna. Our initial antenna pattern on the mask is shown in Fig. 3.15, as a part of the whole wafer.

Due to the limited availability of LT-GaAs wafers in the lab and the cost of such wafers, we did not proceed to the fabrication of this single connected dipole array. All dice need to be filled with different variations of the antenna, which, however, have to be carefully designed and theoretically optimized. Therefore, this part of the fabrication will be left for future research.

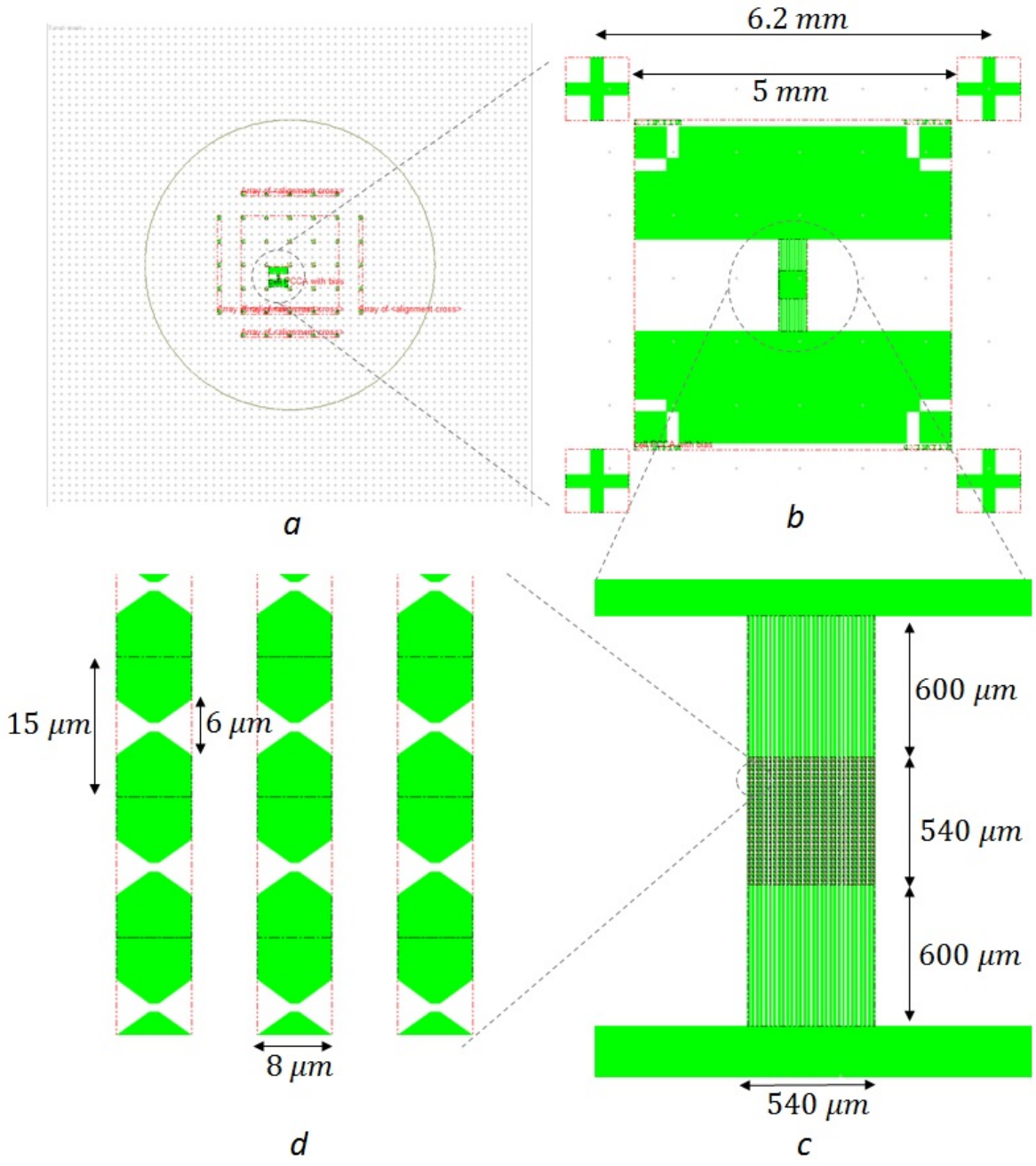

Figure 3.15: Mask including the connected dipole array pattern

3.3. Considerations for misalignment between microlenses and dipoles

Until now we did not take into account the complexity that is involved in integrating the microlens array with the connected dipole array. The microlens array is supposed to be printed with Nanoscribe on the wafer on which we will already have patterned the connected dipole array. The microlens array must be perfectly aligned to the connected dipole array; basically each unit cell of the microlens array should coincide with a unit cell from the connected dipole array. Since the width of the excitation gap of the connected dipoles is only 1 μm, even a slight misalignment may lead to much of the available laser power not reaching the desired excitation area and therefore distorting the expected matching condition of the generator impedance to the antenna impedance. This strict requirement is very challenging and difficult to achieve during the fabrication, therefore, we need to know in advance how to compensate for a potential misalignment.

A solution to this problem is the illumination of the laser with an angle that depends on the misalignment. For slight misalignments, which is the most likely case, the angle of incidence of the laser beam does not need to be large, which facilitates the calculations of the electric field, as we can apply certain approximations, according to [46]. Specifically, if we assume that the laser beam impinges on the microlens surface from a direction $(\Delta\theta_i, \phi_i)$ with respect to the broadside direction, then the energy will be concentrated on the flash point, which is located at the direction

$$\vec{\rho}_{fp} = R\frac{\vec{\Delta k}_{\rho i}}{k_0}$$

from the focal point of the lens, where

$$R = 32.647\mu m \text{ is the radius of the FO sphere}$$
$$\vec{\Delta k}_{\rho i} = k_0(sin\Delta\theta_i cos\phi_i \hat{x} + sin\Delta\theta_i sin\phi_i \hat{y})$$

From the above expressions we can find which angle of incidence is required to maximize the received laser power, if we know that the connected dipoles are misaligned with respect to the microlenses by a vector $\vec{\rho}_{fp} = x_{fp}\hat{x} + y_{fp}\hat{y}$. The angle of incidence is defined from its deviation angle from broadside $\Delta\theta_i$ and azimuth angle ϕ_i

$$\phi_i = tan^{-1}\Big(\frac{y_{fp}}{x_{fp}}\Big)$$
$$\Delta\theta_i = sin^{-1}\Big(\frac{x_{fp}}{k_0 cos\phi_i}\Big)$$

For very small angles of incidence the electric field at the focal plane can be simply considered as a translation of the electric field for broadside illumination to the direction indicated by the flash point. For larger angles, we need to take into account the contribution of the coma phase, which creates an asymmetry at the side lobes. However, since we are interested only in the -3 dB diameter of the main lobe of the electric field, we can neglect the coma phase term, because it does not affect the main lobe.

Following the same steps as in Appendix A.4.2, the electric field at the focal plane is

$$e_{xf}(x_f, y_f) \approx \frac{1}{2\pi}\frac{jE_0^{PW}e^{-jkR}}{k}\frac{c(1+e)}{e}\tau_{||}(0)2k\cdot sin\theta_0\cdot sinc\Big(\frac{kD}{2R}(x-x_{fp})\Big)\cdot 2k\cdot sin\theta_0\cdot sinc\Big(\frac{kD}{2R}(y-y_{fp})\Big)$$

The electric field at the focal plane is shown in Fig. 3.16a for a small angle of incidence. For a reference we include the pattern of the electric field at the focal plane for broadside incidence (Fig. 3.16b). We observe that indeed by stirring the laser beam we can compensate for a misalignment in the $x-y$ plane between the microlens array and the connected dipole array. This effect also holds if we consider the defocusing that will occur due to fabrication errors.

The misalignment is not possible to be detected, because the resin used by Nanoscribe is not transparent and we are not able to see the excitation gap through the resin at the microscope. The best way to determine the optimal angle of incidence for the laser power is by checking the radiated power by the PCCA for changing angles of incidence. It is obvious that radiated power is maximized when the angle of incidence leads to the flash point coinciding with the centre of the excitation gap of the dipoles.

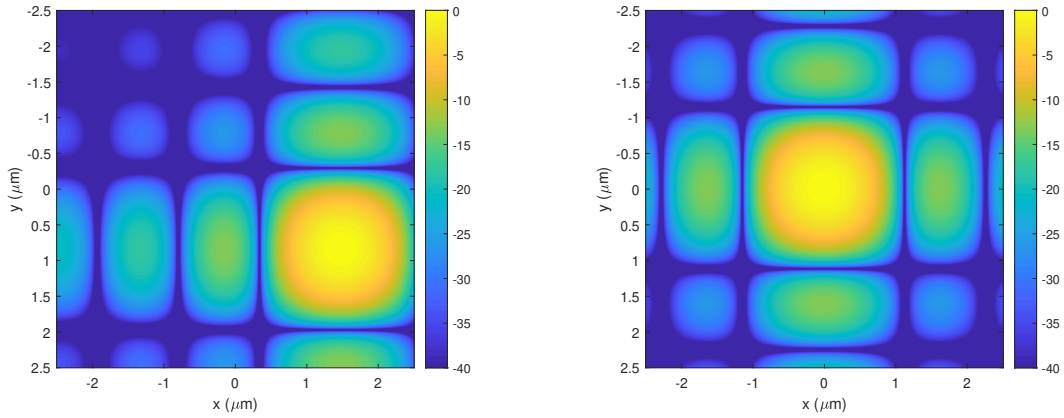

(a) Off-broadside incidence

(b) Broadside incidence

Figure 3.16: Normalized electric field at the focal plane of a microlens when the incidence of the laser beam has an angle $(\Delta\theta_i, \phi_i) = (3°, 30°)$, compared to the electric field upon broadside incidence.

4

A PO Matlab Tool for Lens Antennas in Tx

This chapter could be considered a separate part from the rest of the thesis, as it provides information on a tool that calculates the fields radiated by a generic lens antenna with a random feed. However, this tool has facilitated the calculation of the secondary fields of our PCCA in Sec. 2.2, so it is an important contribution for the thesis. The generic nature of the code that covers different lens types of any dimensions and any feed makes the user-friendly GUI version a valuable tool for every engineer that wishes to design a lens antenna or analyze its performance.

The structure of the chapter is the following. First, a brief description of the main functions of the tool is given. After that, we present the GUI and explain more of its functionality.

4.1. Principle

The principle of the tool is the following. Firstly, it receives as input the far field of the feed of the lens at a certain frequency, as well as geometrical parameters of the configuration. From the given far field of the feed it computes the GO electric and magnetic fields along the exterior part of the lens surface, using Snell's law and the Fresnel law. At this stage, the tool takes into account the presence or absence of a matching layer. The matching layer is generally necessary when the lens is made of a dense material, because otherwise most of the power is reflected at the lens-air boundary. The ideal implementation of the matching layer is a quarter-wavelength layer, at a frequency which is usually at the centre of the operation band of the antenna. The permittivity of the layer is $\epsilon_{r,m} = \sqrt{\epsilon_{r,d}\epsilon_{r,0}} = \sqrt{\epsilon_{r,d}}$. However, in a real-case scenario it is hardly likely that a material with permittivity exactly equal to $\epsilon_{r,m}$ exists, so the user is free to select the permittivity and thickness of the matching layer.

Subsequently, according to the equivalence theorem, electric and magnetic current sources are assumed on the surface of the lens, defined as

$$\vec{J}_{eq} = \hat{n} \times \vec{H}^{GO} \tag{4.1}$$

$$\vec{M}_{eq} = \vec{E}^{GO} \times \hat{n} \tag{4.2}$$

where $\hat{n}$ is the normal unit vector at the lens surface. The far field radiated by these equivalent sources is then

$$\vec{E}^{far}(\vec{r}) = \Big[-\omega\mu(\tilde{I} - \hat{r}\hat{r}) \iiint_v \vec{J}_{eq}(\vec{r}\,')e^{jk\hat{r}\cdot\vec{r}\,'} d\vec{r}\,' + k\hat{r} \times \tilde{I} \iiint_v \vec{M}_{eq}(\vec{r}\,')e^{jk\hat{r}\cdot\vec{r}\,'} d\vec{r}\,' \Big] \frac{je^{-jkr}}{4\pi r}$$

$$\vec{H}^{far}(\vec{r}) = \Big[-\omega\epsilon(\tilde{I} - \hat{r}\hat{r}) \iiint_v \vec{M}_{eq}(\vec{r}\,')e^{jk\hat{r}\cdot\vec{r}\,'} d\vec{r}\,' - k\hat{r} \times \tilde{I} \iiint_v \vec{J}_{eq}(\vec{r}\,')e^{jk\hat{r}\cdot\vec{r}\,'} d\vec{r}\,' \Big] \frac{je^{-jkr}}{4\pi r}$$

Since we have fully determined the electric and magnetic field inside and outside of the lens, the calculation of the Poynting vector and the radiated power for the specified frequency is straightforward as

$$\vec{S}(\vec{r}) = \vec{E}(\vec{r}) \times \vec{H}^*(\vec{r})$$

$$P = \iint_{lens\ boundary} \vec{S}(\vec{r}) \cdot \hat{n}\, dS$$

If the antenna supports broadband operation and many frequencies have been taken into account, the total radiated power will then be

$$P_{total} = \int_{f_{min}}^{f_{max}} P(f)\, df.$$

4.2. Graphical user interface

The contribution of this thesis in this Matlab tool is the creation of a GUI that can be installed as a Matlab App by any Matlab user. The aim of the GUI is to be a user-friendly environment in which someone can find the electric field pattern radiated by a lens antenna, as well as get some results on the directivity and efficiency of the antenna. What the user must know in advance and give as input to the App is the lens configuration, such as type of lens, presence or absence of matching layer, lens diameter and the rim angle of the lens. Furthermore, the user has the freedom to select the distance at which the field needs to be computed and the angular resolution of the field pattern. Finally, the user needs to give as input the electric field of the feed and its polarization, as well as the frequency or frequencies of operation.

The options for the lens type are elliptical, hyperhemispherical, synthesized elliptical or user defined extended hemispherical. The hyperhemispherical lens is defined as the extended hemispherical lens with the extension length equal to R/n. For this type of lens, the rays outside of the lens are assumed to be originating from a virtual focal point located at a distance $R_s \cdot (1+\sqrt{\epsilon_r})$ from the centre of the lens boundary with the air. Here R_s is denoted the radius of the spherical part of the lens. The virtual focal distance is calculated automatically by the tool and is presented in the GUI. The user defined extended hemispherical lens is a more general type of lens, where the user is free to select the additional extension length as well as the virtual focal distance. The option for elliptical lens yields a lens with eccentricity $e = 1/\sqrt{\epsilon_r}$. After transmission through the lens the rays are parallel to each other and parallel to the axis of revolution of the lens, so the virtual focus is located at an infinite distance from the lens. Finally, the synthesized elliptical lens is an extended hemispherical lens that resembles the elliptical lens in shape and has properties similar to the elliptical lens.

All the above are depicted in Fig. 4.1, which shows the main window of the GUI. In the figure, we have put some typical initial values. Detailed explanation with figures showing each step and unveiling the entire functionality of the GUI are shown in Appendix D. Here we explain briefly the main inputs and outputs of the GUI.

The second column in the main window of the App contains information about the feed and the frequency of operation for the antenna. In terms of the feed, the user can shift the phase center of the feed, according to the characteristics of the feed antenna. Also the polarization needs to be specified, which can be either horizontal or vertical. This option affects the calculation of the co-polarized and cross-polarized components of the electric and magnetic field, which are expressed according to Ludwig's third definition [36] as

$$\vec{E}_{co} = E_\theta cos(\phi) - E_\phi sin(\phi)$$
$$\vec{E}_{cx} = E_\theta sin(\phi) + E_\phi cos(\phi)$$

if the polarization of the feed is horizontal (along $\hat{x}$ direction), and

$$\vec{E}_{co} = E_\theta sin(\phi) + E_\phi cos(\phi)$$
$$\vec{E}_{cx} = E_\theta cos(\phi) - E_\phi sin(\phi)$$

if the polarization of the feed is vertical (along $\hat{y}$ direction). The expressions for the magnetic field are the same as the ones for the electric field.

Under the polarization selection, the user needs to upload the field patterns of the lens feed. These can be given either as a `.cut` file, which is an output from CST, or as `.mat` files from Matlab. In the case of the Matlab files, the GUI also asks for the θ and ϕ (or u and v) meshgrid that corresponds to the electric field arrays. For the CST option, a new window pops up, where the user needs to set the range and the step of the discretization of θ and ϕ. The upload of the files with the fields is requested as many times as the number of frequencies, which are specified at the top of the second column.

After giving all necessary input parameters, the user can then get the field radiated by the lens antenna. This is accomplished in two stages. First, the tool plots the far field pattern of the feed of the lens and the equivalent electric current at the lens surface. The second stage is the calculation of the electric and magnetic field at the distance and at angles specified by the user at the bottom of the first column in the main window of

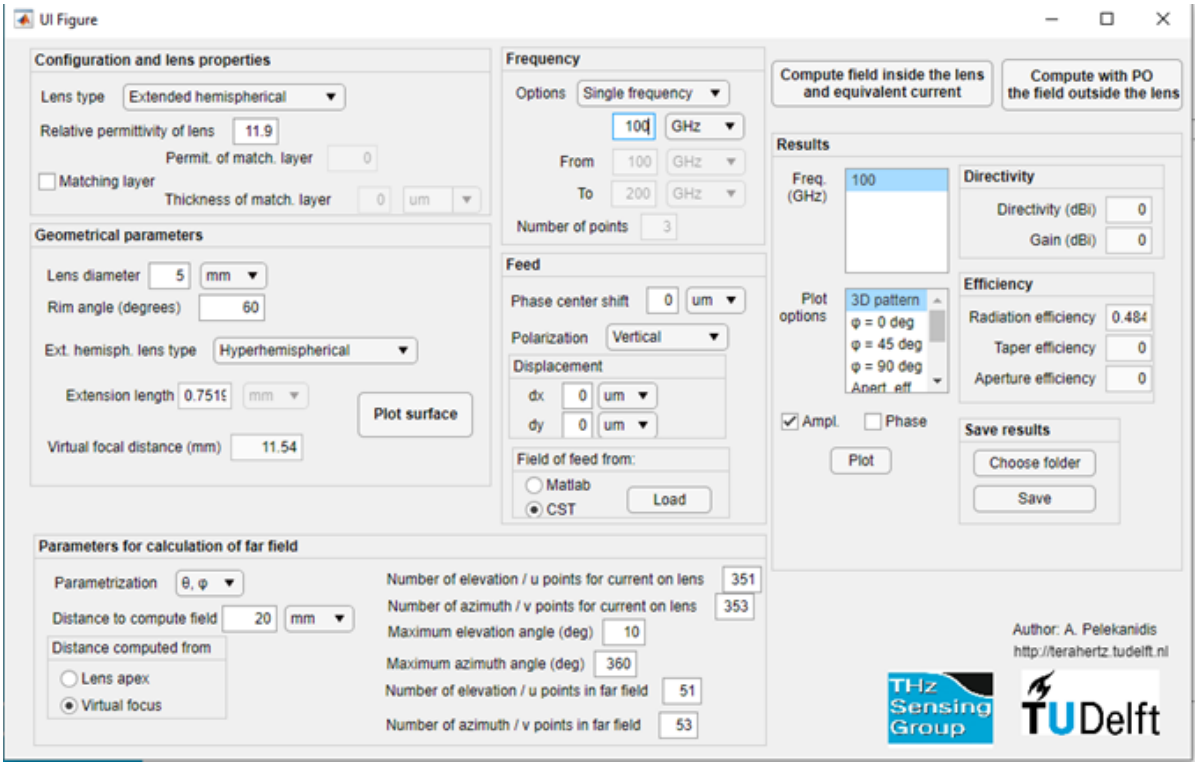

Figure 4.1: GUI of the PO tool for lens antennas in transmission

the GUI. Besides the plot of the far field pattern for the electric field, the tool presents results on the directivity, gain and the efficiency of the antenna. The radiation efficiency is equal to the proportion of the useful power that is transmitted through the lens boundary to the air and is defined as

$$\eta_{rad} = \frac{P_{tx,lens}}{P_{rad,feed}} = \frac{\iint_S (\vec{E}^{GO} \times \vec{H}^{GO*}) \cdot \hat{n} dS}{\frac{1}{2\zeta_d} \int_0^{\pi/2} \int_0^{2\pi} |\vec{E}|^2 sin\theta \, d\phi \, d\theta} \tag{4.3}$$

which is basically the same as the reflection efficiency described in Section 2.1.5.

Another efficiency calculated by the Matlab tool and presented in the GUI is the taper efficiency, which is defined as

$$\eta_{tap} = \frac{D(0,0)}{\pi^2 \left(\frac{D_{lens}}{\lambda}\right)^2}$$

and expresses how good the directivity, and therefore the angular resolution, is, compared to the maximum achievable directivity. In the above equation, $D(0,0)$ is the directivity at broadside direction, D_{lens} is the lens diameter and λ is the wavelength at at the frequency of interest in air. The taper efficiency and the radiation efficiency give the total aperture efficiency of the lens antenna via the expression

$$\eta_{ap} = \eta_{rad} \cdot \eta_{tap}.$$

Finally, the gain that is displayed in the Directivity section is equal to

$$G = \pi^2 \left(\frac{D_{lens}}{\lambda}\right)^2 \cdot \eta_{ap}$$

4.3. Validation of the GUI

In this section we will try to prove the accuracy of the GUI, by comparing the results that we obtain from the tool with results of the far field obtained with CST. For the validation we will use the double slot antenna, presented in Fig. 4.2, which has been mentioned in [31] as a suitable feed for a silicon lens antenna. The dimensions of the double slot are the ones chosen in [31], so that we can have a reference for the field patterns from the literature as well. These dimensions are

- length of slots $L = 0.28\lambda_0$
- distance between slots $d = 0.16\lambda_0$
- lens diameter $R = 13.7\,mm$
- frequency $f = 246\,GHz$.

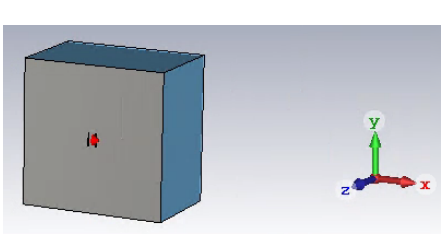

(a) Stratified configuration with the double slot antenna

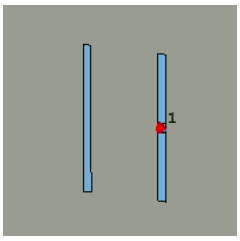

(b) Double slot antenna

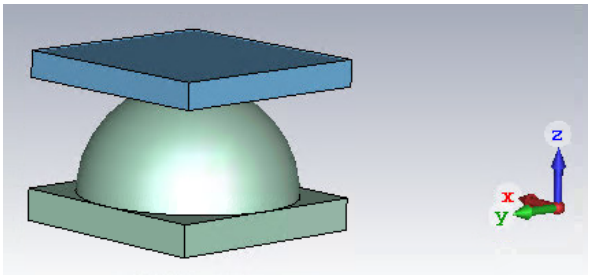

(c) Lens antenna with the double slot as feed

Figure 4.2: CST images of the double slot as a standalone component in the lens stratification and as a feed in the lens antenna

Firstly, we need to find the field radiated by the double slot, which we will give as input to the GUI. We assume that the lens surface is in the far field region of the double slot antenna, and therefore we can find the field of the feed by considering a stratification that consists of a semi-infinite region of air, a semi-infinite region of silicon and the double slot antenna on their interface. In order to validate the accuracy of the theoretical calculations, we also modelled the configuration in CST as in Fig. 4.2a, where we have designed the double slot on a PEC plane (Fig. 4.2b), a cylinder of vacuum whose size is several times the wavelength and silicon as the background material. The theoretical results are compared with CST and with the literature in Fig. 4.3. The results are in very good agreement with each other.

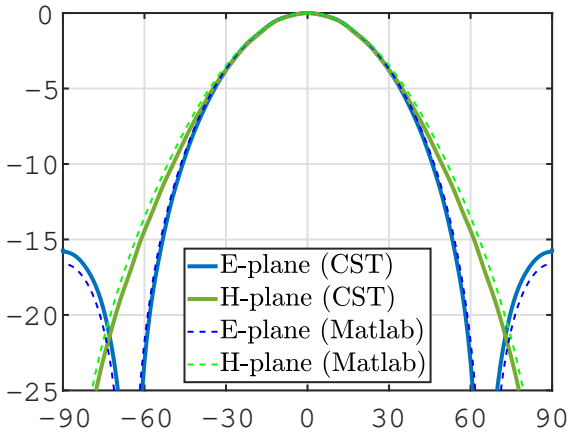

(a) Theoretical and CST results

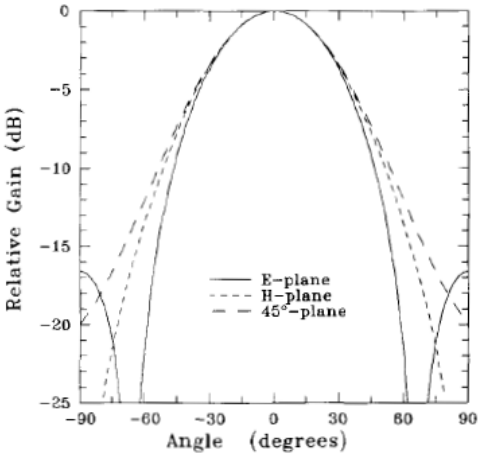

(b) [31, p. 1740]

Figure 4.3: Normalized far field of the double slot antenna

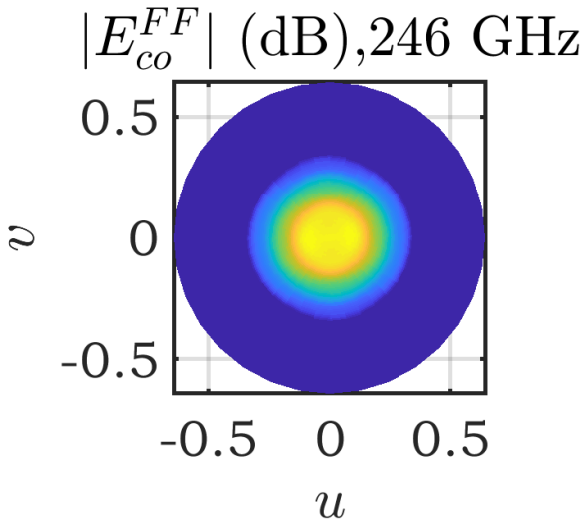

(a) 2D representation from the GUI of the co-polarized electric field amplitude

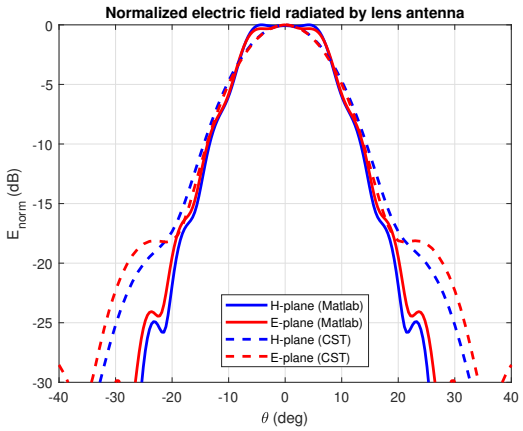

(b) Radiated electric field calculated by the GUI

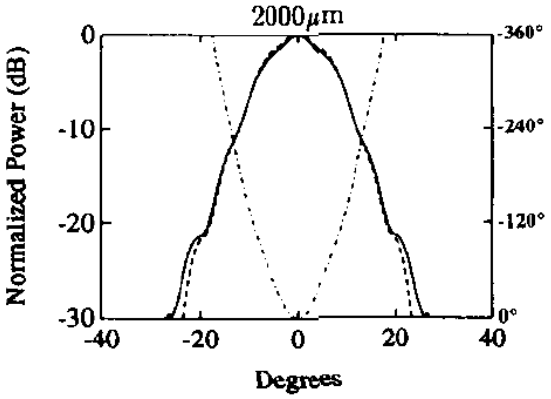

(c) Radiated electric field calculated in [31]

Figure 4.4: Normalized far field of the lens antenna with the double slot as feed

Fig. 4.4 presents the far field from the lens antenna, as they are computed by the GUI tool and by the CST configuration of Fig. 4.2c, using a time domain solver. The far field is shown on the two main planes, $\phi = 0°$ and $\phi = 90°$. The theoretical results are very similar to the results given in [31] and are also quite similar to the results obtained by CST. The difference with CST is probably due to the fact that for computer memory reasons we designed a smaller lens with radius of the hemispherical part $R = 2.5mm$ and extension length $L = R/n$. From Fig. 4.4b we observe that the differences in the CST results are at angles not close to the broadside direction and are for field levels that are less than -17 dB compared to the field level at the broadside. Therefore we can consider that the differences are in an acceptable level and in general we can confirm the accuracy of the Matlab tool and apply it for other feeds as well.

5

Conclusion

5.1. Summary and conclusions

This thesis was an investigation of a THz lens antenna with a PCCA as a feed. The goal of the thesis was twofold; the first part was dedicated to the analysis of the radiation and properties of the feed and the lens antenna and the second part included a feasibility study for the fabrication of this antenna. The design parameters of the feed were already selected in previous work [23].

The theoretical analysis was based on calculating the fields of the feed and the lens antenna in the spectral domain. The feed radiates in a stratification that includes layers of air, resin for the microlenses, GaAs and silicon, which needs to be taken into consideration to formulate the Green's function. Also the equivalent currents along the connected dipole array have been computed according to already known background knowledge found in the literature. The results of the feed radiation show a very directive beam for most of the radiated spectrum of the connected array that illuminates the lens. The secondary field radiated by the lens antenna is found with the aid of a Matlab GUI tool that calculates equivalent currents on the lens surface and subsequently the field radiated by these equivalent currents. The results indicate that for all frequencies from 100GHz up to 5THz the field radiated by the PCCA can be captured by a convergent lens, that will refocus it to the detector.

Regarding the fabrication we investigated some options via some test structures in order to determine whether the accurate fabrication of the desired PCCA, as we theoretically designed it in [23], is feasible. One core component that created some uncertainty over the feasibility was the microlens array that focuses the laser power to the dipole excitation gaps, because in previous work of the group a commercially available microlens array had been selected in the prototype. For this reason, we printed a few test structures and discussed various aspects and issues that can emerge during the 3D printing of the array. The conclusion from our work is that, despite the imperfections of the fabrication, the microlens arrays that we managed to print in the premises of TU Delft meet the accuracy requirements and most of the errors can be compensated through minor changes in the operation.

5.2. Future work

The theoretical background of the thesis was entirely based on [17], which presented the Norton equivalent circuit to model a photoconductive antenna. Although the accuracy of the presented model was experimentally proven by the authors of [17], the model includes some simplifications, for example regarding the frequency dependence of the Norton generator impedance. When working in broadband applications, as it is assumed in the thesis, a more precise model would definitely lead to a better design of the PCCA and achieve more accurate results. We expect, therefore, that if in the TS group we improve the model, the study will be refined before we proceed to the final fabrication of the prototype.

In order to complete the analysis of the PCCA and be able to experimentally verify the results, we need to be able to theoretically estimate the power that reaches the detector. In the experimental configuration, we will characterize the PCCA by measuring the received power and the spectral components of the received signal. In order to estimate the power that is received in the detector, we need to design the QO path of the THz broadband signal and simulate the transmission of the signal through the QO path until the detector.

This will require the utilization of a commercial software, such as GRASP [47], that is capable to simulate large configurations and calculate the fields along QO paths.

The final stage in the future work related to this thesis will be the fabrication of a prototype, which will enable us to experimentally verify the theoretical results and the results obtained by simulations performed by commercial software. During the fabrication we will need to integrate all components of the PCCA, the microlens array, the GaAs layer with the printed connected dipole array pattern and the THz silicon lens. Also, as explained above, we will need to have designed and constructed the whole THz-TDS setup, so that we can perform the measurements, process them and compare them with the expected results. The successful implementation of this antenna will undoubtedly be a breakthrough in the domain of broadband THz antennas and will greatly expand the plans and outlook of the TS group in the PCA research and applications.

5.3. Publications

1. A. Pelekanidis, P. M. Sberna, D. Fan, J. Bueno, N. Llombart and A. Neto, "A connected array of coherent photoconductive pulsed sources to generate mW average power in a 5 THz bandwidth," in *2020 45th Intern. Conf. on Infrared, Millimeter, and Terahertz Waves (IRMMW-THz),* Buffalo NY, USA, to be published.

A

Useful Topics of PCCA Design

A.1. Equations for Norton Circuit

In [17], a Norton equivalent circuit for the PCA is derived, which incorporates the bias voltage and the time variation of the conductance of the photoconductive substrate due to the laser illumination. The equivalent Norton circuit is depicted in Fig. A.1. The equivalent circuit current is given by the expression

$$I_g(\omega) = \eta(W_x, W_y, W_z, A_{laser}) \frac{A_{laser}}{W_y^2} \epsilon\mu H(\omega) \tilde{S}(\omega) V_{bias} \tag{A.1}$$

while the equivalent Norton impedance is

$$Z_g(\omega) \approx \frac{1}{g_0} = \left[\eta(W_x, W_y, W_z, A_{laser}) \frac{A_{laser}}{W_y^2} \epsilon\mu \frac{1}{\tau_\sigma} H(\omega = 0) \tilde{S}(\omega = 0) \right]^{-1} \tag{A.2}$$

where

$$\eta(W_x, W_y, W_z, A_{laser}) = \left(1 - |\Gamma|^2\right) \frac{1 - e^{-\alpha W_z}}{W_z} \frac{1}{A_{laser}} \int_{-W_y/2}^{W_y/2} \int_{-W_x/2}^{W_x/2} \int_{-W_z}^{0} |\tilde{\vec{s}}_n(\vec{\rho}, z = 0)| dz\, dx\, dy$$

$$A_{laser} = \int_{-\infty}^{\infty} \int_{-\infty}^{\infty} |\tilde{\vec{s}}_n(\vec{\rho}, z = 0)| dx\, dy$$

with $\tilde{\vec{s}}_n(\vec{\rho}, z)$ the normalized spatial distribution of the laser pulse

$$H(\omega) = \frac{1}{h f_g} \frac{\tau}{1 + j\tau\omega}$$

$\tilde{S}(\omega)$ is the Fourier transform of the time-varying envelope of the laser pulse

τ_σ is a time interval used for averaging of the conductance.

The efficiency coefficient $\eta(W_x, W_y, W_z, A_{laser})$ consists of 3 terms:

- the reflection efficiency $1 - |\Gamma|^2$, where Γ is the reflection coefficient at the interface between the material in which the laser light propagates and semiconductor. In the current design, this material is a resin, with a relative permittivity $\epsilon_r \approx 2.25$.
- the absorption efficiency $1 - e^{-\alpha W_z}$
- the spillover efficiency $\frac{1}{W_z A_{laser}} \int_{-W_y/2}^{W_y/2} \int_{-W_x/2}^{W_x/2} \int_{-W_z}^{0} |\tilde{\vec{s}}_n(\vec{\rho}, z = 0)| dz\, dx\, dy$

The time interval τ_σ is a reasonable interval during which the average conductivity over space of the photoconductive substrate is practically larger than zero. Throughout this thesis, this interval is assumed to be such that it corresponds to the conductivity being larger than $1/e$ of its maximum value. The expression for the conductivity is

$$\sigma(\vec{r}, t) = e\mu \mathscr{F}^{-1} \left\{ N(\vec{r}, \omega) \right\} \tag{A.3}$$

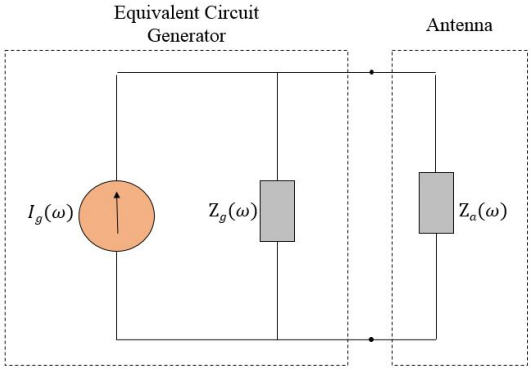

Figure A.1: Equivalent Norton circuit for the photoconductive antenna

where

e is the elementary charge

μ is the carrier mobility

$N(\vec{r},\omega)$ is the Fourier transform of the charge carrier density and is equal to

$$N(\vec{r},\omega) = \left(1-|\Gamma|^2\right)\frac{1-e^{-\alpha W_z}}{W_z}\frac{1}{hf_g}\frac{\tau}{1+j\tau\omega}|\vec{\tilde{s}}_n(\vec{\rho},z=0)|\tilde{S}(\omega)$$

and the average value of $\sigma(\vec{r},t)$ is

$$\sigma(t) = \frac{1}{W_x W_y W_z}\int_{-W_x/2}^{W_x/2}\int_{-W_y/2}^{W_y/2}\int_{-W_z}^{0}\sigma(\vec{r},t)\,dz\,dy\,dx$$

A.2. Connected Dipoles with Width Tapering

In this section we give the expressions for the impedance of connected dipoles whose width has been tapered close to the excitation points Since the antenna utilized in the thesis is an array consisting of connected dipoles, we are interested in calculating the active input impedance in order to investigate matching conditions with the Norton equivalent circuit. The active input impedance is the impedance of one antenna element when all other elements of the array are also excited. If the antenna impedance can be calculated and designed properly in order to conjugate match the source impedance, then we can design the PCCA efficiently and maximize the power that will be generated and radiated into the silicon lens of the PCCA for a given input power.

In the case of infinite arrays, the active input impedance is the same for all elements, whereas in finite structures edge effects influence the impedance of the elements located near the edges. For infinite arrays of connected dipoles with uniform width the active input impedance is known analytically and is given by the following expressions

$$Z_{a,dipole} = d_x\frac{1}{\sum_{m_x=-\infty}^{\infty}\frac{-sinc^2(k_{xm}\delta_d/2)}{D_\infty(k_{xm})}} \tag{A.4}$$

where

$$D_\infty(k_x) = \frac{1}{d_y}\sum_{m_y=-\infty}^{\infty}G_{xx}^{ej}(k_x,k_{ym})J_0\left(\frac{k_{ym}w_d}{2}\right)$$

In Eq. (A.4) it is clear that the analytical formulas give the active input admittance $Y_{a,dipole}$ as a sum of infinite terms, from which we can find the active input impedance as $Z_{a,dipole} = 1/Y_{a,dipole}$. In the above expressions, d_x and d_y are the periodicities of the array in the x and y direction respectively, δ_d is the length of the excitation gap of the dipole, w_d is the width of the dipoles, $k_{xm} = k_{x0} - \frac{2\pi m_x}{d_x} = k_0\sin\theta\cos\phi - \frac{2\pi m_x}{d_x}$

and $k_{ym} = k_{x0} - \frac{2\pi m_y}{d_y} = k_0 \sin\theta \sin\phi - \frac{2\pi m_y}{d_y}$ are the Floquet modes, $G(k_x, k_y)$ is the spectral Green's function and $J_0(ky)$ is the zeroth order Bessel function. The expression in Eq. A.4 is valid when the large dimension of the element is along x and the small dimension along y, so the equivalent current is assumed to flow along x and have an edge-singular distribution along the y direction. The selected dipoles' orientation for which the above expressions are valid is different from the coordinate system presented in Fig. 1.4 which shows the dipoles to extend along the y direction ; however, the results for the active input impedance are not affected, since we radiate in the broadside direction.

The spectral Green's function is the same as the function given in Eq. B.1, which takes into account the stratification of the PCCA structure, as it is shown in Fig. 1.4b. For the calculation of the impedance only the xx component of the expression in B.1 is required.

Note that these expressions are valid only when the width of the dipole w_d is uniform, whereas the connected dipoles we have used are tapered close to the excitation gaps. This tapering creates a crowding of the equivalent electric current, which leads to strong reactive energy at the transition [48]. This reactive energy can be included in the theoretical model as inductors and capacitors placed in series and in parallel respectively to the initially computed active input impedance. We assume that the reactive energy is localized to the tapered area and the excitation gap of each connected dipole and therefore does not affect the input impedance of the other array elements. The value of the impedance of the series inductance is, according to [48],

$$Z_s = Z(t_2) - Z(t_1)$$

where

$$Z(t_i) = k_0 L[Z_a(t_i) + Z_b(t_i)]$$

and

$$Z_a(t_i) = \frac{j\pi\zeta_0}{2t_i^2\left(k_1^2 - k_2^2\right)}\left\{\frac{H_0^2(k_2 t_i) - J_0(k_2 t_i}{-j} - \frac{H_0^2(k_1 t_i) - J_0(k_1 t_i}{-j} + \frac{2}{\pi} ln\Big(\frac{k_1}{k_2}\Big)\right\}$$

$$Z_b(t_i) = \frac{\pi\zeta_0}{2}\left\{\frac{j}{2}\Big[-\frac{2}{\pi} ln(\gamma' t_i) + \frac{3}{\pi}\Big] - \frac{j\Big[k_1^2 ln\Big(\frac{k_1}{k_2}\Big) - k_2^2 ln\Big(\frac{k_1}{k_2}\Big)\Big]}{\pi\left(k_1^2 - k_2^2\right)}\right\}$$

with t_1 and t_2 the widths of the conductors before and after the transition respectively. Accordingly, the value of the impedance of the parallel capacitance is given by the expression

$$Z_p = \frac{1}{Y_p}$$

where

$$Y_p = Y(L_2) - Y(L_1)$$

and

$$Y(L_i) = -\frac{j t k_0 \epsilon_1}{\pi\zeta_0}\Big[ln\Big(\gamma'\frac{k_1}{2}L_1\Big) - \frac{3}{2}\Big] - \frac{j t k_0 \epsilon_2}{\pi\zeta_0}\Big[ln\Big(\gamma'\frac{k_2}{2}L_2\Big) - \frac{3}{2}\Big]$$

with L_1 and L_2 the lengths of the excitation gaps before and after the transition respectively. The rest of the quantities in the above expressions can be found in [48].

The tapering of the connected arrays in the proximity of the excitation gaps is continuous, thus the expressions that describe the transitions cannot be applied directly. However, we can approximate the continuous tapering with a number of discrete steps, as shown in Fig. A.2. The "staircase" geometry in Fig. A.2 corresponds to a number of series and parallel reactances added alternately as correction terms to the initially calculated input impedance. The process is described graphically in Fig. A.3. The series inductance is added to the model to express the crowding of the electric field lines into a smaller area (Fig. A.3b and d). Correspondingly, the parallel capacitances account for the stronger reactive energy that is stored when the plates are placed closer (Fig. A.3c and e).

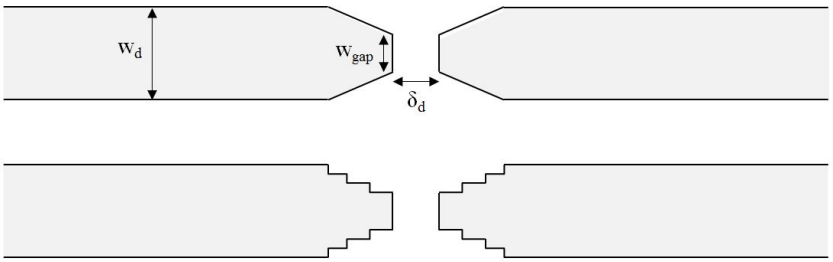

Figure A.2: Discretization of the continuous tapering of the connected dipoles

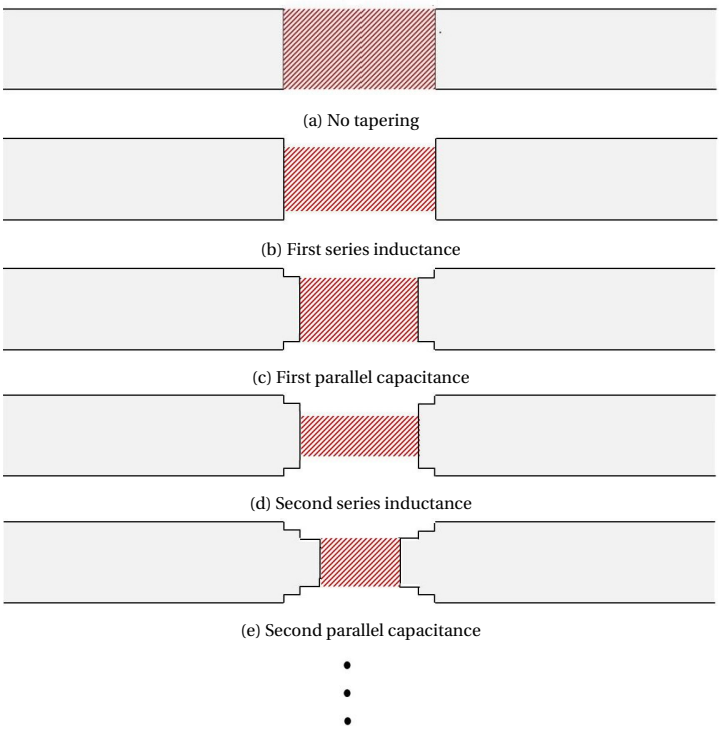

Figure A.3: Space occupied (red striped lines) by the electric field lines at the excitation gap of a dipole when applying the series inductances and parallel capacitances to express the effect of the tapering

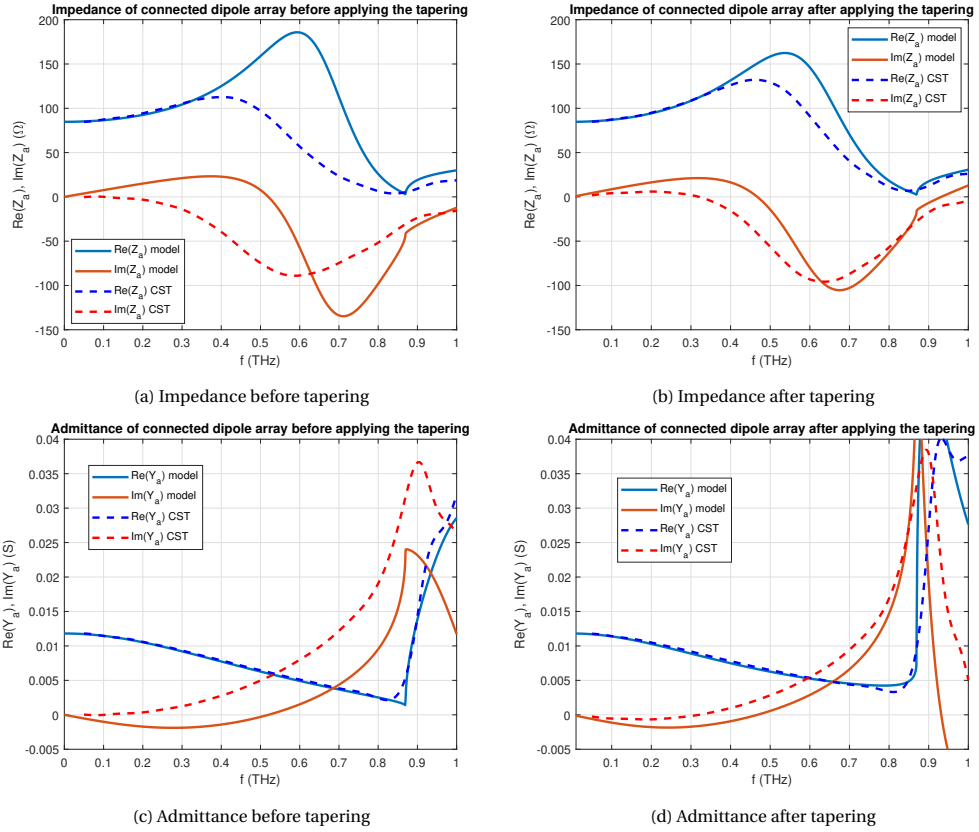

(a) Impedance before tapering

(b) Impedance after tapering

(c) Admittance before tapering

(d) Admittance after tapering

Figure A.4: Impedance and admittance of connected dipole array for the dimensions of the PCCAs defined in [25]. The characterization "before tapering" indicates that the excitation gap is as large as in Fig. A.3a. This gap is set equal to $3w_{gap} = 22.5\mu$m.

Our analysis is based on the theoretical approximation of infinite arrays described above and the results are validated via simulations in CST. Details of the design of the configuration in CST are not given for reasons of conciseness, but they are included in [23]. The active input impedance and admittance for a connected dipole array are given in Fig. A.4. In each subfigure the theoretical results derived by the model and the simulation results of CST are compared. We can remark that the active input impedance of the connected dipole before applying the tapering is quite different when calculated with the theoretical method and when computed by CST (Fig. A.4a). This difference in both the real and imaginary part of the impedance can be explained when we look at the respective admittance (Fig. A.4c). We observe that the real part of the admittance, which is calculated theoretically by the zeroth order Floquet mode in Eq. (A.4), is very close to the real part of the admittance derived by the simulation. On the other hand, there is a large deviation on the values of the imaginary part of the admittance, which comes from the higher order Floquet modes. This deviation emerges probably from the edge-singular basis function that we have assumed for the equivalent current distribution along y, given the coordinate system used in Eq. A.4. Furthermore, after applying the tapering correction, the imaginary part of the admittance tends to be similar in the two approaches, especially in the low frequencies, while the real part remains as accurate as before the tapering was applied (Fig. A.4d). This convergence of the admittances by the two methods has an effect on the calculation of the impedance, which is also quite similar for the theoretical model and the CST. Lastly, the results in Fig. A.4 are in accordance with the results shown in [25], which also includes simulation results for a connected dipole array of the same dimensions.

A.3. Energy Spectrum and Power from a PCCA

This section gives the expressions for the computations of the generated energy spectral density and power by the PCCA, once we have calculated the Norton source impedance, the Norton current and the active input impedance of the array elements. First of all, the expression for the energy spectral density generated

by a single element is, according to [17],

$$E_{s,element}(\omega) = Z_a(\omega)\left|\frac{Z_g(\omega)}{Z_a(\omega)+Z_g(\omega)}\right|^2 |I_g(\omega)|^2$$

This expression for the generated energy spectral density comes directly from the Norton equivalent current of Fig. A.1. For the array, the total energy spectral density is the sum of the energy spectral densities of each array element individually, as mentioned in [25], thus,

$$E_s(\omega) = \sum_{n_y=-\frac{N_y-1}{2}}^{\frac{N_y-1}{2}} \sum_{n_x=-\frac{N_x-1}{2}}^{\frac{N_x-1}{2}} E^{act}_{s_{n_y,n_x}}(\omega) = \sum_{n_y=-\frac{N_y-1}{2}}^{\frac{N_y-1}{2}} \sum_{n_x=-\frac{N_x-1}{2}}^{\frac{N_x-1}{2}} Z_{a_{n_y,n_x}}(\omega)\left|\frac{Z_{g_{n_y,n_x}}(\omega)}{Z_{a_{n_y,n_x}}(\omega)+Z_{g_{n_y,n_x}}(\omega)}\right|^2 |I_{g_{n_y,n_x}}(\omega)|^2 \tag{A.5}$$

If we assume that the active input impedance of all antenna elements is equal to the active input impedance of an antenna element at an infinite array, $Z_{a_{n_y,n_x}}(\omega) = Z_a(\omega)$ for all n_x, n_y in Eq. (A.5); however if we consider the finiteness of the structure and the impact on the active input impedance, then each element will have a different impedance. Similarly, the source impedance and the equivalent current along each excitation gap will be the same if we assume that the laser power exciting the connected dipoles is uniform, but in fact they will be different, because of the spatial power distribution of the laser, which causes an inhomogeneous illumination of the dipole gaps.

The total energy generated by the antenna array is, according to [17], the integration of the energy spectral density over all frequencies,

$$E_{source} = \frac{1}{2\pi}\int_{-\infty}^{\infty} E_s(\omega)\, d\omega \tag{A.6}$$

Finally, we can compute the average power generated if we know the repetition rate of the laser source f_p

$$\bar{P}_{source} = E_{source}\cdot f_p = \frac{E_{source}}{T_p}$$

where $T_p = \frac{1}{f_p}$ is the period of the laser source.

A.4. PCCA Design

This section summarizes the procedure that was followed in [23] for the selection of the design parameters of the PCCA.

A.4.1. Dipole and array design

A parametric analysis was conducted for the determination of a desirable active input impedance. At

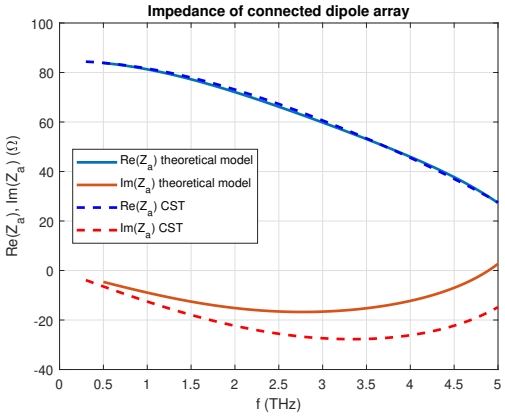

(a) Without microlenses layer included

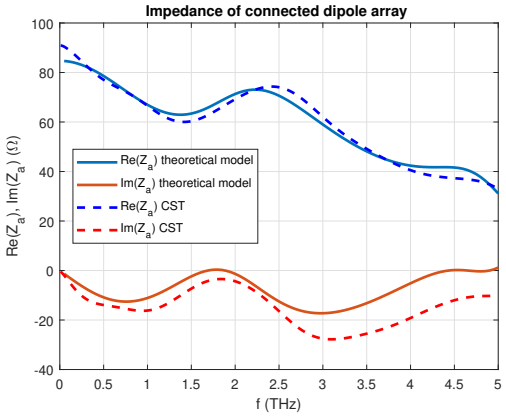

(b) With microlenses layer included

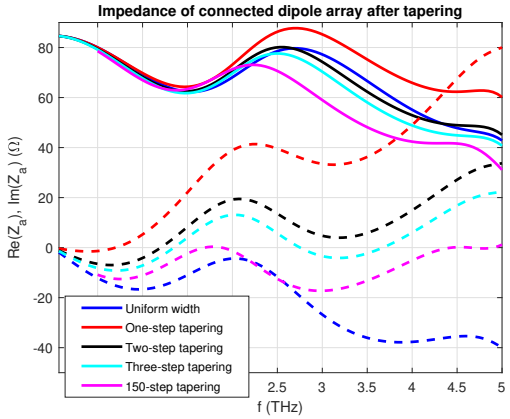

(c) With microlenses layer included for various discretization steps of the tapering. The solid lines show the real part and the dashed lines the imaginary part of the impedances.

Figure A.5: Active input impedance of connected dipole array for $W_{dipole} = 8\,\mu$m, $d_{period} = 15\,\mu$m and angle of tapering $a = 109°$

this stage the connected dipole was assumed to be located at the interface between air and the GaAs substrate, because the final structure of the PCCA was not known, but it was shown later in [23], that including the layer of the microlenses' resin on top of the connected dipoles does not alter significantly the active input impedance. The excitation gap of each dipole has been chosen to have a fixed size of $1 \times 1\,\mu$m. Such a small excitation gap results in a desirable source impedance with low laser power. This is a nice feature for the array, considering that we would like to create a very directive array with many elements in both planar directions x and y, which implies that only a small fraction of the total laser power will impinge on each excitation gap.

The parametric analysis concerned the width of the dipoles and the length of the tapering. The periodicity of the array was selected at 15 μm, so that there is radiation of the array without grating lobes for frequencies up to 5.8 THz, when scanning at broadside direction. The dimensions where chosen with the criterion that the active input impedance should be constant for a wide frequency range. This investigation yielded the results that are presented in the caption of Fig. A.5.

The resin layer is a part of the microlens array. The permittivity of the material is $\epsilon_{r,resin} = 2.25$ and the thickness of this layer has been computed in [23] as $h_{resin} = 31.773\,\mu m$. In fact, this thickness is not uniform over the whole array, since the microlenses have an arc-shape that creates non-uniformity in the thickness; however, this approximation simplifies the calculation of the active input impedance without introducing large errors. The active input impedance under this condition is presented in Fig. A.5b. Fig. A.5c complements the plots of the active input impedance by showing how the "staircase" geometry described in Appendix A.2 for modeling the tapering changes the values of the active input impedance. Specifically, Fig. A.5c presents the active input impedace for different numbers of discretization steps and if no tapering is applied whatsoever. By comparing Fig. A.5b and A.5c, we observe how adding more discretization steps and making the transition from W_{dipole} to W_{gap} smoother leads to a better convergence of the theoretical results with those from CST.

A.4.2. Microlens array design

Previously, we considered the layer of the resin to have a certain thickness, but we did not explain how this value was derived. It has been a part of the microlens array design. The microlenses focus the laser beam on the gaps. They have an elliptical shape and, as mentioned previously, are made of a resin with permittivity $\epsilon_{r,resin} = 2.25$. We already know and expect from [49] that the received electric field at the focal plane will have an Airy pattern. The difference with [49] is that an optimal microlens design for the PCCA is one with square lenses as shown in Fig. 3.1, which means essentially that the rim angle is not constant with the azimuthal angle. As it will be proven below, the consideration of square lenses transforms the Airy pattern that is due to a bessel function to a $sinc$ pattern.

The microlenses shall be designed in such a way that the -3 dB diameter of the main lobe is equal to the excitation gap of the connected dipoles, $d_{laser}^{-3dB} = w_{gap} = 1\mu m$. The design parameter for the microlenses is the f-number $f_\# = R/D$ of the elliptical lens, where R is the distance of the tip of the lens from the focal point, as indicated in Fig. A.6 and D is the length of the chord that corresponds to the arc of the ellipse that is illuminated by the laser. The rest of the lens parameters are either fixed or determined by the $f_\#$. Each microlens has the structure of Fig. A.6. Due to the square geometry, both R and the length of the chord D are functions of the azimuthal angle ϕ. Specifically D ranges between $d_{period} = 15\mu m$ and $d_{period}\sqrt{2}$, as it can be observed in Fig. 3.1; however, for simplicity we can consider it constant and equal to $D = d_{period} = 15\mu m$. Similarly, we assume the distance $R(\phi)$ to be constant and equal to $R(\phi = 0)$. From the geometry of the ellipse, we can also derive the values for the eccentricity, the major and minor axes, the focal distance and the rim angle. The expressions for these parameters are given in [23] for the interested reader.

The electric field in the focal plane of the ellipse can be found via a FO approach, similar to [49], but for a square geometry,

$$\vec{e}_f(x_f, y_f) \approx \frac{1}{4\pi^2} e^{-jk\frac{x_f^2+y_f^2}{2R}} \int_{-\infty}^{\infty}\int_{-\infty}^{\infty} \vec{E}_f(k_x, k_y) rect(k_x, 2k\cdot sin\theta_0) rect(k_y, 2k\cdot sin\theta_0) e^{jk_x x_f} e^{jk_y y_f} dk_x dk_y$$

where

$$\vec{E}_f(k_x, k_y) = \frac{j2\pi\vec{E}_0^{PW} e^{-jkR}}{k_z} \frac{c(1-e^2)}{e(1-ecos\theta)} \cdot \left(\tau_{||}(\theta)\frac{k_x}{k_\rho}\hat{\theta} - \tau_\perp(\theta)\frac{k_y}{k_\rho}\hat{\phi}\right) \Rightarrow$$
$$E_f(k_x, k_y) \approx \frac{j2\pi E_0^{PW} e^{-jkR}}{k} \frac{c(1+e)}{e}\tau_{||}(0),$$

when the incident field is linearly polarized along x with amplitude E_0^{PW} and after doing some approximations. The electric field is, then, equal to

$$e_{xf}(x_f, y_f) \approx \frac{1}{2\pi} \frac{jE_0^{PW} e^{-jkR}}{k} \frac{c(1+e)}{e}\tau_{||}(0) 2k\cdot sin\theta_0 \cdot sinc\left(\frac{kD}{2R}x\right) \cdot 2k\cdot sin\theta_0 \cdot sinc\left(\frac{kD}{2R}y\right)$$

It is important to note that the above expressions for the electric field according to the FO approach has an applicability region that ensures an amplitude error of smaller that 20% and phase error smaller than $\frac{\pi}{8}$. The applicability region is of diameter

$$Diam_{FO} = f_\# \min(0.4D, \sqrt{2f_\# D\lambda})$$

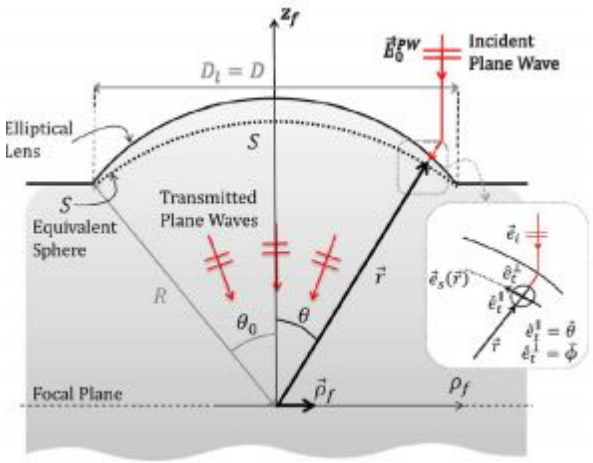

Figure A.6: Structure of a single microlens [18, p. 577]

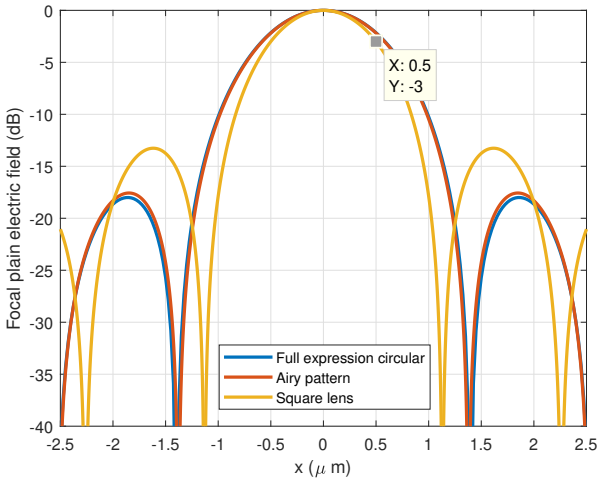

Figure A.7: Normalized electric field in the focal plane for $y_f = 0$, when the focal distance is $f = 34.393\mu m$. The field for the square lens geometry (in yellow) is compared to the field that would yield for a circular lens geometry (blue and red lines).

The focal distance of the lens that gives a beam whose main lobe has a -3 dB diameter equal to 1 μm has been found to be equal to 34.393 μm. The applicability region for this choice of dimensions is $Diam_{FO} = 13.71\,\mu m$, so the result for the electric field at the gap is valid. The electric field is presented in Fig. A.7.

According to the geometry of the lens presented in Fig. A.6, the thickness of the resin layer is equal to $h_{resin} = R \cdot cos\theta_0 = 31.773\mu m$, which is the value used before at the expressions for the calculation of the active input impedance.

A.4.3. PCCA Radiation

After having determined the active input impedance of the array elements and the design parameters for the microlenses array, we can simulate the whole PCCA structure. Initially, we need to express the laser that impinges on the PCCA. We assume a spatial distribution of a Gaussian-shaped pulse that impinges with an average laser power of $P_{ave,total} = 250mW$, which is the maximum available average laser power in our setup in the THz lab of TU Delft. The number of elements and consequently the size of the array will be computed via a parametric analysis, in which the radiated power is estimated as a function of the array size. The results of this parametric analysis are presented in Fig. A.8. The bias electric field assumed is 10.67 V/μm, as is the maximum bias electric field used in [25]. This ensures that the bias voltage will not cause breakdown of the semiconductor or the air.

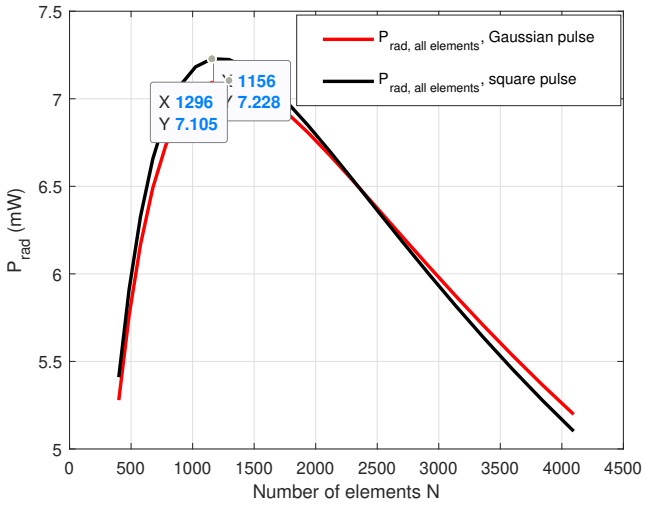

Figure A.8: Radiated power as a function of the number of elements in the square array, when the laser power is $P_{ave,total} = 250mW$.

Fig. A.8 compares the estimated radiated power for two laser spatial distributions, Gaussian and uniform distribution. For the Gaussian laser pulse, it turns out that the array should optimally consist of $N = 1296$ elements. Given a square array, the number of elements along x, N_x should be equal to the number of elements along y, N_y, so

$$N_x = N_y = \sqrt{N} \Rightarrow N_x = N_y = 36$$

For an array with period $d_{period} = 15\mu$m, the array size is $L_x \times L_y = (N_x \cdot d_{period}) \times (N_y \cdot d_{period}) = 540\,\mu m \times 540\,\mu m$. The -3 dB diameter of the Gaussian beam is $D_{laser} = L_x = L_y = 540\,\mu$m. With all design parameters determined, the PCCA has the structure of Fig. 2.1.

As mentioned before, the laser pulse propagates through the microlens array that focuses the laser power on the excitation gaps of the connected dipole array elements. Since the spatial distribution of the power is Gaussian and not homogeneous, the average power that impinges on each excitation gap will be different. Due to the symmetry of the Gaussian beam along both $x'x$ and $y'y$ axis, it is sufficient to calculate the average power only for the gaps in one quarter of the array.

As an example, we will consider a typical value for the bias voltage, according to [25], $V_{bias} = 10.67$ V per unit cell, which corresponds to an electric field $E_{bias}^{cell} = 10.67V/\mu m$, same as what was used for the results of Fig. A.8. The total bias voltage is, therefore, 384 V. The equivalent Norton impedance Z_g of the 18×18 elements in the first quarter of the array is given in Table A.1. The gaps at the edges of the array have high resistance (and consequently low conductance), because the average power that impinges on them, which is proportional to the conductance, is low. Accordingly, the resistance at the centre of the array is low, because the laser power density has the maximum value. We observe that the central elements achieve a good match with the active input impedance of the connected dipoles, shown in Fig. A.5b, over a large frequency band.

The radiated power by this configuration is calculated as $P_{rad} = 7.1mW$. Note that the power has been computed as described in Appendix A.3, but at the integration of Eq. A.6 we have excluded the low frequencies $|f| < 0.1$ THz, as for these frequencies the finiteness of the array is significant and due to the presence of edge effects the theoretical results are not accurate.

Fig. A.9 shows the generated energy spectral density for the above selected values of laser power, bias voltage, array dimensions and dipole dimensions. The results are compared to the previous work performed in the group and mentioned in [25]. From the comparison we can conclude that the performance of our array is very satisfying, given that the laser power we have assumed is only 250 mW, which is half of the laser power used in [25].

x/y	1	2	3	⋯	6	⋯	9	⋯	12	⋯	15	16	17	18
1	198	184	172		144		125		113		106	104	103	103
2	184	171	160		134		116		105		98.2	96.9	96.1	95.7
3	172	160	149		125		108		97.7		91.7	90.5	89.7	89.3
⋮														
6	144	134	125		104		90.5		81.7		75.6	75.6	75	74.6
⋮														
9	125	116	108		90.5		78.6		70.9		66.5	65.7	65.1	64.8
⋮														
12	113	105	97.7		81.7		70.9		64		60	59.2	58.7	58.5
⋮														
15	106	98.2	91.7		76.6		66.5		71.1		56.3	55.6	55.1	54.9
16	104	96.9	90.5		75.6		65.7		59.2		55.6	54.9	54.4	54.2
17	103	96.1	89.7		75		65		58.7		55.1	54.4	53.9	53.7
18	103	95.7	89.3		74.6		64.8		58.5		54.9	54.2	53.7	53.5

Table A.1: Norton equivalent source impedances (in Ω) of the excitation gaps that are located in the first quarter of the array

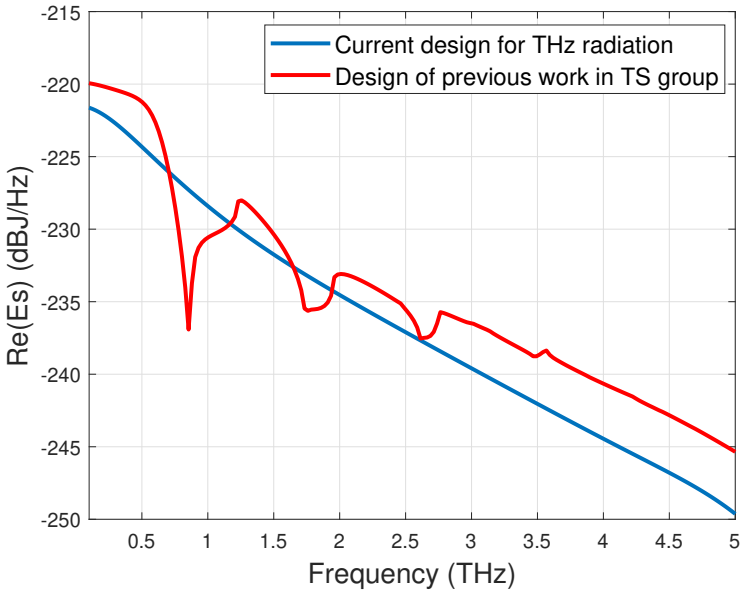

Figure A.9: Generated energy spectral density by the PCCA, compared to the results in [25] for the same bias electric field.

B

Spectral Green's Function for the PCCA Stratification

The silicon layer at the bottom half-space and the air layer at the top half-space are considered infinite. Therefore, the spectral Green's function, which has been used for the calculation of the radiated far field from the PCCA in Section 2, as well as in [23] for the derivation of the active input impedance, is

$$\tilde{G}^{ej} = \begin{bmatrix} -\frac{v_{TM}k_x^2 + v_{TE}k_y^2}{k_\rho^2} & \frac{(v_{TE}-v_{TM})k_x k_y}{k_\rho^2} \\ \frac{(v_{TE}-v_{TM})k_x k_y}{k_\rho^2} & -\frac{v_{TE}k_x^2 + v_{TM}k_y^2}{k_\rho^2} \\ \zeta \frac{k_x}{k} i_{TM} & \zeta \frac{k_y}{k} i_{TM} \end{bmatrix} \tag{B.1}$$

with

$$v_{TE} = Z_{TE} \cdot e^{-jk_z^{Si}z} = \frac{Z_{TE}^{up} Z_{TE}^{down}}{Z_{TE}^{up} + Z_{TE}^{down}} \cdot e^{-jk_z^{Si}z} \tag{B.2}$$

$$v_{TM} = Z_{TM} \cdot e^{-jk_z^{Si}z} = \frac{Z_{TM}^{up} Z_{TM}^{down}}{Z_{TM}^{up} + Z_{TM}^{down}} \cdot e^{-jk_z^{Si}z} \tag{B.3}$$

$$\begin{aligned} i_{TE} &= \frac{Z_{TE}}{Z_{TE}^{Si}} \cdot e^{-jk_z^{Si}z} \\ i_{TM} &= \frac{Z_{TM}}{Z_{TM}^{Si}} \cdot e^{-jk_z^{Si}z} \end{aligned} \tag{B.4}$$

$$
\begin{aligned}
Z_{TE}^{up} &= Z_{TE}^{resin}\frac{Z_{TE}^{0}+jZ_{TE}^{resin}\,tan(k_z^{resin}h_{resin})}{Z_{TE}^{resin}+jZ_{TE}^{0}\,tan(k_z^{resin}h_{resin})}\\
Z_{TM}^{up} &= Z_{TM}^{resin}\frac{Z_{TM}^{0}+jZ_{TM}^{resin}\,tan(k_z^{resin}h_{resin})}{Z_{TM}^{resin}+jZ_{TM}^{0}\,tan(k_z^{resin}h_{resin})}\\
Z_{TE}^{down} &= Z_{TE}^{GaAs}\frac{Z_{TE}^{Si}+jZ_{TE}^{GaAs}\,tan(k_z^{GaAs}h_{GaAs})}{Z_{TE}^{GaAs}+jZ_{TE}^{Si}\,tan(k_z^{GaAs}h_{GaAs})}\\
Z_{TM}^{down} &= Z_{TM}^{GaAs}\frac{Z_{TM}^{Si}+jZ_{TM}^{GaAs}\,tan(k_z^{GaAs}h_{GaAs})}{Z_{TM}^{GaAs}+jZ_{TM}^{Si}\,tan(k_z^{GaAs}h_{GaAs})}\\
k_z^X &= -j\sqrt{-\left((k_0\sqrt{\epsilon_{r,X}})^2-k_\rho^2\right)}\\
Z_{TE}^X &= \frac{120\pi}{\sqrt{\epsilon_{r,X}}}\frac{k_z^X}{k_0\sqrt{\epsilon_{r,X}}}\\
Z_{TM}^X &= \frac{120\pi}{\sqrt{\epsilon_{r,X}}}\frac{k_0\sqrt{\epsilon_{r,X}}}{k_z^X}\\
k_\rho^2 &= k_x^2+k_y^2
\end{aligned}
$$

For the calculation of the far field to an observation point at distance $\vec{r}$ radiated by the PCCA, the values for k_x and k_y are

$$
\begin{aligned}
k_x &= k_d\,sin\theta cos\phi\\
k_y &= k_d\,sin\theta sin\phi
\end{aligned}
$$

where θ and ϕ are the stationary phase points, and

$$z = r\,cos\theta$$

For the calculation of the active input impedance, assuming an infinite array, k_x and k_y take discrete values, the Floquet modes,

$$
\begin{aligned}
k_{xm} &= -2\pi m_x d_x\\
k_{ym} &= -2\pi m_y d_y
\end{aligned}
$$

where m_x, m_y are from $-\infty$ to $+\infty$ and d_x, d_y are the periodicities along x and y. The value for z is taken equal to 0 in this case.

Finally, when computing the spectrum of the current along the connected dipoles in Eq. 2.2, the spectral Green's function is called at the function $D_l(k_x)$. In this case, we assume infinite array along y and finiteness along x, so k_y takes the values of the Floquet modes and $k_x = k_d\,sin\theta cos\phi$, where θ and ϕ are the stationary phase points.

C

Fabricated Microlenses in the 4 × 4 Configuration

The fabricated microlenses test structure is has some imperfections that occur during the 3D printing with Nanoscribe and the 2PP process. These imperfections can be approximated by a defocusing term, as explained in Section 3. In this section we present the results of our attempt to fit the measured data to a displaced ellipse as well as the aberrated fields that have been calculated as a result of the estimated defocusing.

C.1. Fitting of displaced ellipse to measurements

In Figs. C.2 to C.17 we show how the measured microlens profiles across horizontal, vertical and diagonal lines passing through the center of each element deviate from the ideal elliptical shape that was given as input to Nanoscribe, as well as how the inclusion of an axial displacement of the ellipse leads to a better fitting of the fabricated structures. The numbering of the elements is according to Fig. C.1. The errors of the fabricated profiles with respect to the displaced ellipse for each element and each measurement have the statistical properties given in Table 3.1.

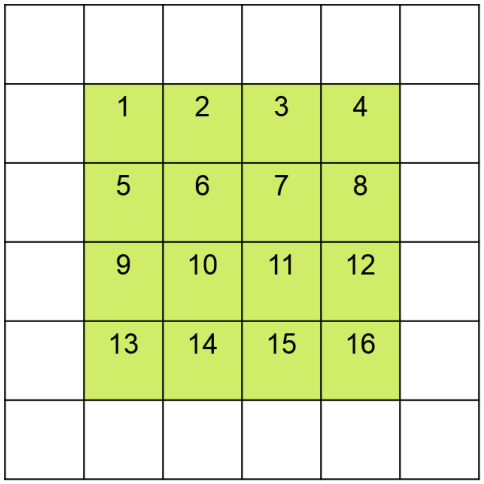

Figure C.1: Numbering of the 4×4 elements within the 6×6 fabricated structure

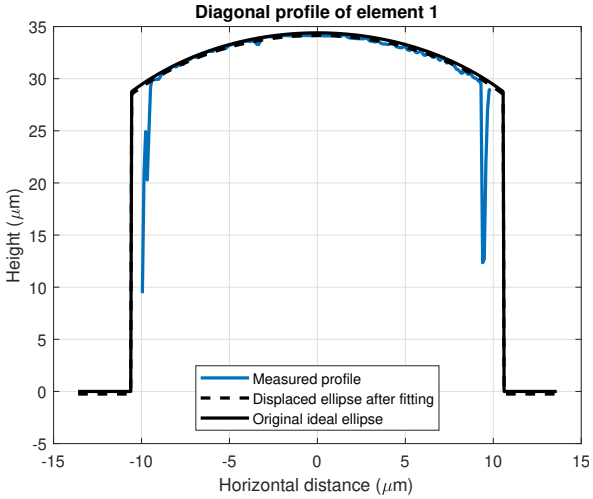

(a) Entire height range

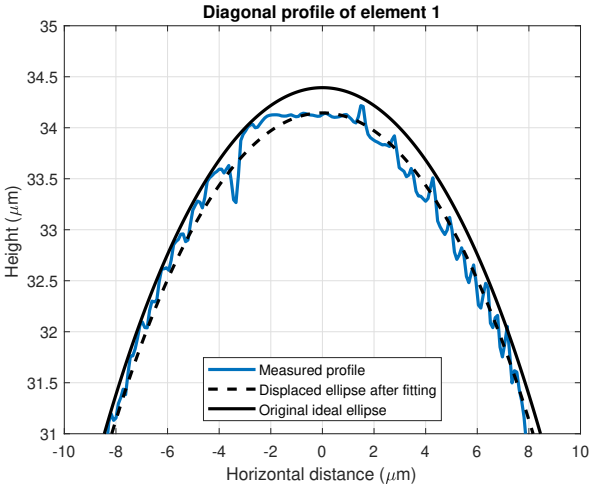

(b) Zoom at the elliptical part of the lens

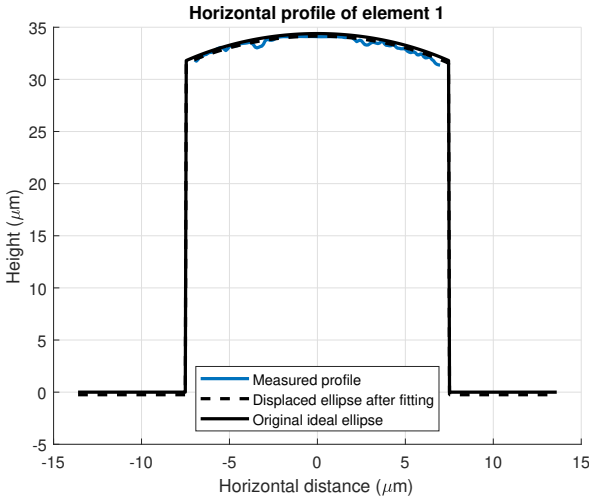

(c) Entire height range

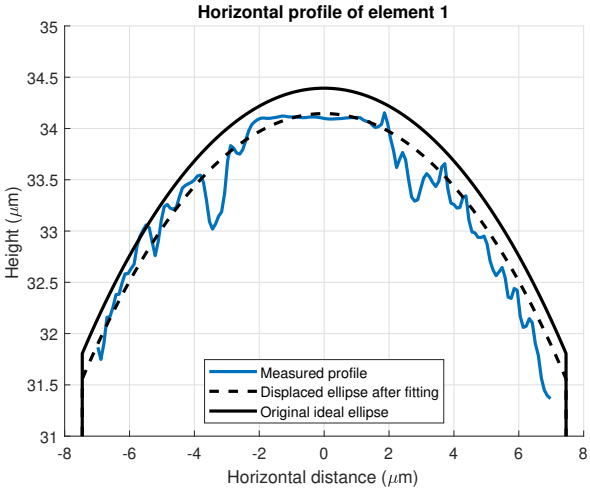

(d) Zoom at the elliptical part of the lens

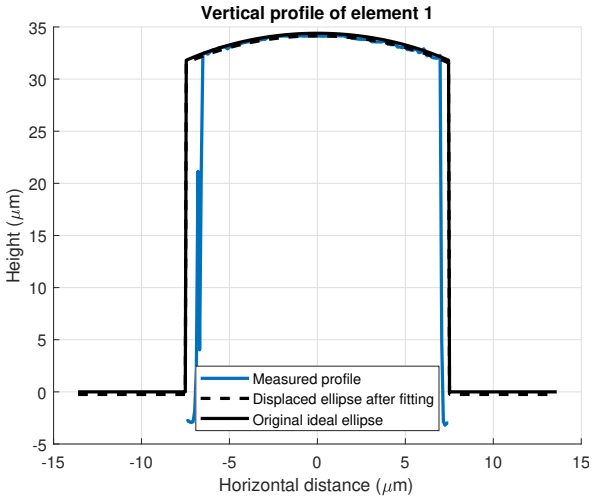

(e) Entire height range

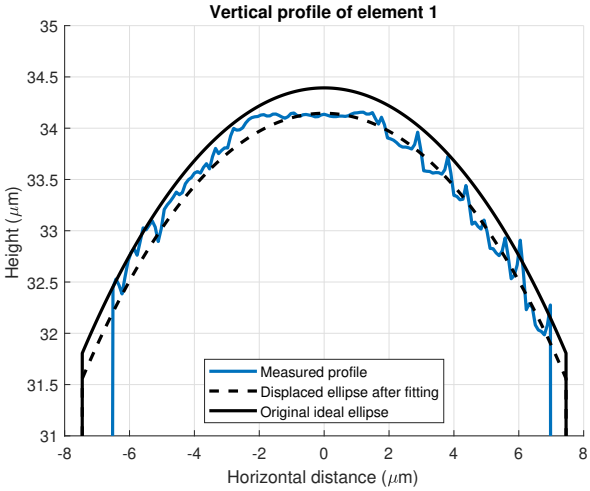

(f) Zoom at the elliptical part of the lens

Figure C.2: Element 1

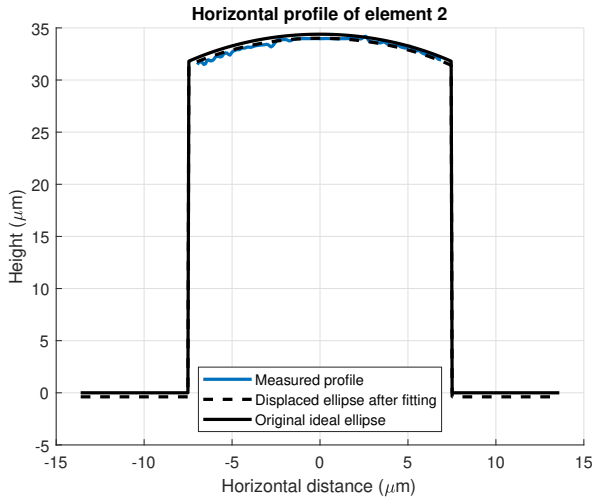

(a) Entire height range

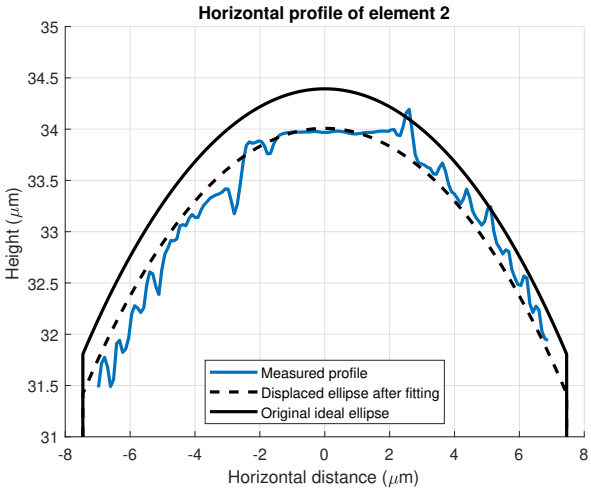

(b) Zoom at the elliptical part of the lens

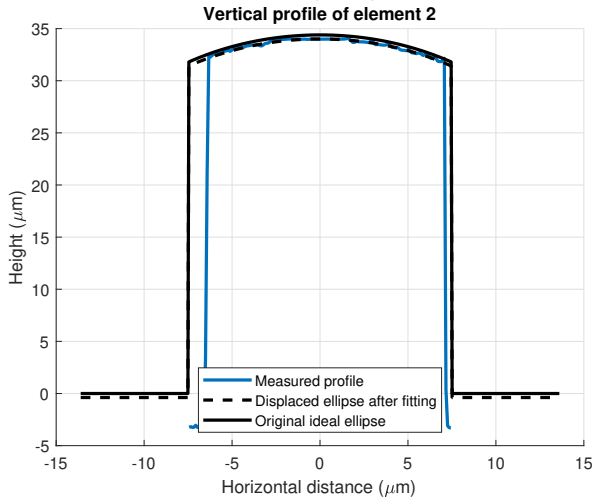

(c) Entire height range

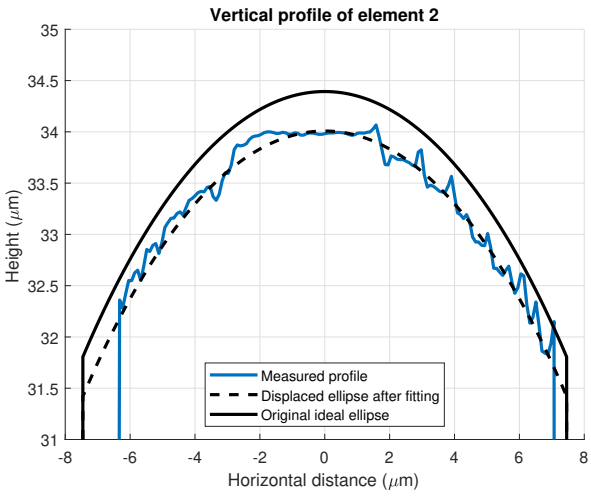

(d) Zoom at the elliptical part of the lens

Figure C.3: Element 2

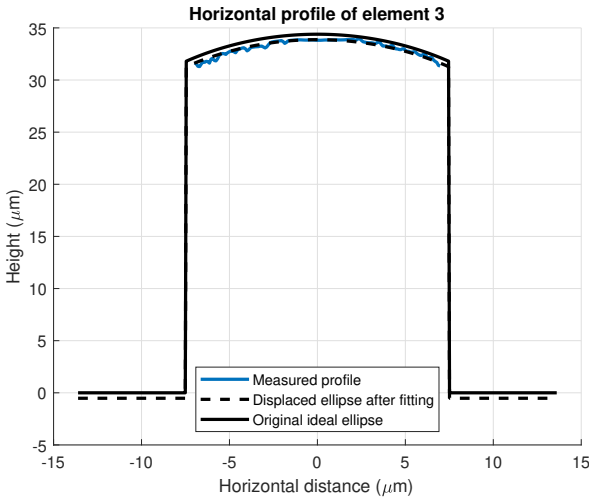

(a) Entire height range

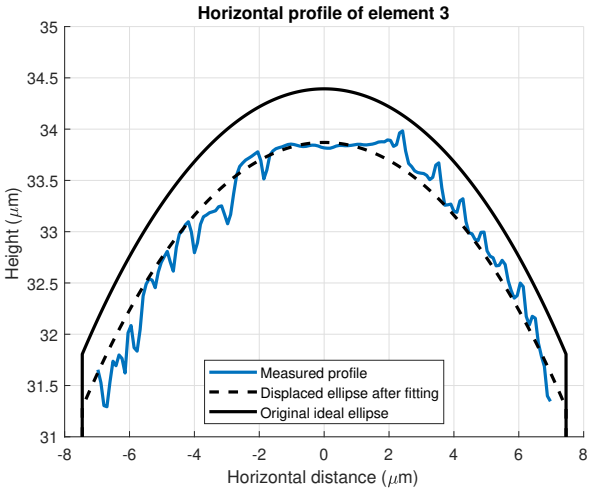

(b) Zoom at the elliptical part of the lens

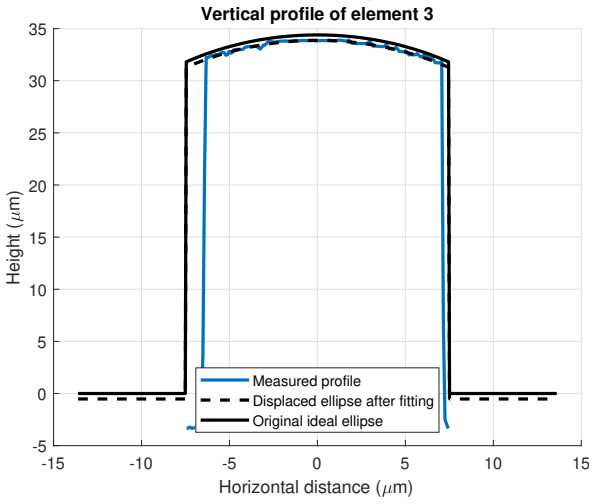

(c) Entire height range

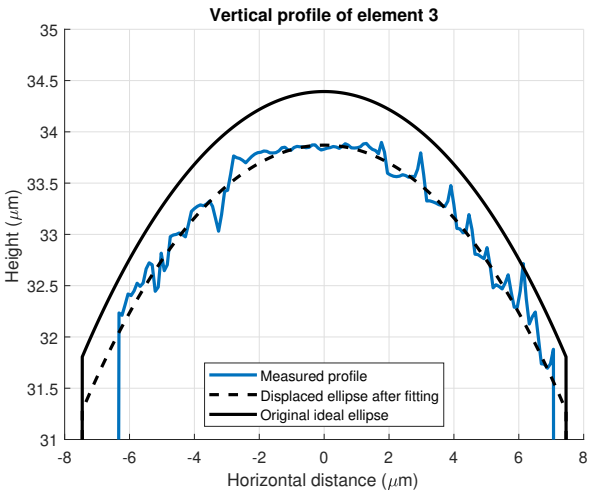

(d) Zoom at the elliptical part of the lens

Figure C.4: Element 3

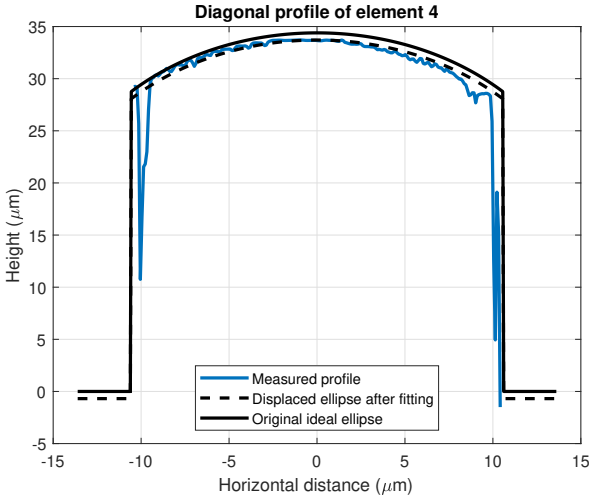

(a) Entire height range

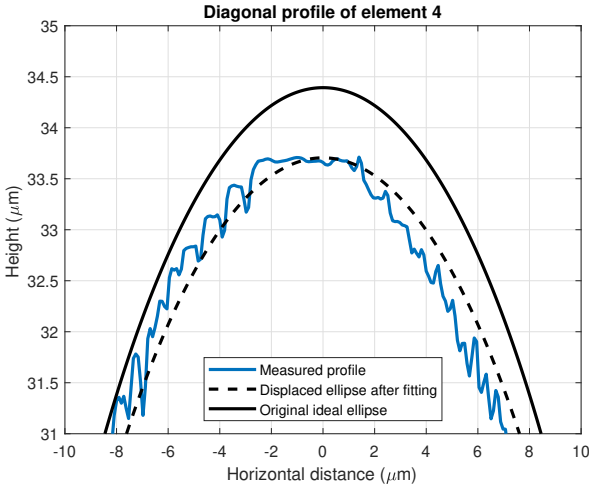

(b) Zoom at the elliptical part of the lens

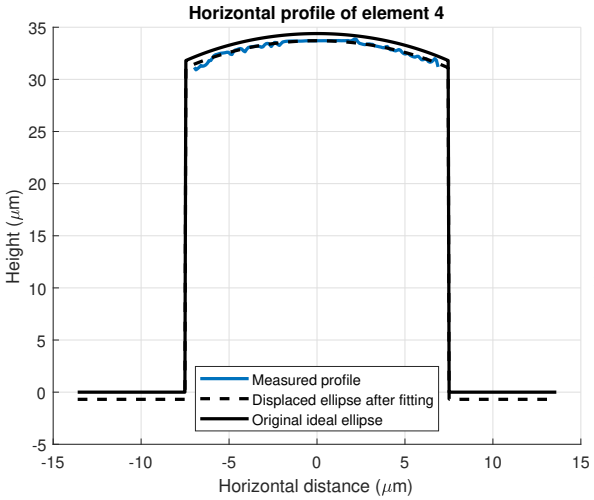

(c) Entire height range

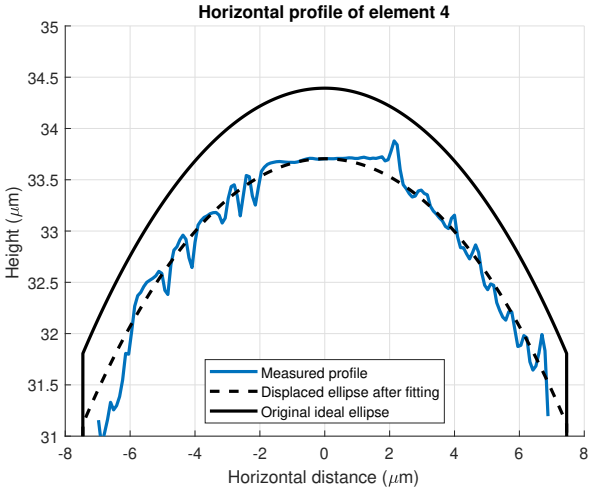

(d) Zoom at the elliptical part of the lens

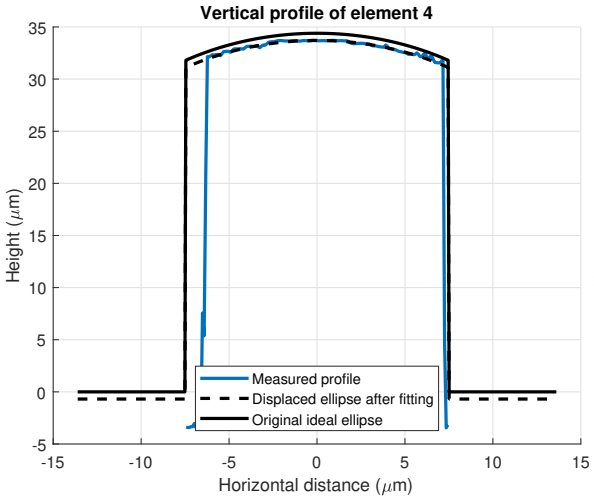

(e) Entire height range

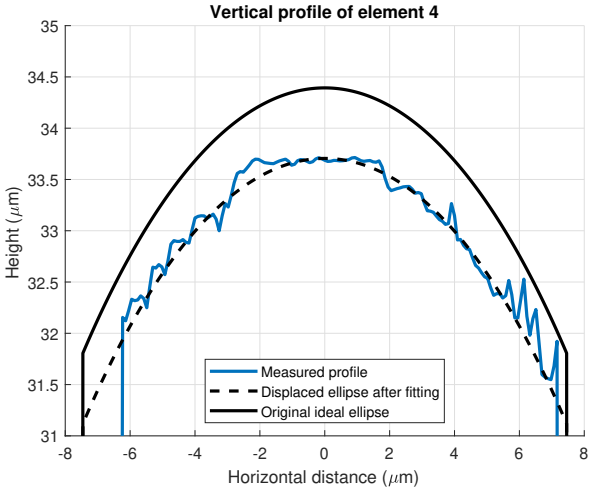

(f) Zoom at the elliptical part of the lens

Figure C.5: Element 4

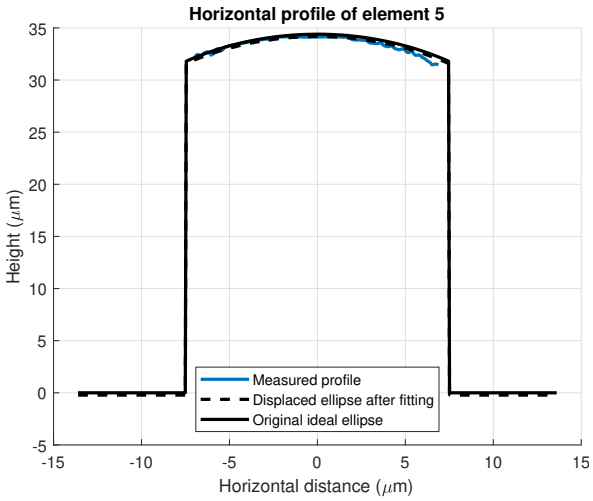

(a) Entire height range

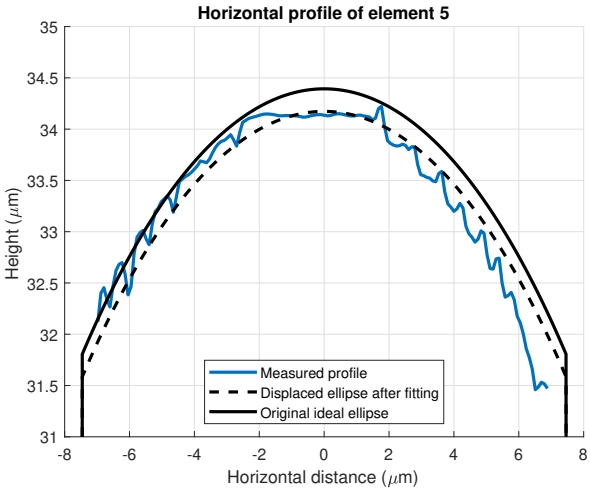

(b) Zoom at the elliptical part of the lens

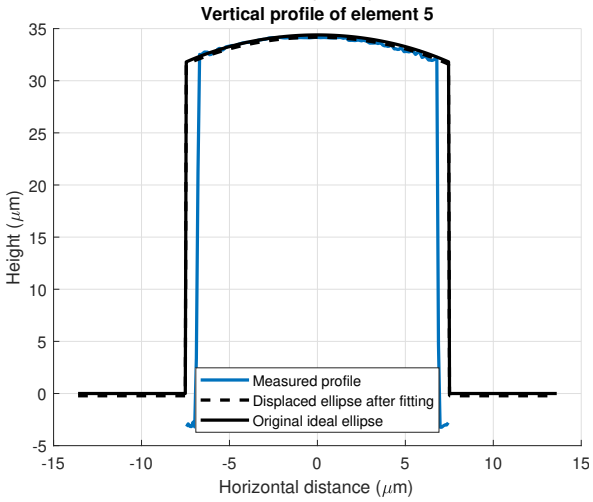

(c) Entire height range

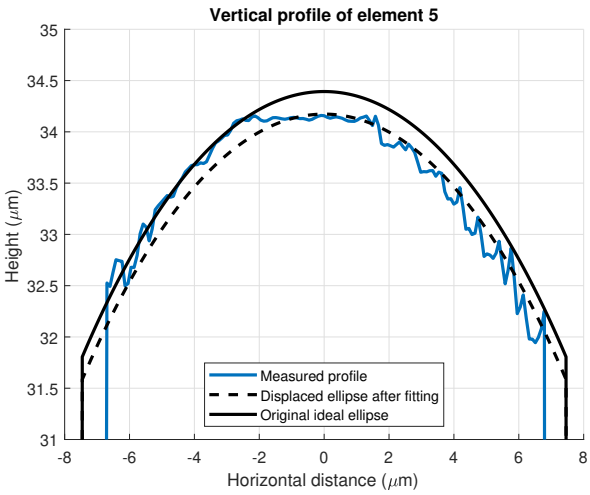

(d) Zoom at the elliptical part of the lens

Figure C.6: Element 5

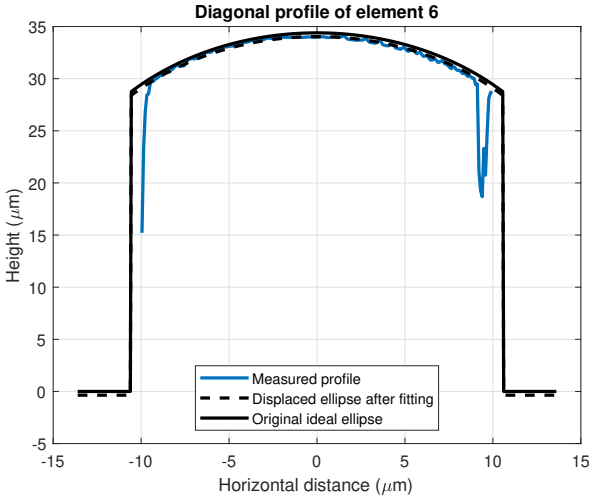

(a) Entire height range

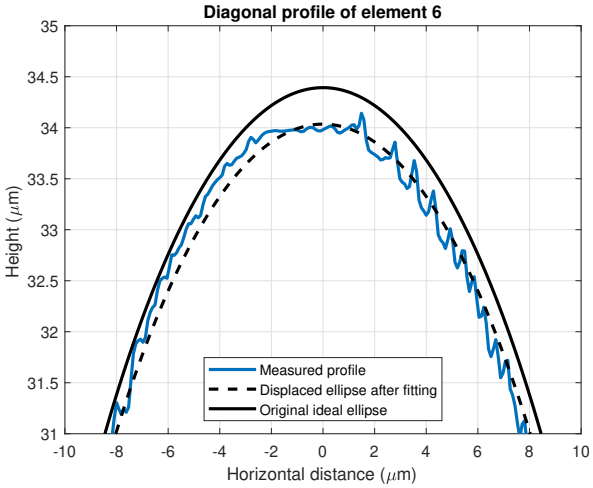

(b) Zoom at the elliptical part of the lens

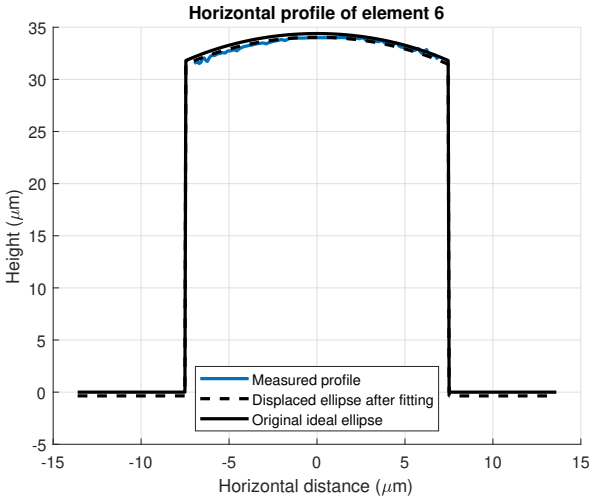

(c) Entire height range

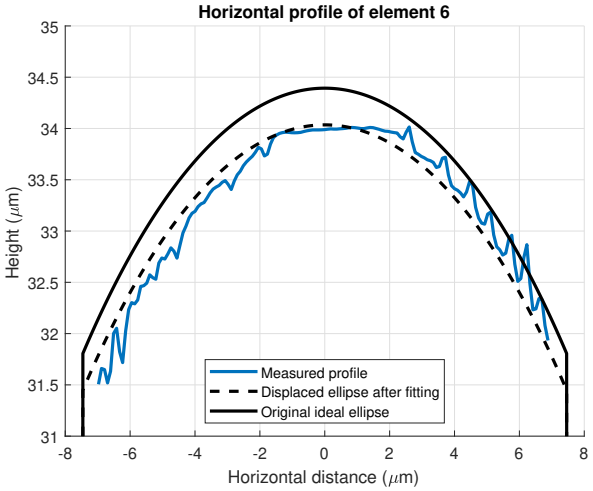

(d) Zoom at the elliptical part of the lens

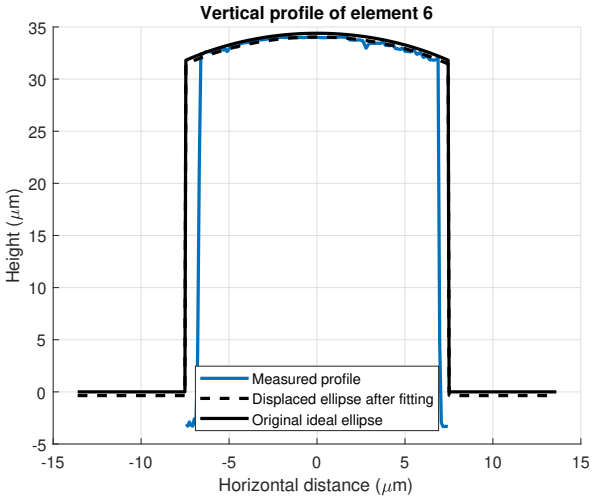

(e) Entire height range

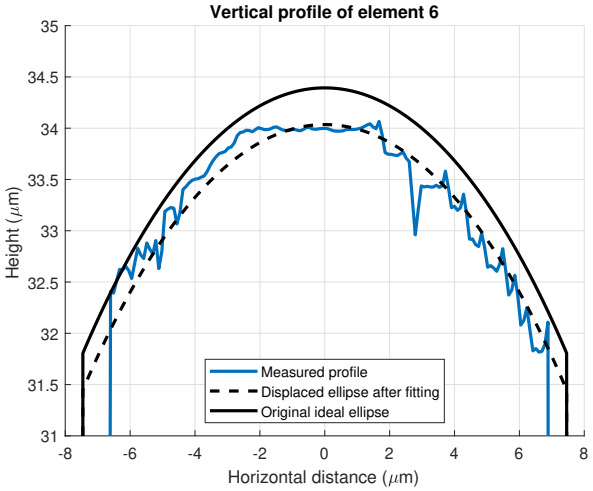

(f) Zoom at the elliptical part of the lens

Figure C.7: Element 6

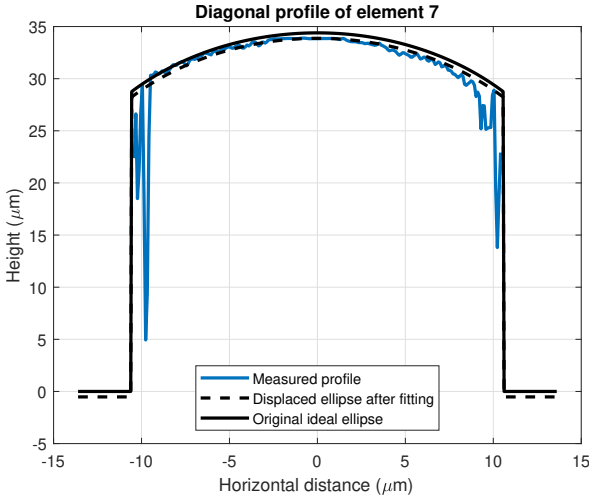

(a) Entire height range

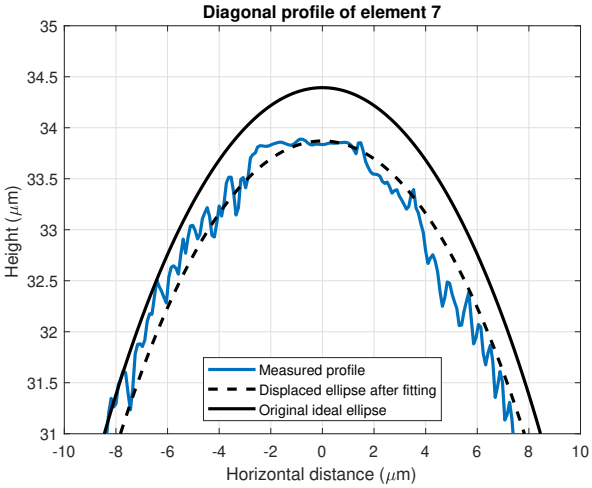

(b) Zoom at the elliptical part of the lens

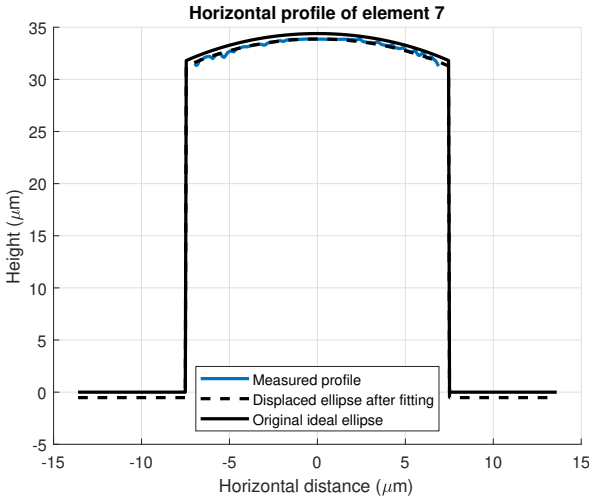

(c) Entire height range

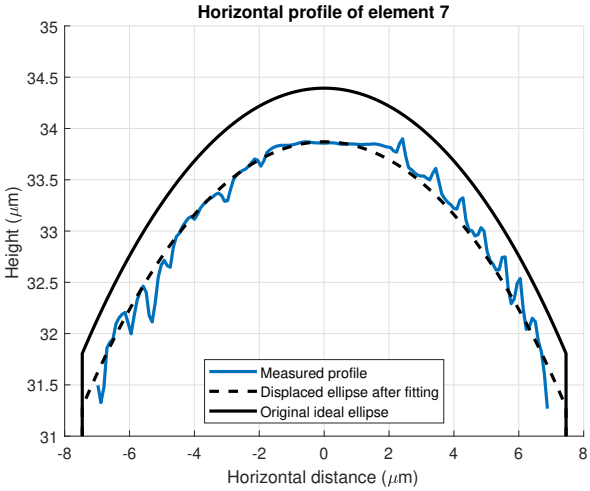

(d) Zoom at the elliptical part of the lens

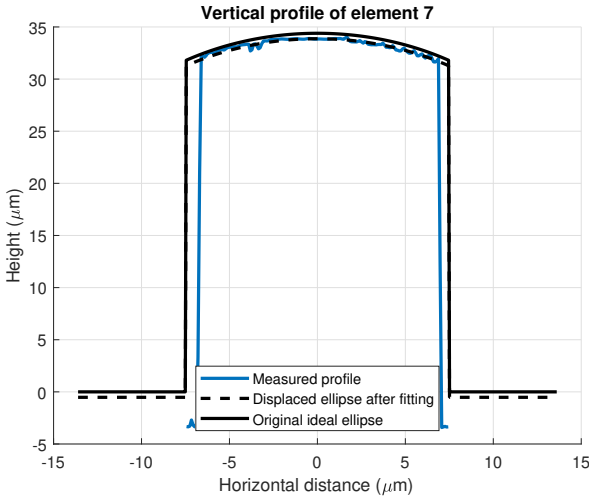

(e) Entire height range

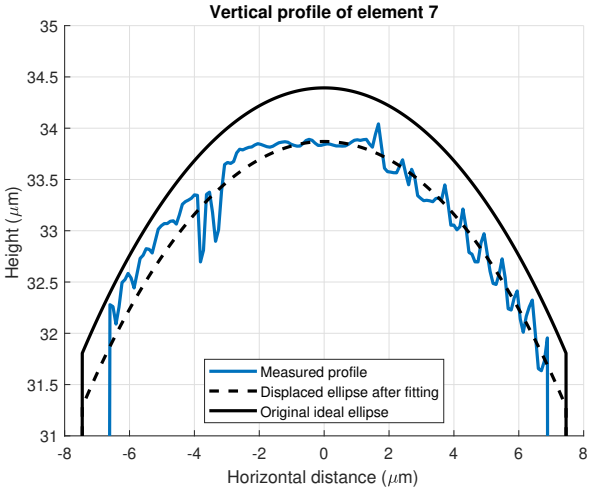

(f) Zoom at the elliptical part of the lens

Figure C.8: Element 7

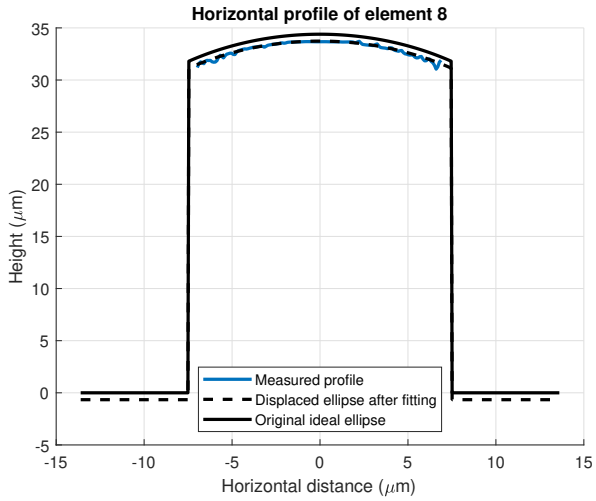

(a) Entire height range

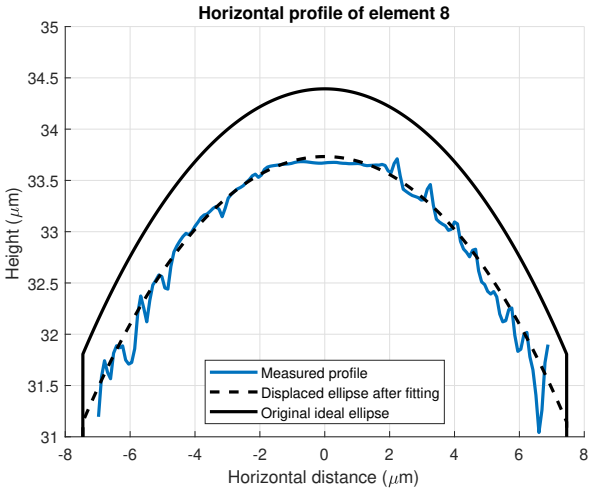

(b) Zoom at the elliptical part of the lens

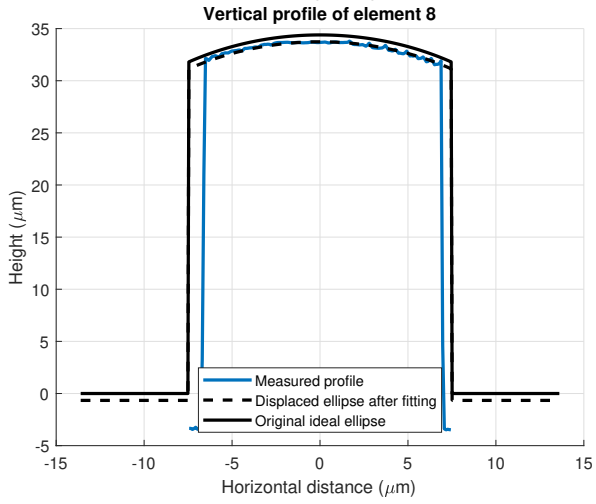

(c) Entire height range

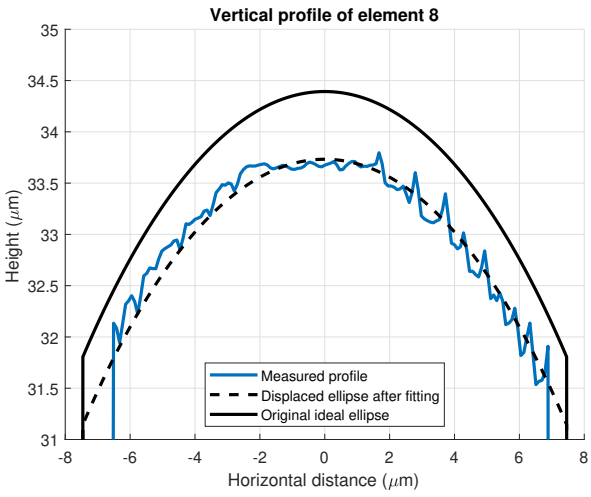

(d) Zoom at the elliptical part of the lens

Figure C.9: Element 8

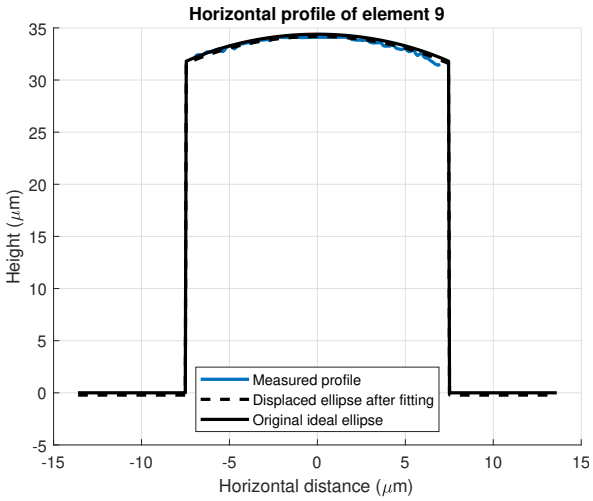

(a) Entire height range

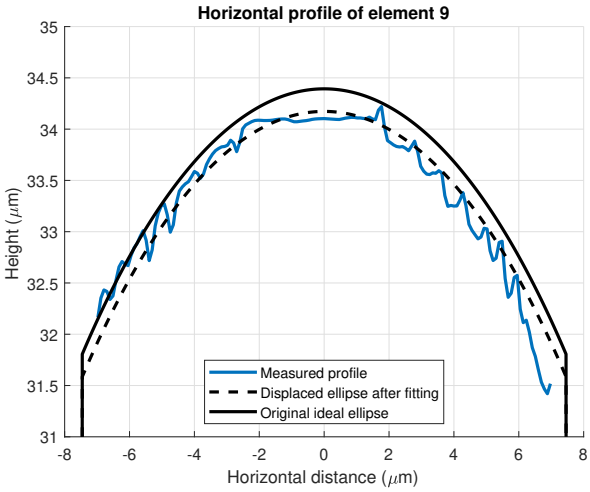

(b) Zoom at the elliptical part of the lens

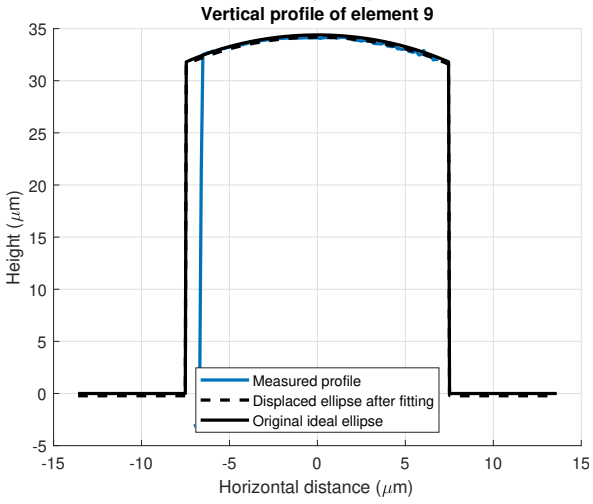

(c) Entire height range

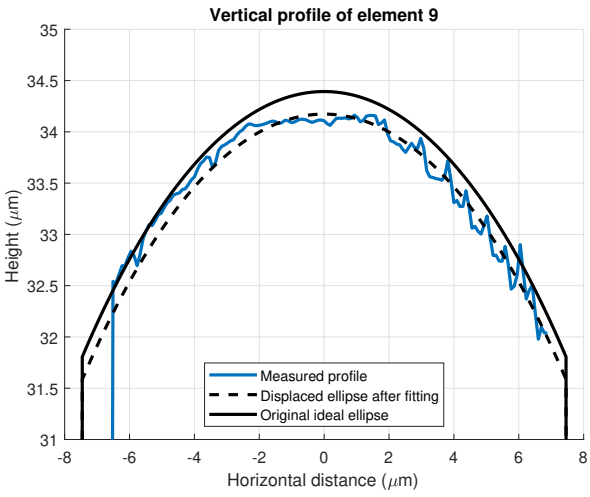

(d) Zoom at the elliptical part of the lens

Figure C.10: Element 9

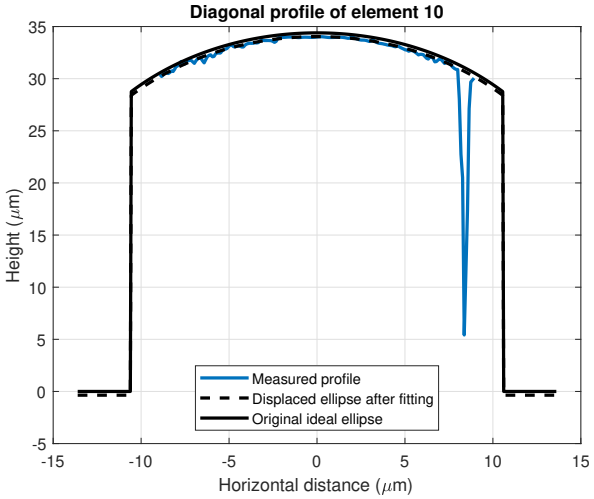

(a) Entire height range

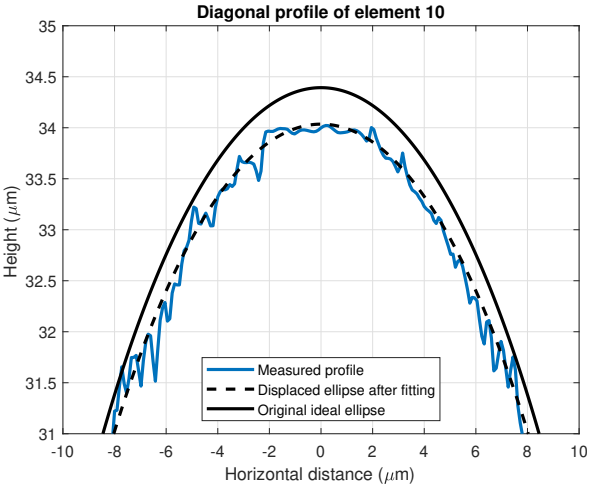

(b) Zoom at the elliptical part of the lens

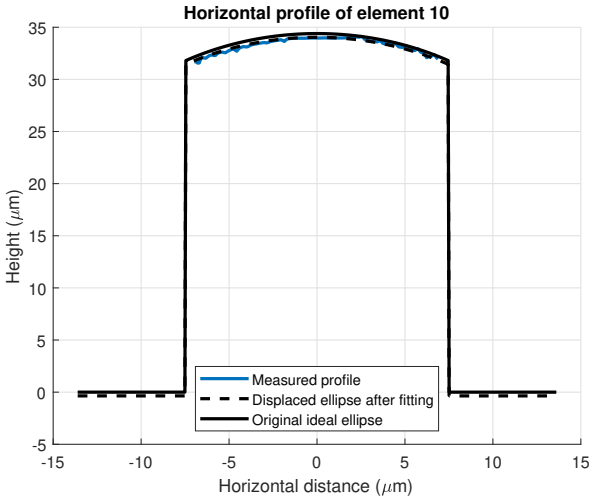

(c) Entire height range

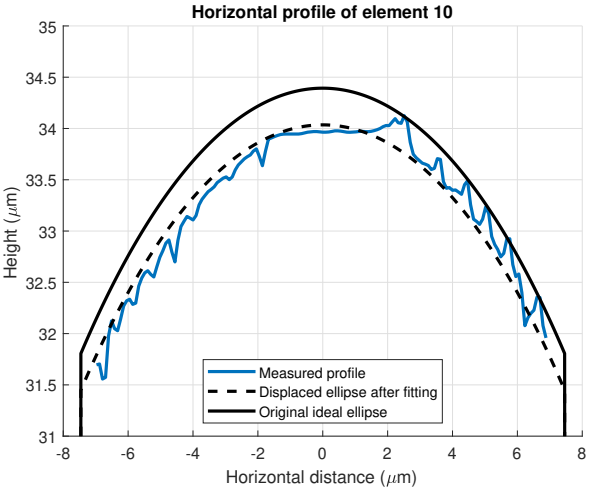

(d) Zoom at the elliptical part of the lens

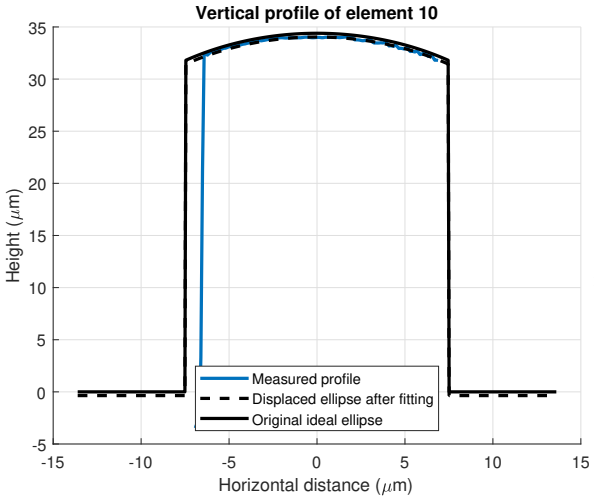

(e) Entire height range

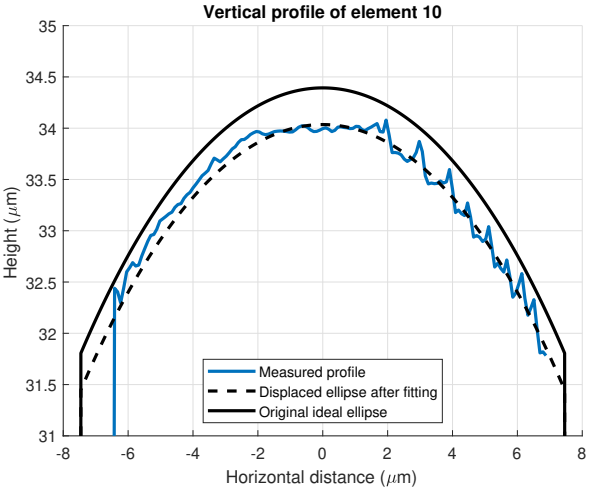

(f) Zoom at the elliptical part of the lens

Figure C.11: Element 10

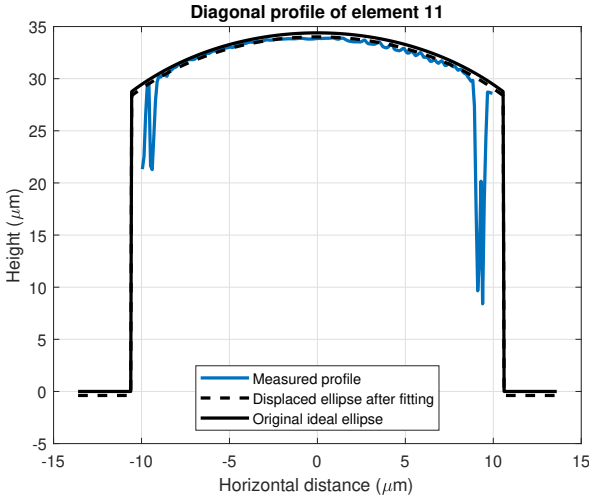

(a) Entire height range

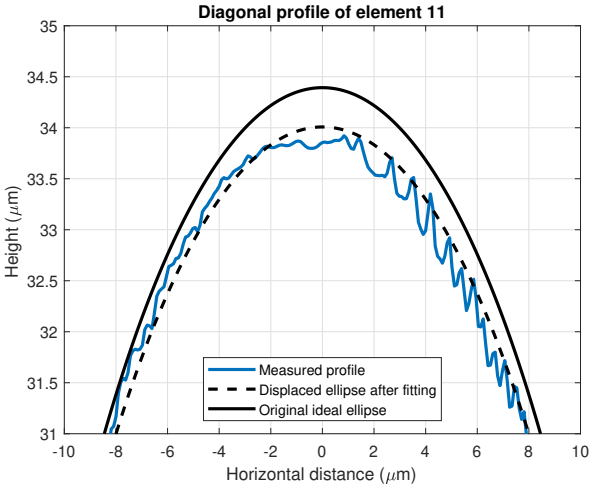

(b) Zoom at the elliptical part of the lens

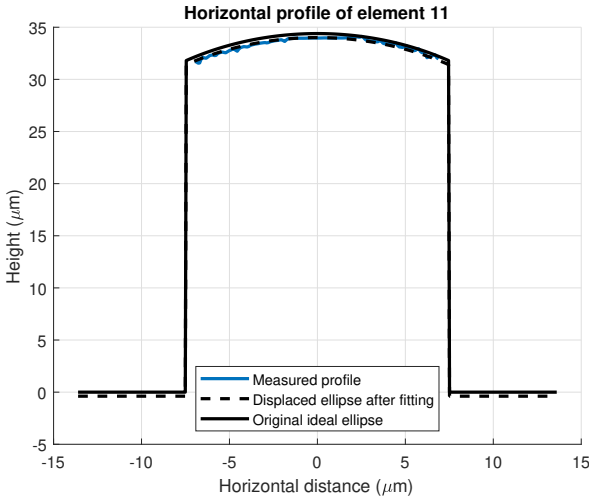

(c) Entire height range

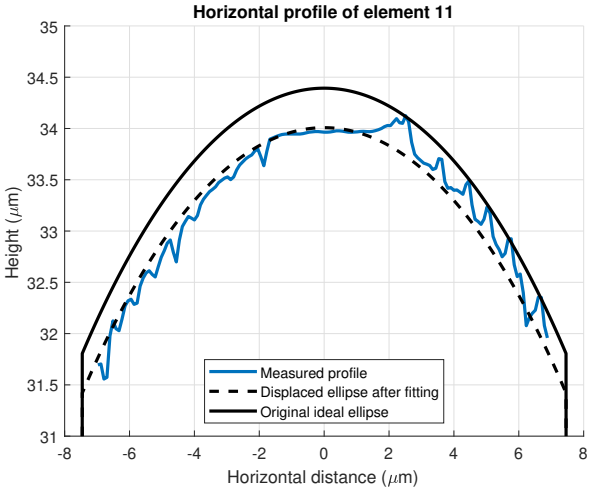

(d) Zoom at the elliptical part of the lens

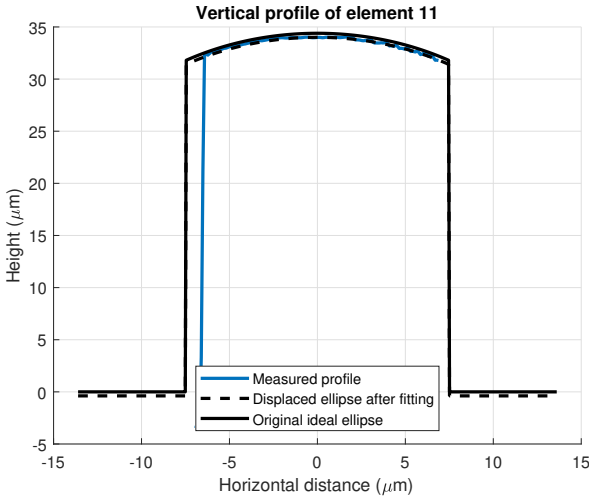

(e) Entire height range

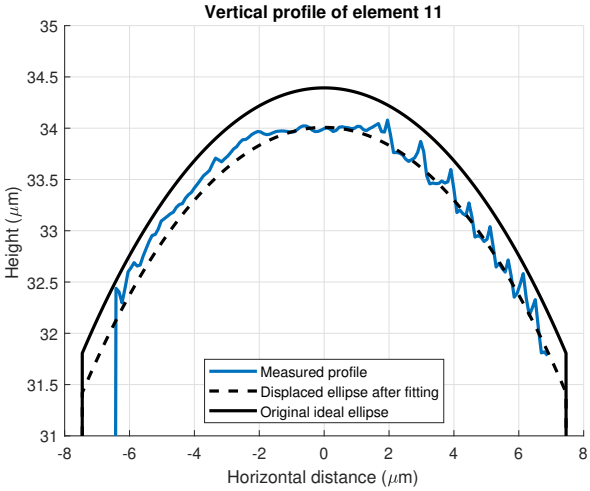

(f) Zoom at the elliptical part of the lens

Figure C.12: Element 11

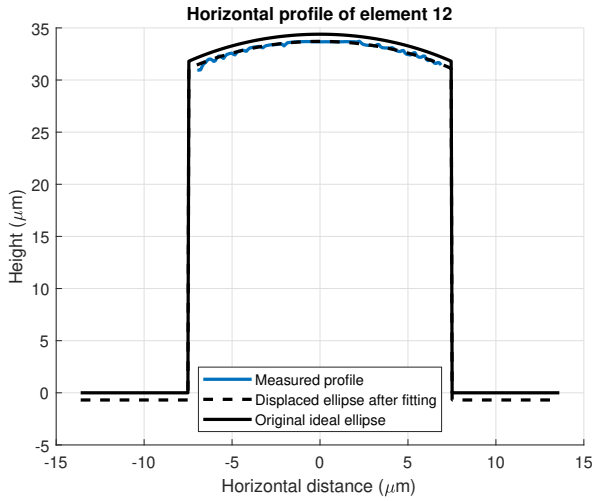

(a) Entire height range

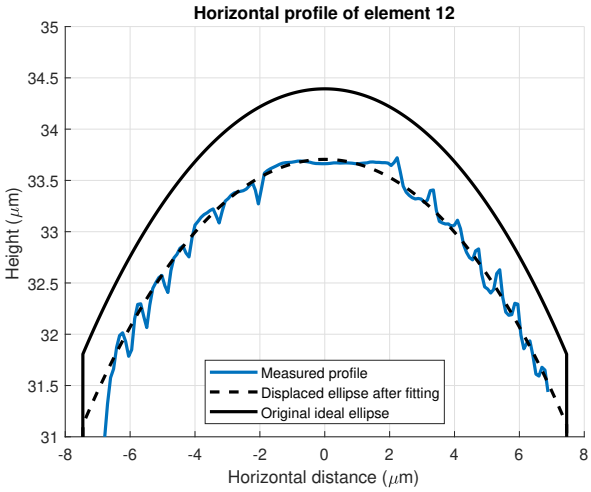

(b) Zoom at the elliptical part of the lens

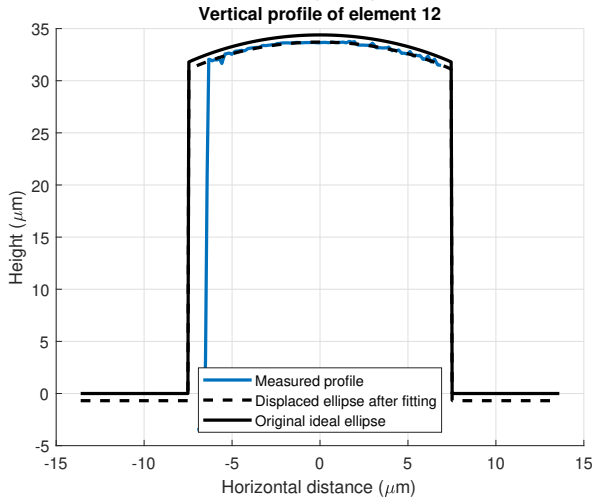

(c) Entire height range

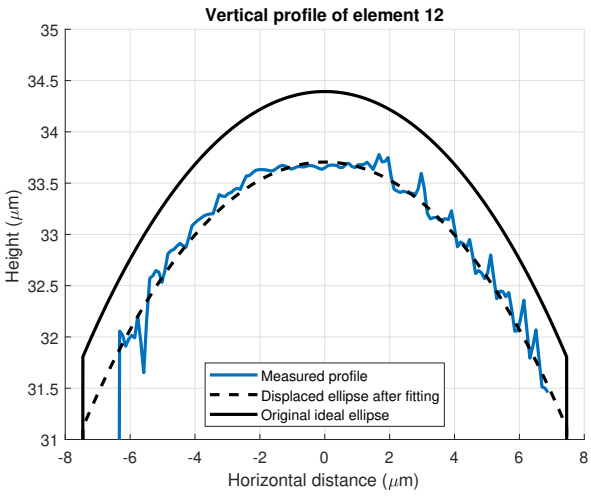

(d) Zoom at the elliptical part of the lens

Figure C.13: Element 12

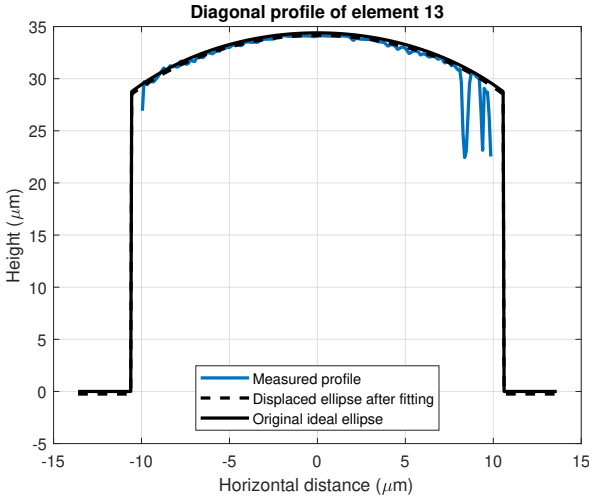

(a) Entire height range

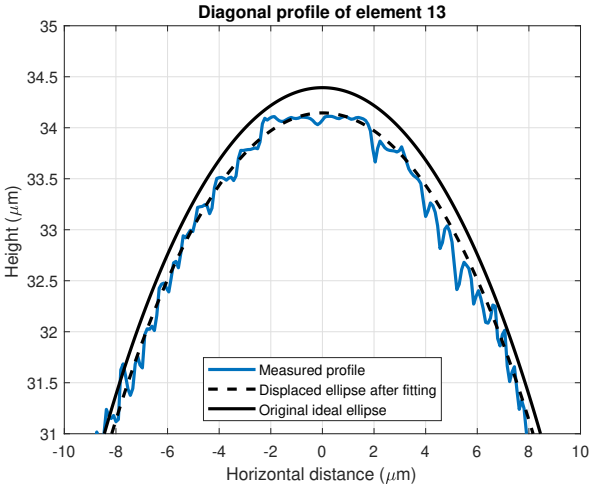

(b) Zoom at the elliptical part of the lens

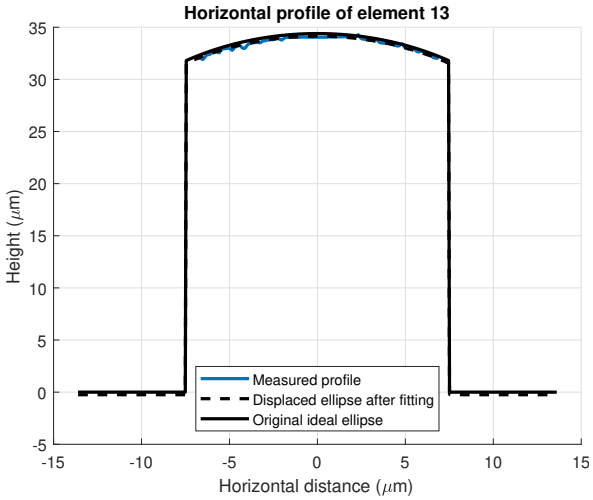

(c) Entire height range

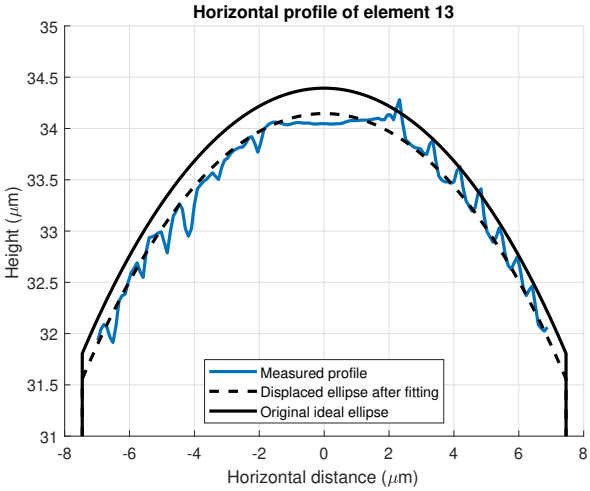

(d) Zoom at the elliptical part of the lens

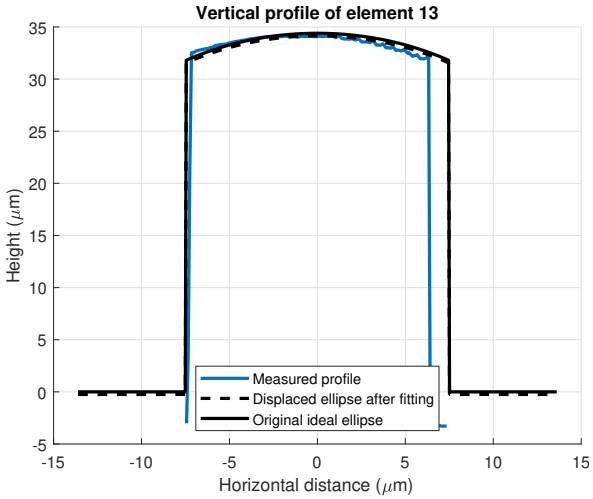

(e) Entire height range

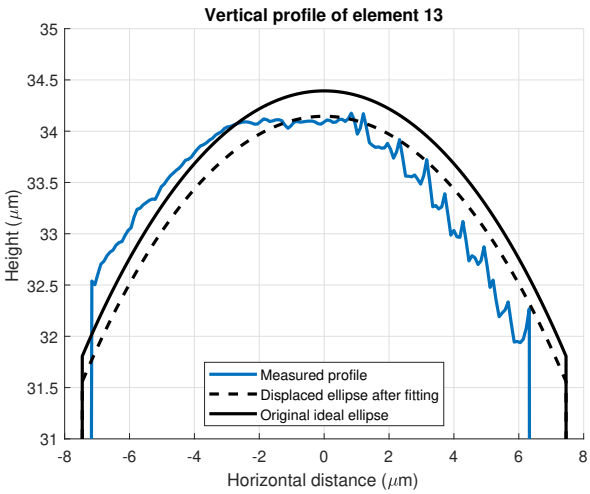

(f) Zoom at the elliptical part of the lens

Figure C.14: Element 13

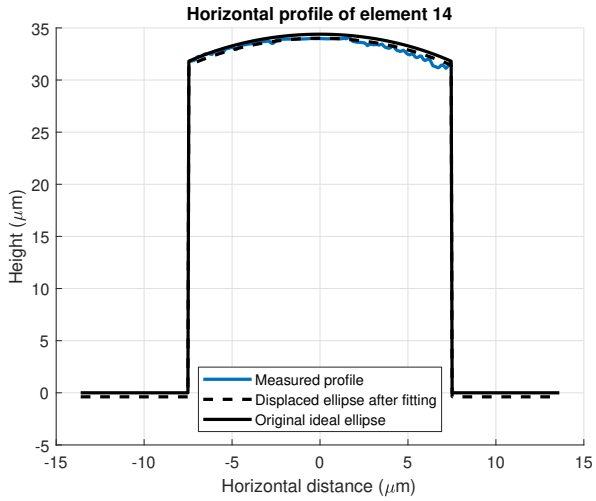

(a) Entire height range

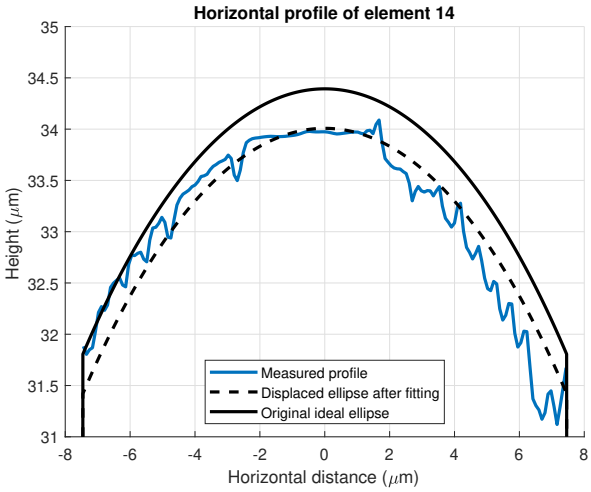

(b) Zoom at the elliptical part of the lens

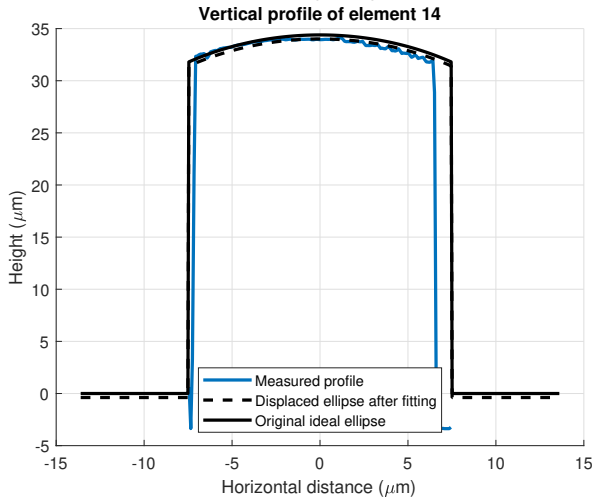

(c) Entire height range

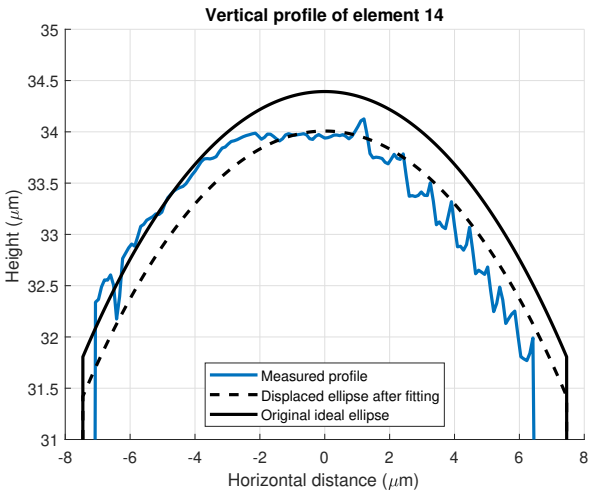

(d) Zoom at the elliptical part of the lens

Figure C.15: Element 14

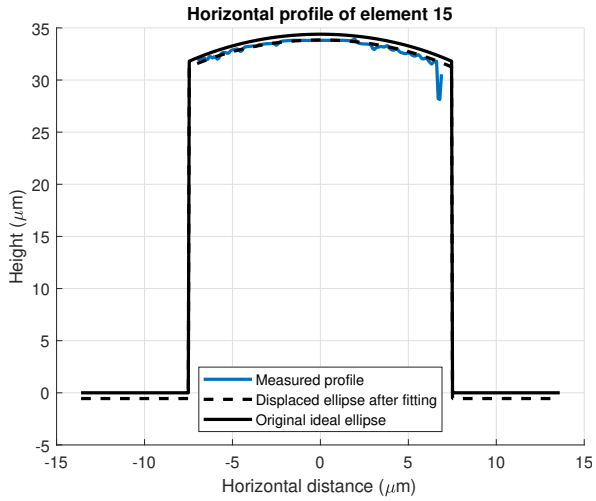

(a) Entire height range

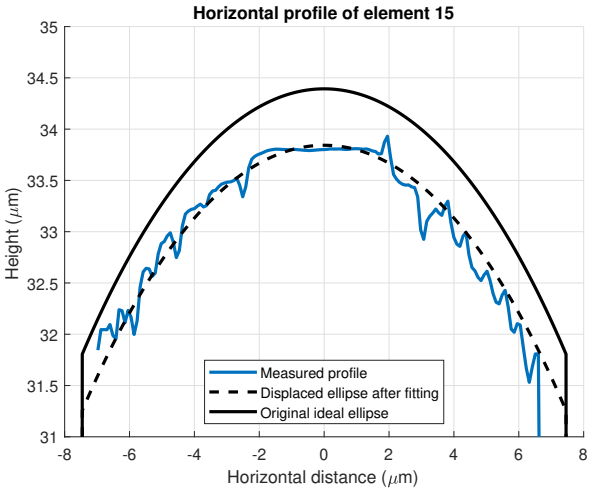

(b) Zoom at the elliptical part of the lens

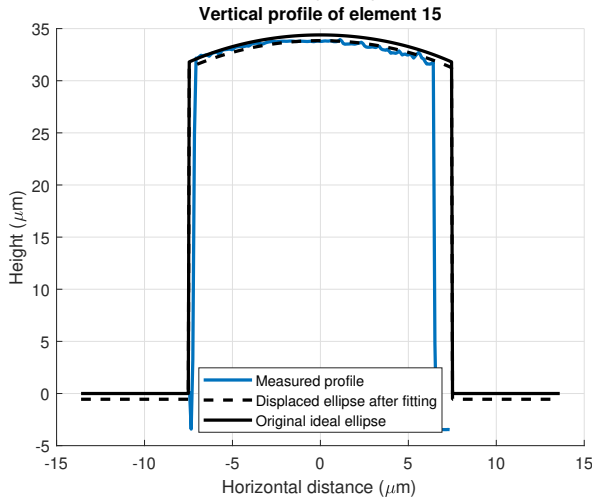

(c) Entire height range

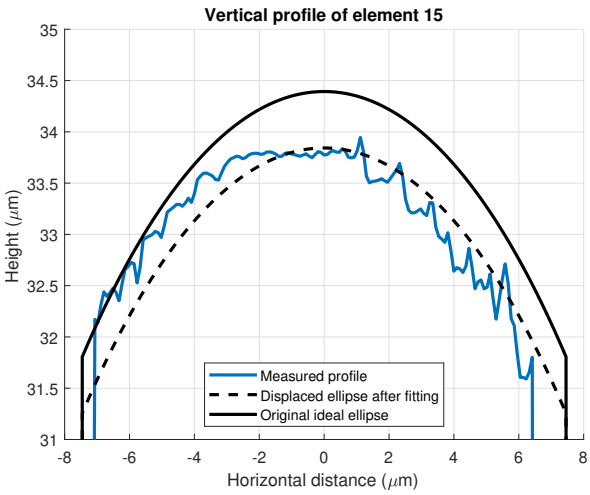

(d) Zoom at the elliptical part of the lens

Figure C.16: Element 15

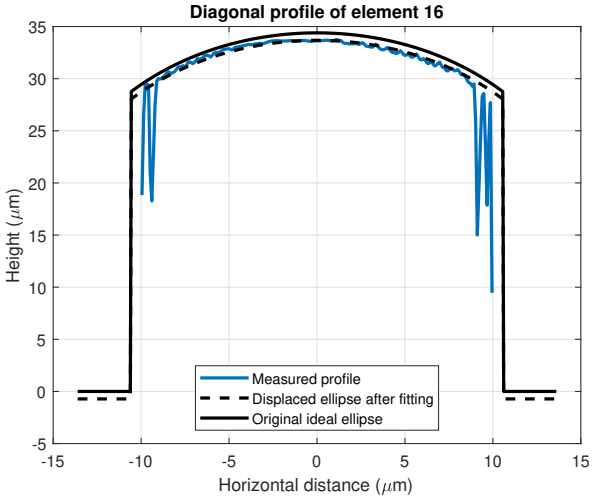

(a) Entire height range

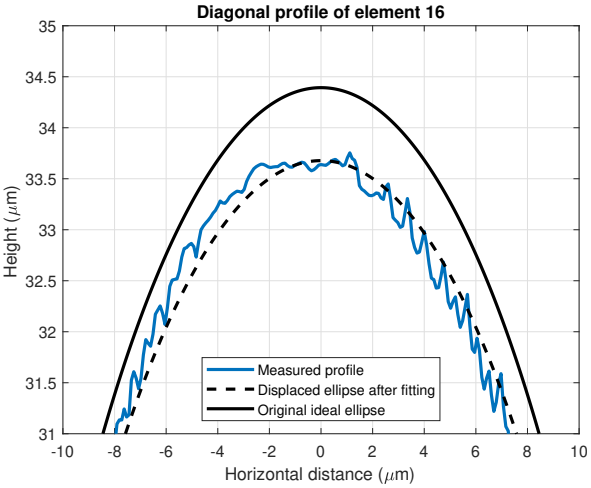

(b) Zoom at the elliptical part of the lens

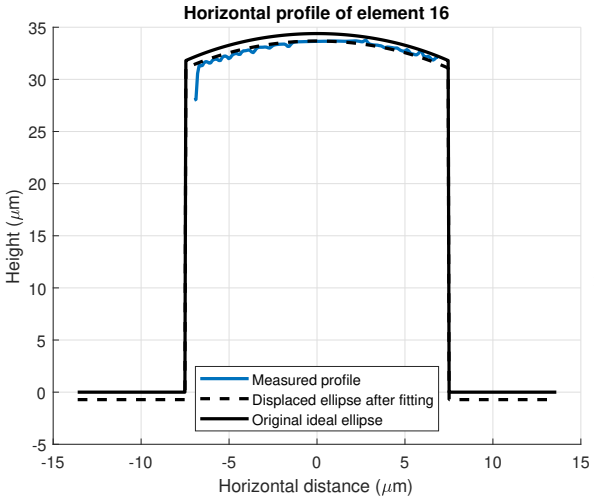

(c) Entire height range

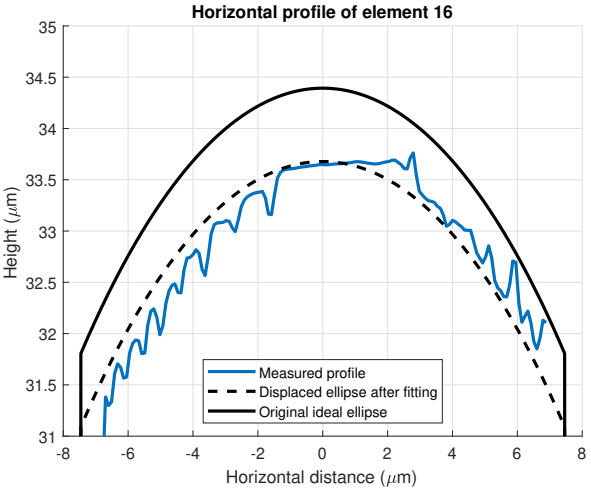

(d) Zoom at the elliptical part of the lens

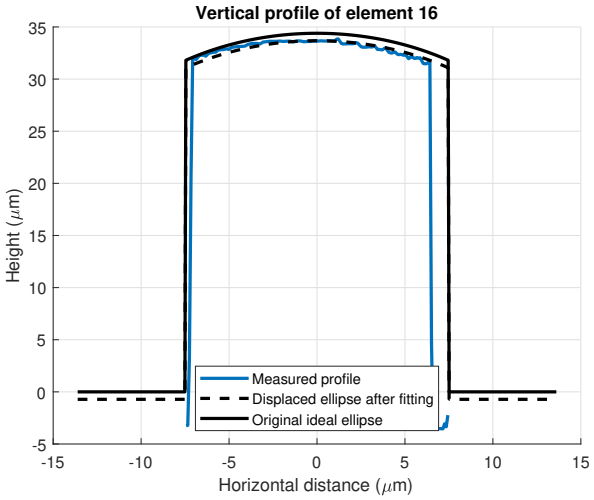

(e) Entire height range

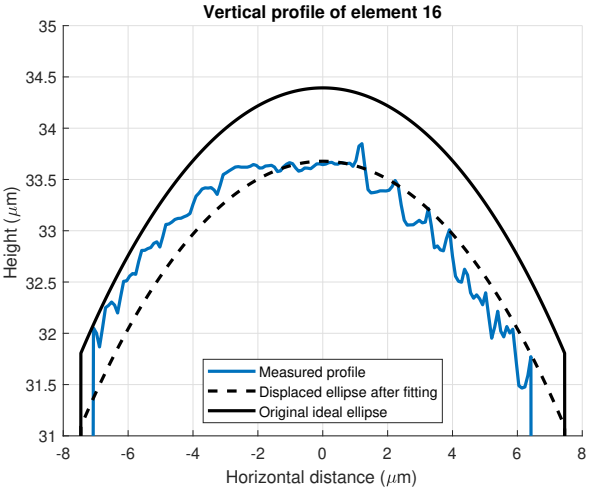

(f) Zoom at the elliptical part of the lens

Figure C.17: Element 16

C.2. Aberrated fields

The aberrated fields have been calculated according to Eq. 3.1. In Fig. C.18 we illustrate the normalized field pattern for each of the 16 elements of the microlens array that were measured and analyzed. We observe that, as expected, when the displacement of the fitted ellipse is large, the defocusing is more intense compared to the cases when the displacement is small. As a reference, for zero aberration the 2D field pattern is given in Fig. 3.16b.

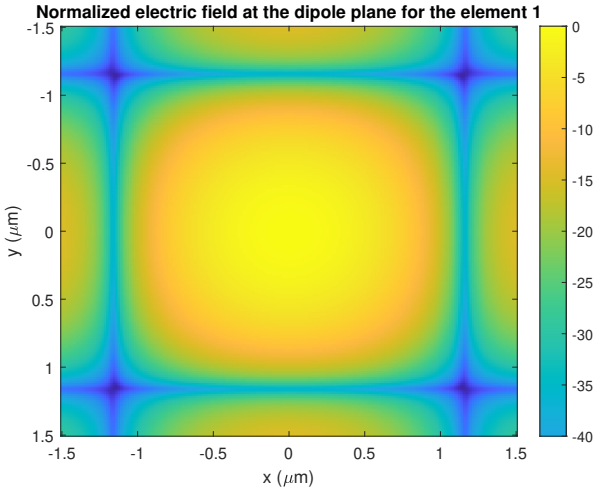

(a) $\delta z = -0.2476 \mu m$

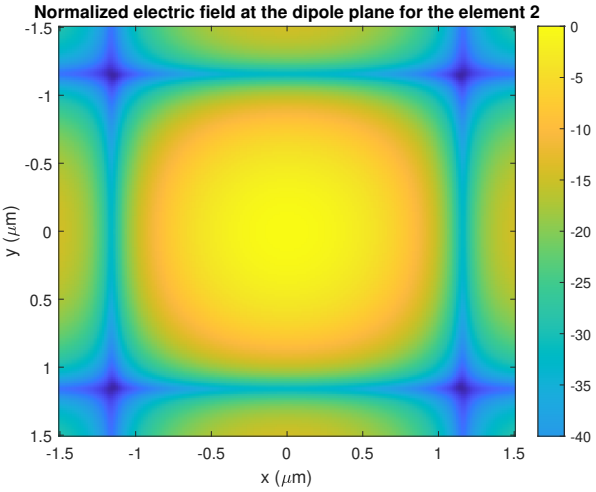

(b) $\delta z = -0.3852 \mu m$

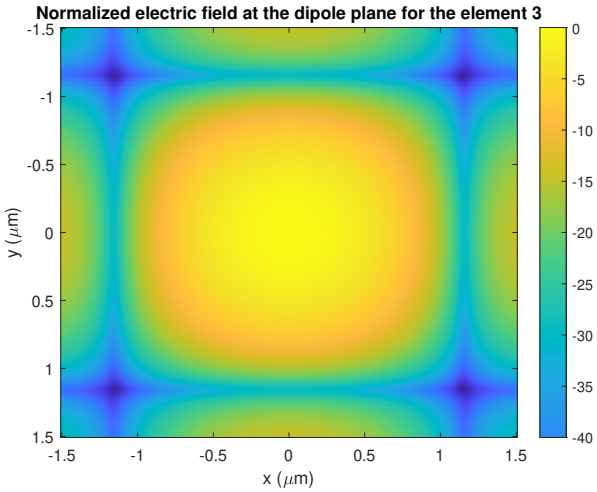

(c) $\delta z = -0.5228 \mu m$

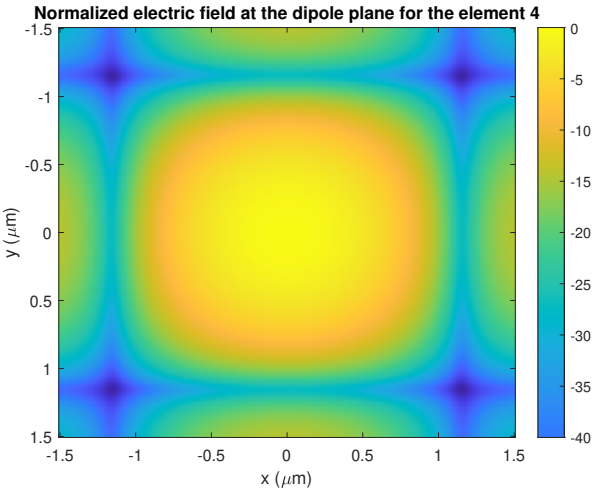

(d) $\delta z = -0.6879 \mu m$

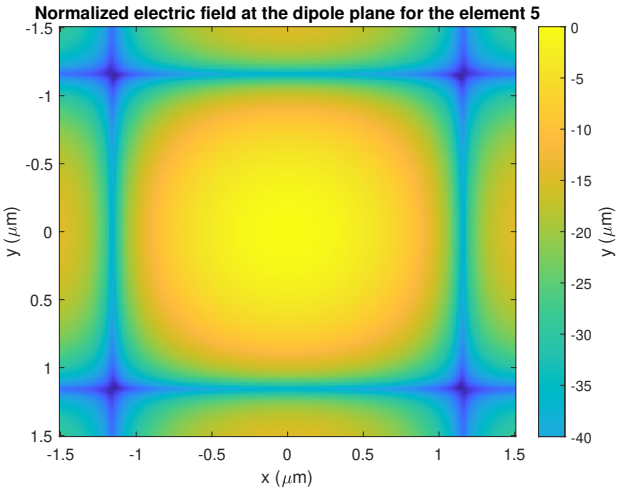

(e) $\delta z = -0.2201 \mu m$

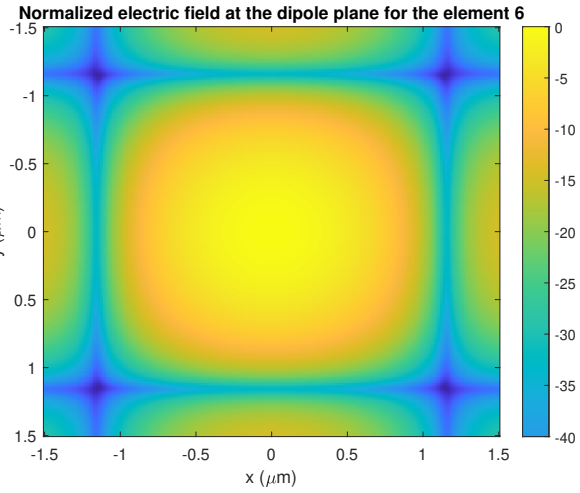

(f) $\delta z = -0.3577 \mu m$

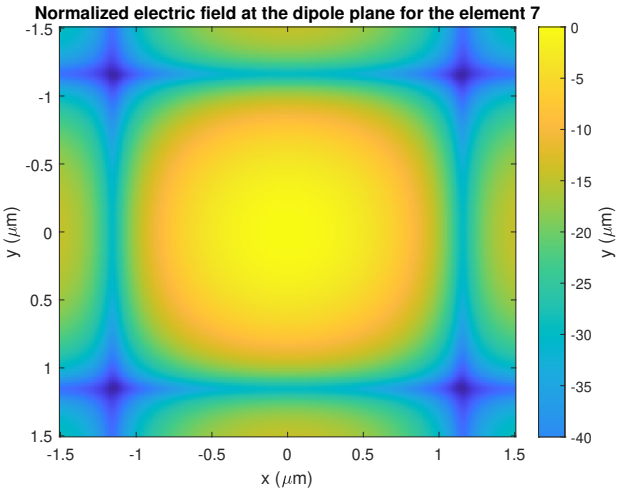

(g) $\delta z = -0.5228 \mu m$

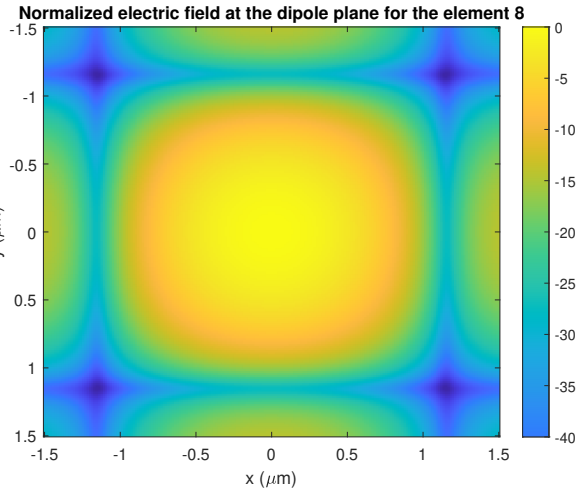

(h) $\delta z = -0.6603 \mu m$

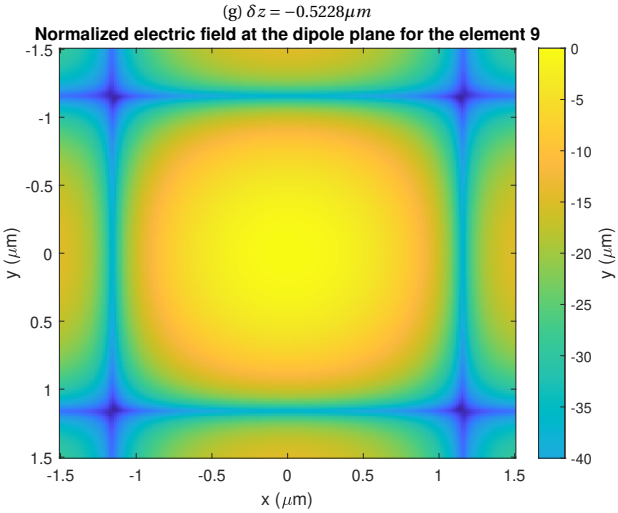

(i) $\delta z = -0.2201 \mu m$

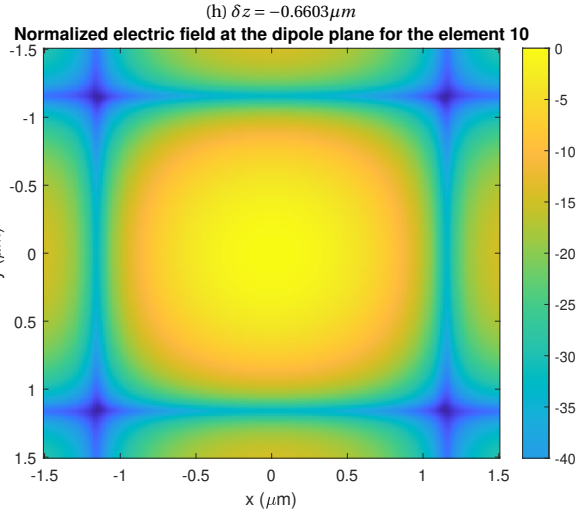

(j) $\delta z = -0.3577 \mu m$

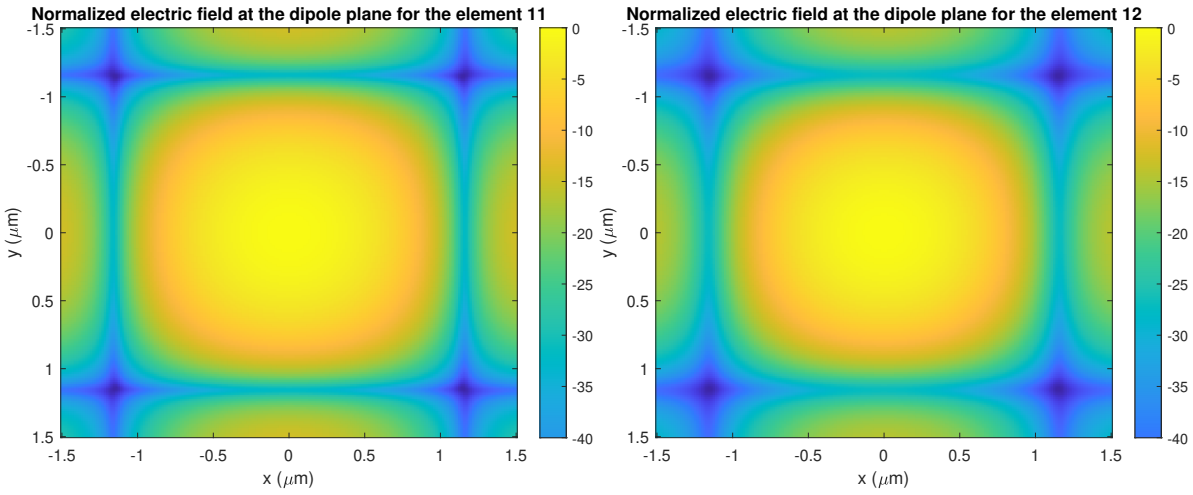

(k) $\delta z = -0.3582 \mu m$

(l) $\delta z = -0.6879 \mu m$

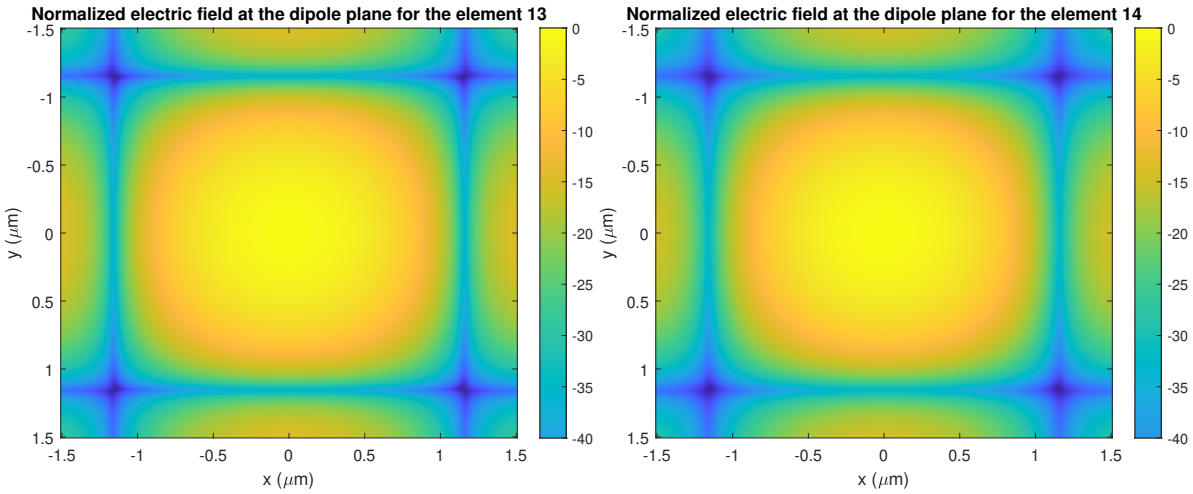

(m) $\delta z = -0.2476 \mu m$

(n) $\delta z = -0.3852 \mu m$

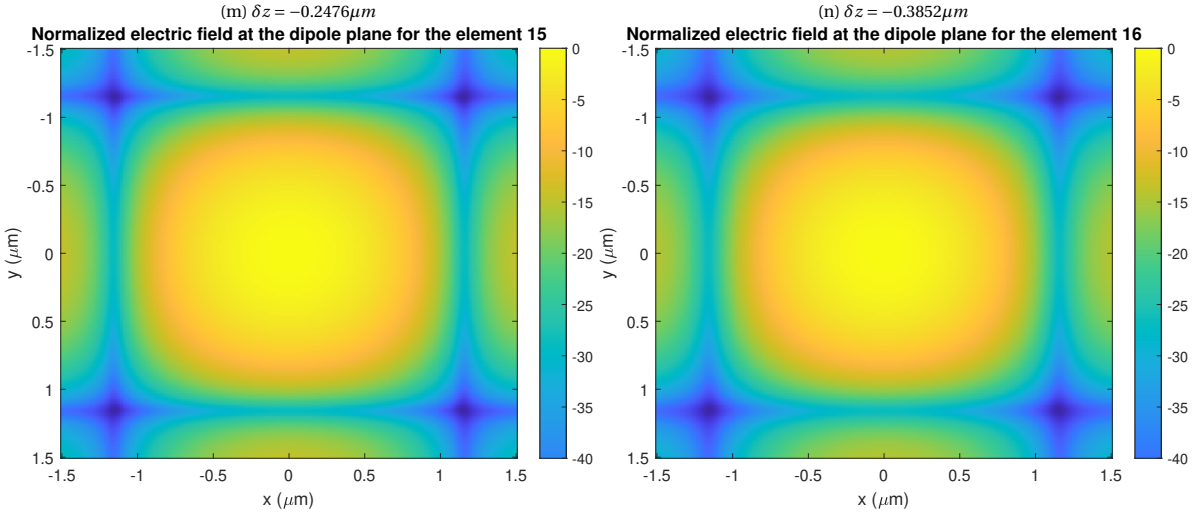

(o) $\delta z = -0.5503 \mu m$

(p) $\delta z = -0.7154 \mu m$

Figure C.18: Plots of amplitude of electric field at the planes $\phi = 0°$ and $\phi = ang90$ at various frequencies.

D

Guide for Matlab App of Lens Antennas in Tx

The GUI described in Section 4 allows the user to find the electric and magnetic field transmitted by a lens antenna for any feed and for any sizes of an elliptical or extended hemispherical lens. Here we explain the steps that the user needs to follow in order to

- select their desired parameters for their configuration
- calculate the fields
- plot the results
- save the results.

The main window of the GUI is the one displayed in Fig. 4.1. It consists of 3 columns, the first 2 of which are related to inputs for the tool. The last column includes buttons for the calculation of the far field from the lens antenna, information based on the results about efficiencies and directivity and options for plotting and saving the results.

D.1. Inputs

The first property that the user needs to define is the type of lens. Initially there are two available options, extended hemispherical and elliptical shape. If the user selects elliptical lens, as shown in Fig. D.1b, then all subsequent options regarding the lens type are disabled. Furthermore, the option "Distance computed from" at the bottom of the first column, which determines the sphere on which the far field from the lens antenna is computed, is locked at the lens apex value, because for an elliptical lens the virtual focal distance is at infinity. However, if the user selects that the lens type is an extended hemispherical lens, as shown in Fig. D.1a, then a second drop-down menu at the middle of the first column is activated. In this menu, the user is asked to select the specific lens type which can be

- a hyperhemispherical lens, according to the definition of hyperhemispherical lens given in [31]
- a synthesized elliptical lens, which is an extended hemispherical lens whose surface tries to fit an elliptical lens
- a user defined lens, with extension length and virtual focal distance freely defined by the user.

Also, the user can choose whether they want the center of the sphere, on which the far field will be computed, at the lens apex or at the virtual focal distance. The option of the lens apex is recommended for the synthesized elliptical lens and the option of the virtual focal is recommended for the hyperhemispherical lens. The recommended points are such that the phase is constant along the far field sphere.

The next lens properties that need to be defined are the (real) permittivity of the lens and the permittivity and thickness of the matching layer, if there is one. For the latter the user can tick the box "Matching layer"

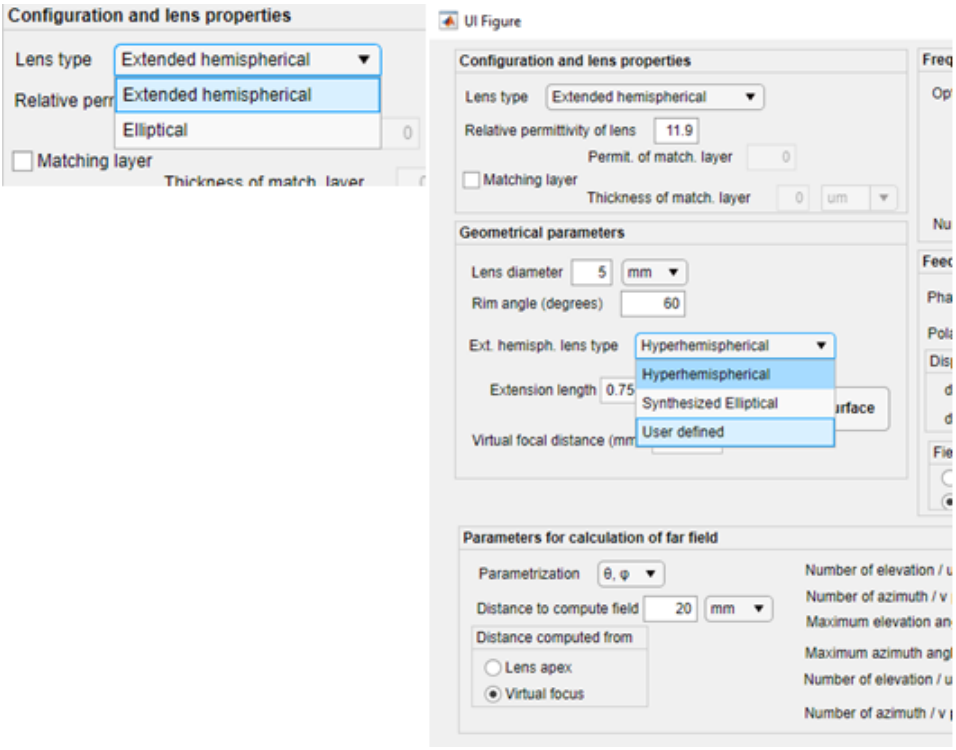

(a) Options for extended hemispherical lens

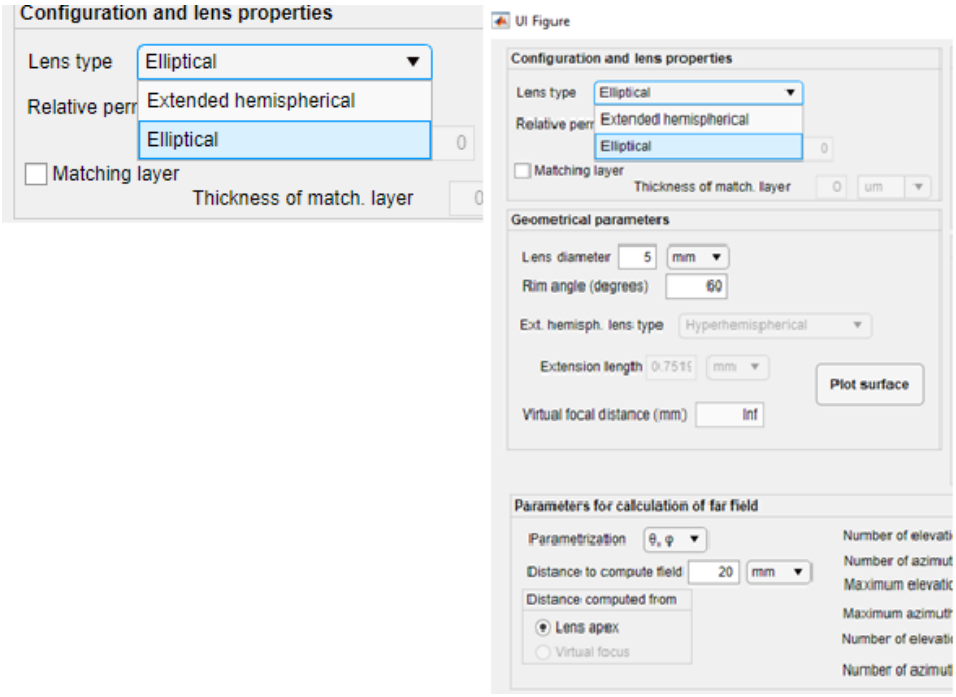

(b) Options for elliptical lens

Figure D.1: First column of the GUI main window with all options for lens type

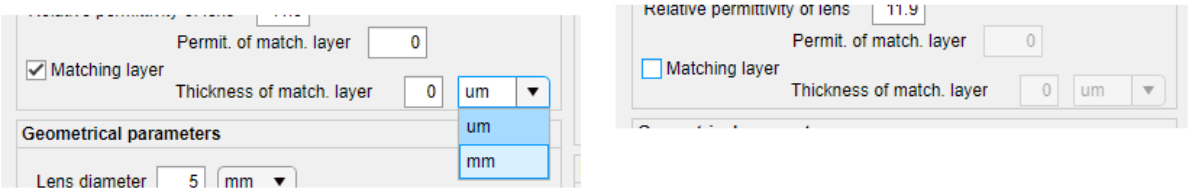

Figure D.2: Option for adding a matching layer at the lens interface

if the configuration includes a matching layer and can then edit the fields regarding the permittivity and thickness of the matching layer. Otherwise, the fields are not editable. This effect is shown in Fig. D.2.

In the middle of the first column, one finds the section *Geometrical parameters*. Here the user needs to determine the diameter of the lens D and the rim angle θ_0. These two parameters, along with the permittivity of the lens, are sufficient for the tool in order to plot the surface of the lens, if the lens type is elliptical, hyperhemispherical or synthesized elliptical. Specifically, if the lens type is elliptical, the ellipse parameters are computed as

$$e = \frac{1}{\sqrt{\epsilon_r}}$$

$$a \cdot \sqrt{1 - \frac{\left(\frac{D}{2}\right)^2}{a^2 \cdot (1-e^2)}} = \frac{\frac{D}{2}}{tan\theta_0}$$

$$c = a \cdot e$$

$$b = \sqrt{a^2 - c^2}$$

If the lens type is hyperhemispherical, the radius of the hemisphere R_{hyps}, the extension length L and the virtual focal distance f_v are computed as

$$\left(\frac{\frac{D}{2}}{tan\theta_0} - \frac{R_{hyps}}{\sqrt{\epsilon_r}}\right)^2 + \left(\frac{D}{2}\right)^2 = R_{hyps}^2$$

$$L = \frac{R_{hyps}}{\sqrt{\epsilon_r}}$$

$$f_v = R_{hyps}(1 + \sqrt{\epsilon_r})$$

If the lens type is synthesized elliptical, the respective parameters are, following the approximation proposed in [50],

$$e = \frac{1}{\sqrt{\epsilon_r}}$$

$$\left(\frac{\frac{D}{2}}{tan\theta_0} - R_{hyps}\left(\frac{1+e}{\sqrt{1-e^2}} - 1\right)\right)^2 + \left(\frac{D}{2}\right)^2 = R_{hyps}^2$$

$$L = R_{hyps}\left(\frac{1+e}{\sqrt{1-e^2}} - 1\right)$$

$f_v \approx \infty$ and practically it is calculated in the tool as $100 R_{hyps}$

For the user defined case, the tool needs the extension length of the lens and the virtual focal distance to be added by the user. Then, the radius of the hemisphere is

$$\left(\frac{\frac{D}{2}}{tan\theta_0} - L\right)^2 + \left(\frac{D}{2}\right)^2 = R_{hyps}^2$$

For the elliptical case, the geometrical parameters are not displayed in the main window of the GUI, whereas for the different types of the extended hemispherical lens, the extension length and the virtual focal distance are displayed. Fig. D.3 shows the section of the geometrical parameters for the different available

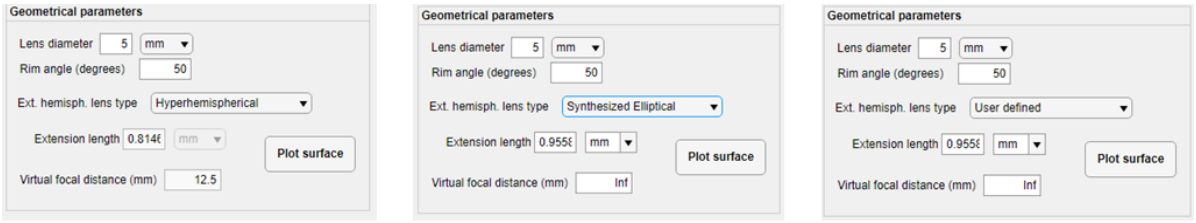

Figure D.3: Geometrical parameters section for different cases of extended hemispherical lenses.

options. We should note that when a hyperhemispherical lens is selected, the fields for the extension length and virtual focal distance are computed by the tool and are not editable for the user. On the other hand, when a synthesized elliptical lens is selected, the extension length and the virtual focal distance are computed by the tool and updated in the main window, but the fields are editable for the user, because the user may want to apply a different method from the one suggested in [50] to determine the geometrical parameters. Finally, at the user defined case all fields are editable for the user and no suggestions are displayed by the tool.

The geometrical parameters section includes a button through which the user can view the lens surface that has been created with the parameters that have been given so far. Fig. D.4 displays the output of the Plot surface button, when each of the four different lens types have been selected. For all lens types we observe that the plots show important information such as the lens diameter, the rim angle, the radius of the FO sphere and the permittivity of the lens material. For the cases of extended hemispherical lenses, the radius of the hemisphere and the virtual focus are also shown in the plot. For the synthesized elliptical lens, and in all cases when the virtual focus is very far from the lens, the point is not shown per se, but an arrow indicates that the direction of the virtual focus. Fig. D.4d shows a lens surface for user defined parameters that are given in the inset of Fig. D.4d.

The next section is related to parameters for the calculation of the far field. Firstly, the user can select the parametrization which shall be used in the calculation of the fields. This can be either (θ, ϕ) or (u, v), as shown in Fig. D.5, where $u = sin\theta cos\phi$ and $v = sin\theta sin\phi$. The other fields in this section are easily comprehensible. The number of points in both the lens surface and the far field sphere is an important parameter, as it determines the discretization of the space and thus the resolution, in the expense of computation time, when the resolution is set at a high level.

Another necessary section for the tool is the frequency of operation of the antenna. Here the user has also two options, as indicated in Fig. D.6; a single frequency or multiple frequencies. For multiple frequencies, the only option is a linear progression of frequencies, for which the user determines the minimum and maximum frequency, as well as the number of frequencies. Whenever the frequencies are updated, the respective listbox at the results section showing is updated, too, as we can see in Fig. D.6. The last section in the inputs part is the feed. The user gives values of the phase center, if it is shifted with respect to the focus of the lens, the displacement in x and y with respect to the focus and determined the polarization, which can be either horizontal or vertical. Lastly, the user needs to give as input the field of the feed. The windows that open for the user to load the data are given in Fig. D.7a and D.7b, depending on whether the data file comes from Matlab or CST. In Fig. D.7a, which is the window that opens for Matlab files, we present the window that opens for uploading the θ or u matrix. Similar windows open subsequently, where the user is asked to upload the ϕ or v matrix, and the matrices for E_θ and E_ϕ. An important note is that if the (u, v) parametrization has been previously selected, for CST input, the data are assumed to be in (θ, ϕ) parametrization and are transformed later to (u, v), whereas for Matlab input the data are assumed to be already in (u, v) parametrization. If the files have been loaded successfully, a message like the one of Fig. D.7c is shown that informs the user of the successful loading.

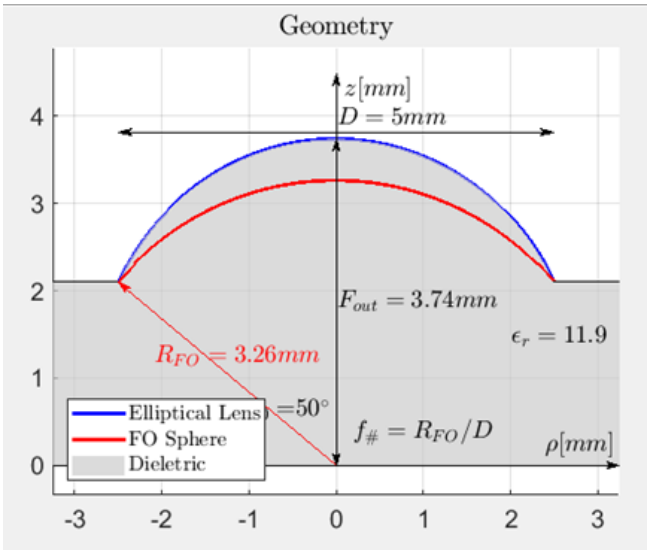

(a) Elliptical lens

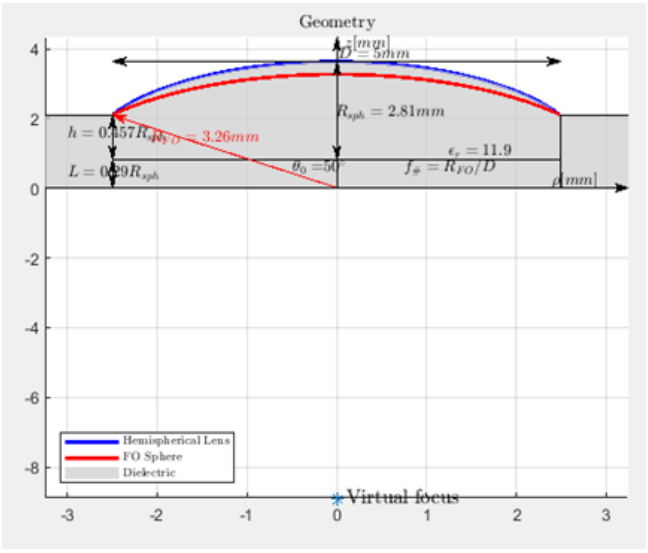

(b) Hyperhemispherical lens

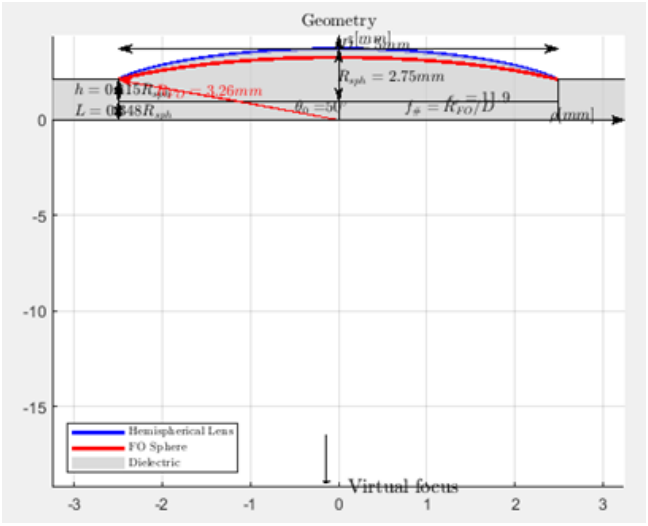

(c) Synthesized elliptical lens

Figure D.4: Plots of the surfaces of different lens types

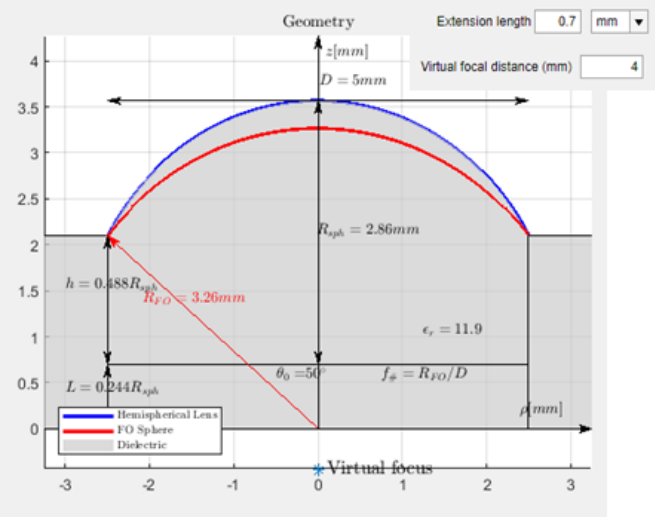

(d) User defined extended hemispherical lens

Figure D.4: Plots of the surfaces of different lens types (cont.)

Figure D.5: Parametrization options

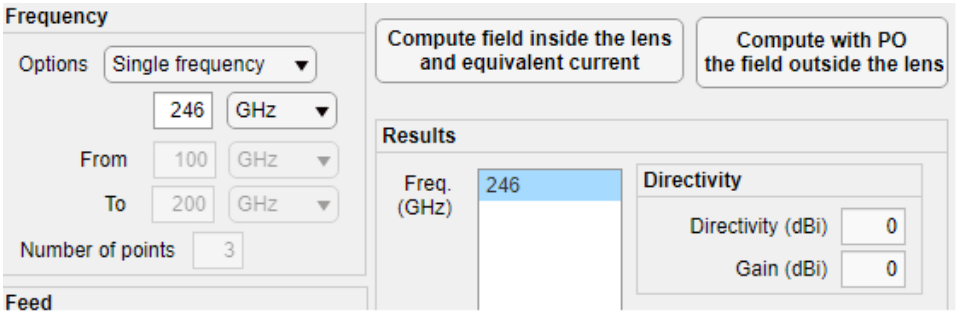

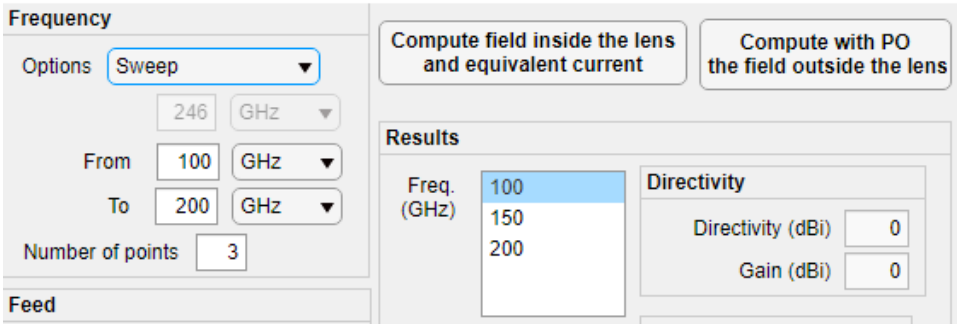

Figure D.6: Options for frequency

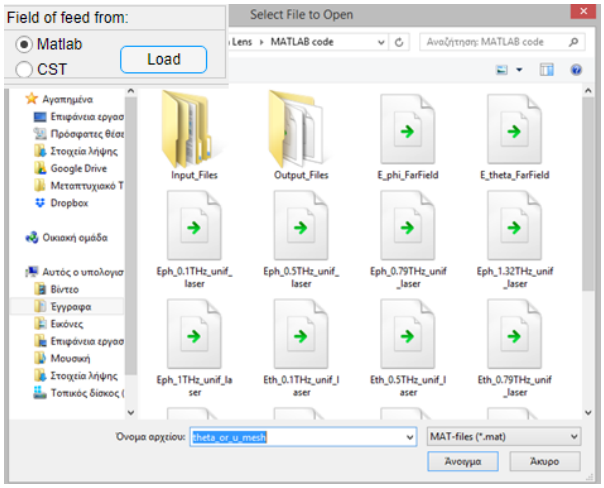

(a) Example of window for upload from Matlab file

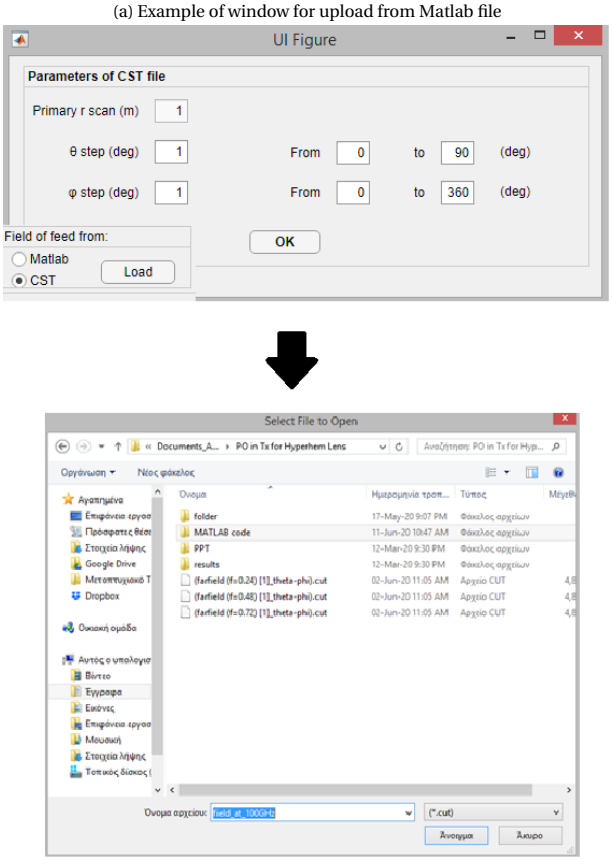

(b) Windows for upload from CST file

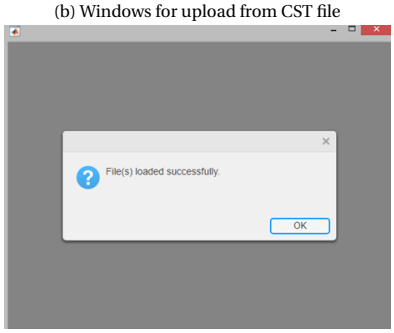

(c) Message that file(s) was/were successfully uploaded

Figure D.7: Uploading of the field of feed

D.2. Outputs

The third column includes two buttons at the top of the column that initiate the functions of the tool that compute the field radiated by the lens antenna. Firstly, the user needs to compute the equivalent current on the lens surface. The plots of the field of the feed in 2D and of the equivalent current on the lens surface in 2D are automatically plotted. Subsequently, the user can click on the button that computes the far field. This is a slow process, because it requires the calculation of the far field at each point of the far field sphere. Therefore, a message with a progress bar is displayed (Fig. D.8), so that the user is informed about the progress of the computations.

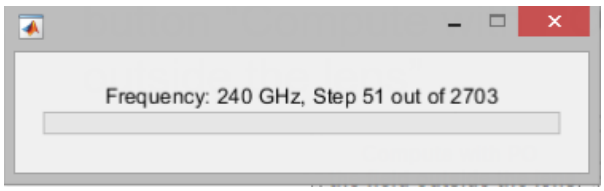

Figure D.8: Progress bar for far field computation

When the fields radiated by the lens antenna have been computed, the progress bar vanishes and the results regarding directivity, gain and efficiencies are displayed in the main window. The displayed values correspond to the selected frequency at the frequencies listbox.

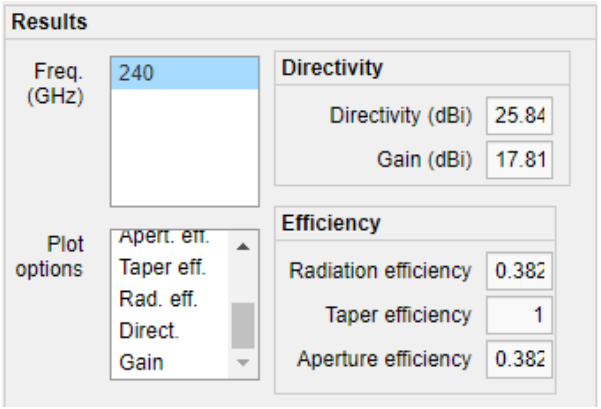

Figure D.9: Single-frequency results of directivity, gain and efficiencies

Apart from these results, the user can plot the electric field in 2D, in the cuts $\phi = 0°$, $\phi = 45°$, $\phi = 90°$, as well as the results for directivity, gain, aperture efficiency, taper efficiency and radiation efficiency over frequency. All possible plot options are shown in Fig. D.10.

Finally, the user can save the results in `.mat` files. First, it is asked that the user defines a folder to save the results, as shown in Fig. D.11. Then, when the user clicks the Save button, the tool creates, for each frequency studied before, a folder with a name that corresponds to the frequency and saves the `.mat` files in this new folder.

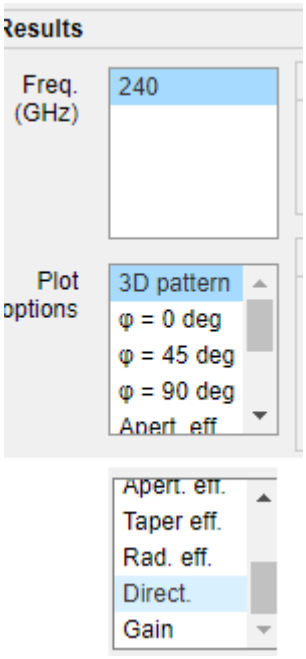

Figure D.10: Options for plotting the results

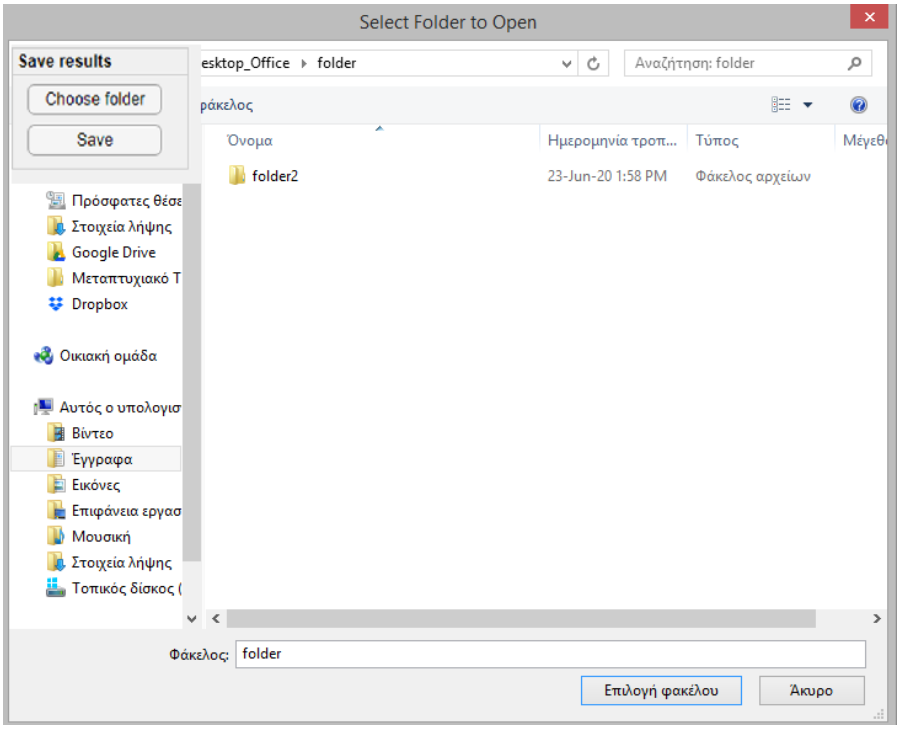

Figure D.11: Window for saving the results

Bibliography

[1] International Telecommunication Union, "Technology trends of active services in the frequency range 275-3 000 GHz," Rep. no ITU-R SM.2352-0, Jun. 2015. Accessed on: Dec. 1, 2019. [Online]. Available: https://www.itu.int/dms_pub/itu-r/opb/rep/R-REP-SM.2352-2015-PDF-E.pdf

[2] J. M. Chamberlain, "Where optics meets electronics: recent progress in decreasing the Terahertz gap," *Philos. Trans.: Math., Phys. and Eng. Sciences,* vol. 362, no. 1815, pp. 199-213, Feb. 2004, doi: 10.1098/rsta.2003.1312.

[3] D. Saeedkia, "Optoelectronic techniques for the generation and detection of terahertz waves," in *Handbook of Terahertz Technology for Imaging, Sensing and Communications*. Cambridge, U.K.: Woodhead Publishing, 2013, ch. 1, sec. 1.1, pp. 3-6. [Online]. Available: https://www.sciencedirect.com/book/9780857092359/handbook-of-terahertz-technology-for-imaging-sensing-and-communications.

[4] D. A. Neamen, "Nonequilibrium excess carriers in semiconductors," in *Semiconductors physics and devices: basic principles,* 4th ed., New York, NY, USA: McGraw-Hill, 2012, ch. 6, sec. 6.1, pp. 193-198.

[5] H. J. Gerritsen, "Terahertz dynamics in semiconductor heterostructures using ultrashort electrical pulses," Ph.D. dissertation, Dept. Physics, Eindhoven Univ. of Technology, Eindhoven, the Netherlands, 1998.

[6] D. H. Auston, K. P. Cheung, and P. R. Smith, "Picosecond photoconducting Hertzian dipoles," *Appl. Phys. Lett.,* vol. 45, no. 3, pp. 284–286, May 1984, doi: 10.1063/1.95174.

[7] J. T. Darrow, X. C. Zhang, D. H. Auston, and J. D. Morse, "Saturation properties of large-aperture photoconducting antennas," *IEEE J. Quantum Electron.,* vol. 28, no. 6, pp. 1607–1616, Jun. 1992, doi: 10.1109/3.135314.

[8] P. U. Jepsen, R. H. Jacobsen, and S. R. Keiding, "Generation and detection of terahertz pulses from biased semiconductor antennas," *J. Opt. Soc. Amer. B, Opt. Phys.,* vol. 13, no. 11, pp. 2424–2436, Nov. 1996, doi: 10.1364/JOSAB.13.002424.

[9] M. Tani, S. Matsuura, K. Sakai, and S. Nakashima, "Emission characteristics of photoconductive antennas based on low-temperature-grown GaAs and semi-insulating GaAs," *Appl. Opt.,* vol. 36, no. 30, pp. 7853–7859, Oct. 1997, doi: 10.1364/AO.36.007853

[10] E. R. Brown, "THz generation by photomixing in ultrafast photoconductors," *Int. J. High Speed Electron. Syst.,* vol. 13, no. 2, pp. 497–545, 2003, doi: 10.1142/9789812796820_0005.

[11] M. Hangyo, M. Tani, T. Nagashima, H. Kitahara, and H. Sumikura, "Spectroscopy and imaging by laser excited terahertz waves," *Plasma Fusion Res.,* vol. 2, Nov. 2007, Art. no. S1020, doi: 10.1585/pfr.2.S1020.

[12] A. Garufo, "Towards the engineering of pulsed photoconductive antennas," Ph.D. dissertation, Dept. Elect. Eng., Delft Univ. of Technology, Delft, the Netherlands, 2017. Accessed on: Sep. 29, 2019. [Online]. Available: https://repository.tudelft.nl/islandora/object/uuid:3850fd4d-9256-4925-88bb-9679da5f3aaf?collection=research

[13] G. C. Loata, M. D. Thomson, T. Löffler, and H. G. Roskos, "Radiation field screening in photoconductive antennae studied via pulsed terahertz emission spectroscopy," *Appl. Phys. Lett.,* vol. 91, p. 232506, Dec. 2007, doi: 10.1063/1.2823590

[14] N. Khiabani, Y. Huang, Y.-C. Shen, and S. J. Boyes, "Theoretical modeling of a photoconductive antenna in a terahertz pulsed system," *IEEE Trans. Antennas Propag.,* vol. 61, no. 4, pp. 1538–1546, Apr. 2013. Accessed on: Oct. 9, 2019. doi: 10.1109/TAP.2013.2239599, [Online]. Available: https://ieeexplore.ieee.org/document/6409989

[15] S. Preu *et al.*, “Principles of THz generation,” in *Semiconductor Terahertz Technology: Devices and Systems at Room Temperature Operation,* G. Carpintero, L. E. García-M~unoz, H. L. Hartnagel, S. Preu, and A. V. Räisänen, Eds. Hoboken, NJ, USA: Wiley, 2015, pp. 3–68, doi: 10.1002/9781118920411.ch2.

[16] R. Emadi, N. Barani, R. Safian, and A. Z. Nezhad, “Hybrid computational simulation and study of terahertz pulsed photoconductive antennas,” *J. Infr., Millim., Terahertz Waves,* vol. 37, no. 11, pp. 1069–1085, Aug. 2016, doi: 10.1007/s10762-016-0299-0.

[17] A. Garufo, G. Carluccio, N. Llombart, and A. Neto, "Norton equivalent circuit for pulsed photoconductive antennas–Part I: theoretical model," *IEEE Transactions on Antennas and Propagation,* vol. 66, no. 4, pp. 1635-1645, Apr. 2018. Accessed on: Sep. 6, 2019. doi: 10.1109/TAP.2018.2800524, [Online]. Available: https://ieeexplore.ieee.org/document/8276317

[18] A. Garufo, G. Carluccio, J. R. Freeman, D. R. Bacon, N. Llombart, E. H. Linfield, A. G. Davies, and A. Neto, "Norton equivalent circuit for pulsed photoconductive antennas–Part II: experimental validation," *IEEE Transactions on Antennas and Propagation,* vol. 66, no. 4, pp. 1646-1659, Apr. 2018. Accessed on: Dec. 13, 2019. doi: 10.1109/TAP.2018.2800704, [Online]. Available: https://ieeexplore.ieee.org/document/8278150

[19] G. Rana, A. Gupta, A. Bhattacharya, R. Jain, S. P. Duttagupta, and S. S. Prabhu, "Enhancing the THz emission through surface patterning in photo-conductive antenna, " in *2018 43rd Intern. Conf. on Infrared, Millimeter, and Terahertz Waves (IRMMW-THz)*, Nagoya, Japan. Accessed on: Dec. 23, 2019. doi: 10.1109/IRMMW-THz.2018.8510396, [Online]. Available: https://ieeexplore.ieee.org/document/8510396

[20] N. M. Burford, M. J. Evans, and M. El-Shenawee, "Fabrication and Characterization of Plasmonic ThinFilm Terahertz Photoconductive Antenna, " in *2018 IEEE Intern. Symp. on Antennas and Propagation & USNC/URSI National Radio Science Meeting*, Boston MA, USA. Accessed on: Dec. 23, 2019. doi: 10.1109/APUSNCURSINRSM.2018.8608534, [Online]. Available: https://ieeexplore.ieee.org/document/8608534

[21] D. V. Lavrukhin *et al.*, "Terahertz photoconductive emitter With dielectric embedded high-aspect-ratio plasmonic grating for operation with low-power optical pumps, " in *2019 Intern. Workshop on Antenna Technology (iWAT)*, Miami FL, USA. Accessed on: Dec. 23, 2019. doi: 10.1109/IWAT.2019.8730608, [Online]. Available: https://ieeexplore.ieee.org/document/8730608

[22] D. Turan, N. T. Yardimci, Z. Rong, D. Ren, H. Kim, D. Huffaker, and M. Jarrahi, "High-power terahertz generation from telecommunication-compatible, bias-free photoconductive nano-antennas, " in *2019 IEEE MTT-S Intern. Microwave Sympos. (IMS)*, Boston MA, USA. Accessed on: Dec. 23, 2019. doi: 10.1109/MWSYM.2019.8701036, [Online]. Available: https://ieeexplore.ieee.org/document/8701036

[23] A. Pelekanidis, "Design of a THz photoconductive connected array, " Honours Programme Master project, Dept. Elect. Eng., Delft Univ. of Technology, Delft, the Netherlands, 2020.

[24] A. Neto and J. J. Lee, ""Infinite bandwidth" long slot array antenna," *IEEE Antennas and Wireless Propagation Letters,* vol. 4, pp. 75-78, Jun. 2005. Accessed on: Dec. 17, 2019. doi: 10.1109/LAWP.2005.844141, [Online]. Available: https://ieeexplore.ieee.org/document/1424006

[25] A. Garufo *et al.*, "A connected array of coherent photoconductive pulsed sources to generate mW average power in the submillimeter wavelength band," *IEEE Transactions on Terahertz Science and Technology,* vol. 9, no. 3, pp. 221-236, May 2019. Accessed on: Sep. 6, 2019. doi: 10.1109/TTHZ.2019.2896791, [Online]. Available: https://ieeexplore.ieee.org/document/8663355

[26] D. Cavallo, "Connected array antennas : analysis and design," Ph.D dissertation, Technische Universiteit Eindhoven, Eindhoven, The Netherlands, 2011. doi: 10.6100/IR719461

[27] W. Yuan, L. H. Li, W. B. Lee, and C. Y. Chan, "Fabrication of microlens array and its application: A review" *Chinese Journal of Mechanical Engineering,* vol. 31, no. 16, Feb. 2018. Accessed on: Nov. 29, 2019. doi:10.1186/s10033-018-0204-y.

[28] V. N. Mahajan, "Optical aberrations," in *Optical imaging and aberrations: Part I. Ray geometrical optics,* SPIE Press Book, 1998, ch. 3, pp. 139-202.

[29] S. A. Campbell, *The Science and Engineering of Microelectronic Fabrication,* 2nd ed., New York, NY: Oxford University Press, 2001.

[30] S. K. Ghandi, *VLSI Fabrication Principles: Silicon and Gallium Arsenide,* 2nd ed., New York, NY: John Wiley and Sons, 1994.

[31] D. F. Filipovic, S. S. Gearhart, and G. M. Rebeiz, "Double-slot antennas on extended hemispherical and elliptical silicon dielectric lenses," *IEEE Trans. Microw. Theory Techn.,* vol. 41, no. 10, pp. 1738–1749, Oct. 1993. Accessed on: Nov. 17, 2019. doi: 10.1109/22.247919, [Online]. Available: https://ieeexplore.ieee.org/document/247919

[32] M. Born and E. Wolf, "Geometrical theory of optical imaging," in *Principles of Optics,* 7th ed., New York, NY, USA: Cambridge University Press, 1999, ch. 4, sec. 4.4, pp. 167-177.

[33] D. Cavallo, Class Lecture, Topic: "Lecture: Connected arrays equivalent circuits." EE4620, Dept. Elect. Eng., Delft Univ. of Technology, May, 2019.

[34] P. H. Bolivar *et al.*, "Measurement of the dielectric constant and loss tangent of high dielectric-constant materials at terahertz frequencies," *IEEE Transactions on Microwave Theory and Techniques,* vol. 51, no. 4, pp. 1062 - 1066, Apr. 2003. Accessed on: Nov. 18, 2019. doi: 10.1109/TMTT.2003.809693, [Online]. Available: https://ieeexplore.ieee.org/document/1193114

[35] D. M. Pozar, "Electromagnetic theory," in *Microwave Engineering,* 4th ed., Danvers, MA, USA: John Wiley & Sons, Inc., 2012, ch. 1, sec. 1.3, pp. 10-15.

[36] A. Ludwig, "The definition of cross polarization " *IEEE Transactions on Antennas and Propagation,* vol. 21, no. 1, pp. 116 - 119, Jan. 1973. Accessed on: May 2, 2020. doi:10.1109/TAP.1973.1140406, [Online]. Available: https://ieeexplore.ieee.org/document/1140406

[37] "TERA K15 All fiber-coupled terahertz spectrometer". Accessed on: Jan. 9, 2020. [Online]. Available: https://www.menlosystems.com/products/thz-time-domain-solutions/terak15-terahertz-spectrometer/

[38] "Photonic professional GT2". Accessed on: Jan. 3, 2020. [Online]. Available: https://www.nanoscribe.com/en/solutions/photonic-professional-gt2

[39] "Making precise structures at the smallest scale". Accessed on: Jan. 3, 2020. [Online]. Available: https://www.tudelft.nl/en/3me/research/check-out-our-science/making-precise-structures-at-the-smallest-scale/

[40] M. Albota *et al.*, "Design of organic molecules with large two-photon absorption cross sections," *Science*, vol. 281, no. 5383, pp. 1653-1656, Sep. 1998. Accessed on: Jan. 8, 2020. doi: 10.1126/science.281.5383.1653, [Online]. Available: https://science.sciencemag.org/content/281/5383/1653

[41] B. H. Cumpston *et al.*, "Two-photon polymerization initiators for three-dimensional optical data storage and microfabrication," *Nature*, vol. 398, pp. 51-54, Mar. 1999. Accessed on: Jan. 8, 2020. doi: 10.1038/17989, [Online]. Available: https://www.nature.com/articles/17989

[42] E. Biancalani, "Towards the characterisation of exo-Earths' atmospheres: 3D-printed microlenses for visible-NIR MKID-arrays," First master's research project, Faculty of Science, Univ. Leiden, Leiden, the Netherlands, 2019.

[43] "SOLIDWORKS". Accessed on: Jan. 9, 2020. [Online]. Available: https://www.solidworks.com/

[44] Y. Li and E. Wolf, "Focal shifts in diffracted converging spherical waves", *Optics Communications*, vol. 39, no. 4, pp. 211-215, Oct. 1981. doi: 10.1016/0030-4018(81)90108-5

[45] "Tanner L-Edit IC layout". Accessed on: Jan. 9, 2020. [Online]. Available: https://www.mentor.com/tannereda/l-edit

[46] N. Llombart, Class Lecture, Topic: "Lecture: Fourier Optics for Focal Plane Arrays." EE4580, Dept. Elect. Eng., Delft Univ. of Technology, Feb., 2019.

[47] *GRASP*. Accessed on: 26 Jul. 2020. [Online]. Available: https://www.ticra.com/

[48] P. Focardi, A. Neto, and W. R. McGrath, "Coplanar-waveguide-based terahertz hot-electron-bolometer mixers - Improved embedding circuit description," *IEEE Transactions on Microwave Theory and Techniques,* vol. 50, no. 10, pp. 2374-2383, Oct. 2002. Accessed on: Sep. 25, 2019. doi: 10.1109/TMTT.2002.803448, [Online]. Available: https://ieeexplore.ieee.org/document/1038878

[49] N. Llombart, B. Blázquez, A. Freni, and A. Neto, "Fourier optics for the analysis of distributed absorbers under THz focusing systems," *IEEE Transactions on Terahertz Science and Technology,* vol. 5, no. 4, pp. 573-583, Jul. 2015. Accessed on: Nov. 24, 2019. doi: 10.1109/TTHZ.2015.2439511, [Online]. Available: https://ieeexplore.ieee.org/document/7152993

[50] T. H. Büttgenbach, "An improved solution for integrated array optics in quasi-optical mm and submm receivers: the hybrid antenna," *IEEE Transaction on Microwave Theory and Techniques*, vol. 41, no. 10, pp. 1750-1761, Oct. 1993. Accessed on: Jun. 23, 2020. doi: 10.1109/22.247920, [Online]. Available: https://ieeexplore.ieee.org/document/247920